POLITECNICO
MILANO 1863

SCUOLA DI INGEGNERIA INDUSTRIALE
E DELL'INFORMAZIONE

Erosion and impurity migration modelling of helium plasmas in tokamaks and linear devices

Tesi di Laurea Magistrale in
Nuclear Engineering - Ingegneria Nucleare

Author: **Carlo Tuccari**

Student ID: 971655
Advisor: Prof. Matteo Passoni
Co-advisors: Dr. Gabriele Alberti
Academic Year: 2022-23

Abstract

Within the framework of magnetic nuclear fusion, the study of plasma-wall interaction (PWI) plays a key role in the way towards the successful realization of nuclear fusion reactors. Erosion processes on plasma facing components (PFCs) and the following contamination of the core by the eroded impurities can compromise the performances of the magnetic confinement devices. To study these phenomena, modelling tools, such as the ERO2.0 code, prove to be a precious resource to complement experimental activities. The goal of this thesis is to employ the code to study erosion and transport processes both in a linear device, GyM, and in a tokamak, ASDEX Upgrade (AUG). The thesis focuses on the role of helium as a plasma species, as its presence in future reactors as a D-T reaction product requires the study of its influence on PWI.
In GyM, simulations with a global approach were used to assess the influence of an additional PFC, the sample-holder, not included in previous studies, while also giving an estimate of the erosion rates of the lateral wall and the samples, assuming a variety of different wall materials and tuning the ion impact energy by applying a biasing voltage. Simulations were also conducted at a local micro-scale level, observing a tiny volume on the samples surface, allowing to evaluate the surface morphology of real samples employed in experimental campaigns, thus establishing a link between simulations and experiments.
In AUG, simulations were mostly aimed at reproducing PWI processes observed during an experimental campaign involving L-mode He plasma discharges. The main goal was to match the measured net eroded thickness on the outer divertor with the one computed by the simulations. Although preliminary results showed a large gap, a parametric analysis of electron and ion temperatures and the oxygen impurities concentration allowed to obtain a better agreement. Finally, the model was improved by considering a Z_{eff} distribution in the plasma, describing the local concentration of the two He charge states. Differences in impurity transport were observed with the new model leading to a lower tungsten impurity content in the volume.

Keywords: magnetic confinement fusion, ERO2.0, helium plasma, erosion

Abstract in lingua italiana

Nel contesto della fusione nucleare magnetica, lo studio dell'interazione plasma-parete (PWI) riveste un ruolo chiave nel percorso verso la realizzazione di successo dei reattori a fusione nucleare. I processi di erosione sui componenti a contatto con il plasma (PFC) e la conseguente contaminazione del nucleo da parte delle impurità erose possono compromettere le prestazioni dei dispositivi di confinamento magnetico. Per studiare questi fenomeni, strumenti di modellazione, come il codice ERO2.0, si dimostrano risorse preziose per integrare le attività sperimentali. L'obiettivo di questa tesi è impiegare il codice per studiare i processi di erosione e trasporto sia in una macchina lineare, GyM, sia in un tokamak, ASDEX Upgrade (AUG). La tesi si concentra sul ruolo dell'elio (He) come specie di plasma, poiché la sua presenza nei futuri reattori come prodotto della reazione D-T richiede lo studio della sua influenza sulla PWI.
In GyM, le simulazioni con un approccio globale sono state utilizzate per valutare l'influenza di un ulteriore PFC, il portacampioni, non incluso negli studi precedenti, fornendo anche una stima dei tassi di erosione della parete laterale e dei campioni, assumendo una varietà di materiali per la parete e regolando l'energia di impatto degli ioni mediante l'applicazione di una tensione. Le simulazioni sono state condotte anche localmente a livello microscopico, esaminando un piccolo volume sulla superficie dei campioni, consentendo di valutare la morfologia superficiale dei campioni impiegati realmente nelle campagne sperimentali, stabilendo così un collegamento tra simulazioni ed esperimenti.
In AUG, le simulazioni sono state principalmente mirate a riprodurre i processi di PWI osservati durante una campagna sperimentale che coinvolgeva scariche di plasma di He in L-mode. L'obiettivo principale era confrontare lo spessore netto eroso misurato sul divertore esterno con quello calcolato dalle simulazioni. Sebbene i risultati preliminari abbiano mostrato un ampio divario, un'analisi parametrica delle temperature degli elettroni e degli ioni e della concentrazione di impurità di ossigeno ha permesso di ottenere un migliore accordo. Infine, il modello è stato migliorato considerando una distribuzione di Z_{eff} nel plasma, che descrive la concentrazione locale dei due stati di carica dell'elio. Con il nuovo modello, sono state osservate differenze nel trasporto delle impurità, portando a un contenuto inferiore di impurità di tungsteno nel volume.

Parole chiave: fusione a confinamento magnetico, ERO2.0, plasma di elio, erosione

Contents

Abstract **i**

Abstract in lingua italiana **iii**

Contents **v**

1 Magnetic nuclear fusion **1**
1.1 Introduction to nuclear fusion energy 1
1.2 Nuclear fusion reactions and the plasma state of matter 2
1.3 Energetic balance: the Lawson criterion 6
1.4 Magnetic confinement 12
1.5 Introduction to plasma-surface interaction 19
1.5.1 Plasma facing components and the scrape-off layer 20
1.5.2 The plasma sheath 23
1.5.3 Consequences of ion impact upon plasma facing components walls . 27

2 Wall material erosion and impurity migration inside the plasma **31**
2.1 The physics of sputtering and impurity migration 31
2.2 The study of erosion and transport in tokamaks and linear plasma devices 38
2.2.1 Experimental studies 41
2.2.2 Modelling studies 44
2.3 Motivations and goals of the present thesis work 46

3 Tools and simulation strategies **49**
3.1 ERO2.0 code for the simulation of erosion and impurity migration 49
3.2 GyM linear device 53
3.3 ASDEX Upgrade 60

4 He plasma erosion simulations in GyM linear device **67**
4.1 Global erosion results on the lateral wall 67

4.1.1 Material and bias investigation in sample-holder configuration . . . 67
4.1.2 Realistic steel wall . . . 71
4.1.3 Evolution in multiple time-steps simulations . . . 74
4.2 Global erosion results on samples . . . 77
4.3 Global deposition results . . . 78
4.4 Local erosion results on W samples . . . 82

5 He plasma erosion simulations in ASDEX Upgrade 87
5.1 Parametric analysis for improvements in experimental agreement . . . 87
5.1.1 Electron temperature coefficient . . . 88
5.1.2 Ion temperature coefficient . . . 89
5.1.3 Oxygen impurity concentration . . . 90
5.1.4 Combination of parameters . . . 94
5.2 Evolution of the erosion profile at the following time steps . . . 96
5.3 The effect of considering realistic m_{eff} and Z_{eff} distributions . . . 98

6 Conclusions and future perspectives 103

Bibliography 107

List of Figures 119

List of Tables 125

1 | Magnetic nuclear fusion

This first introductory chapter aims at giving the framework of the research field this thesis is inserted in. Section 1.1 gives a general overview about the global energy issue, highlighting the role of nuclear fusion energy. Section 1.2 describes the physics of the nuclear fusion reactions involved and the plasma state of matter. Section 1.3 deals with the issue of the energetic balance of a self-sustaining fusion reactor. Section 1.4 focuses on the magnetic confinement approach. Finally, section 1.5 gives an introduction to the topic of boundary plasma and the phenomena arising from the interaction between a plasma and a solid surface.

1.1. Introduction to nuclear fusion energy

Energy supply has always been a central theme in the public debate worldwide. This has to do with the fact that energy is a crucial factor in our societies, since every human activity requires energy to be performed. It is not surprising then, that energy demand positively correlates with most indices associated with economic growth, technological and social development and human well-being [1].
In recent times, the discussion around this topic has been even more intense due to various factors. The ever-growing concern about climate change is pushing us to revise our global energy supply mix, which is still largely based on fossil fuels today, in order to comply with 2050 carbon neutrality plans [2]; furthermore, the issue must be tackled by a global perspective, whereas measures undertaken by individual countries are insufficient. Thus, this means that very delicate international relationship between countries are always involved, and the complexity is further aggravated in the last years by the outbreak of the conflict between Russia and Ukraine, the Israeli-Palestinian crisis and instabilities in many key countries involved in fossil fuel production in North Africa and Middle-East. In this complex picture, we must also take into account that energy demand is going to further increase in the next decades, since many countries are growing in demographics and gross domestic product (GDP) while working their way towards industrialization, and this, as already mentioned, is usually associated with greater energetic needings [1].

Thus, we find ourselves in a situation where more than 60% of electric energy supply and more than 80% of primary energy supply must transit to other, carbon-free, sources; among them, nuclear energy stands out as a candidate to cover a significant portion of it.

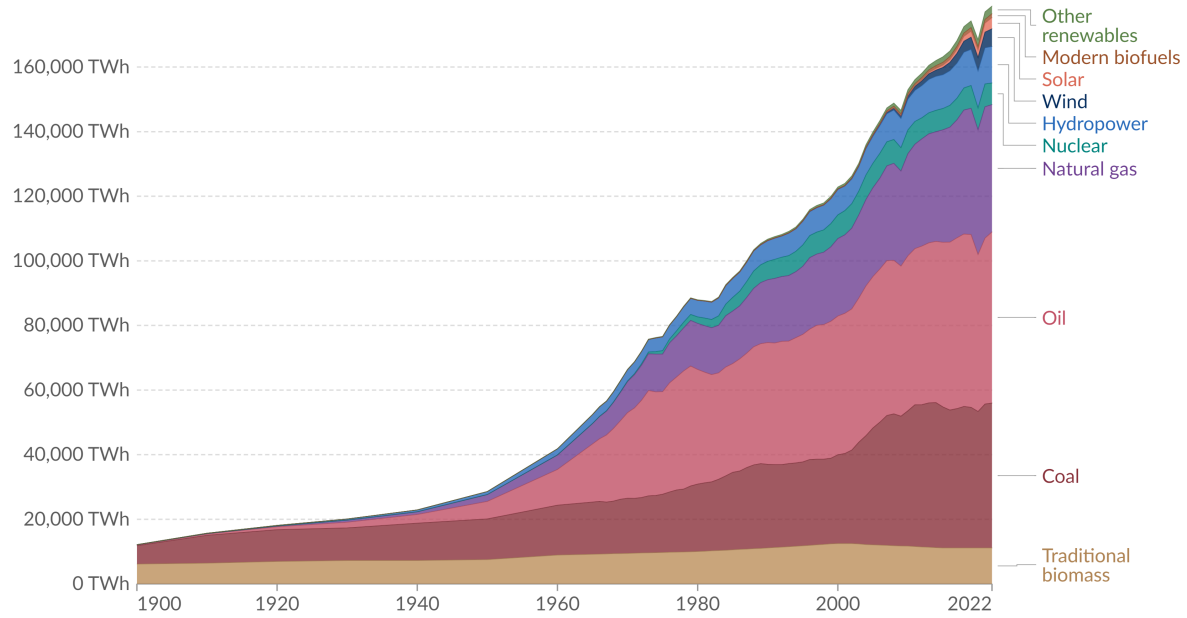

Figure 1.1: Global energy consumption by energy source [3]. The increasing trend can be easily noted.

Conventional nuclear fission power plants have been a part of the global energy mix for many decades already, they are a well established and mature technology which is set to play an important role in the decarbonization process of the next years, especially thanks to its reliability in covering base loads of energy demand. On the other hand, nuclear fusion has yet many challenges to face towards its realization as a reliable source of energy, but nonetheless it is considered a promising resource for the next centuries of energy production, thanks to the virtually unlimited availability of fuel and a much simpler management of radioactive waste, since produced radionuclides have in general a much shorter decay time compared to fission.

1.2. Nuclear fusion reactions and the plasma state of matter

In this section the physics of nuclear processes, which are responsible of the energy release exploitable by nuclear technologies, will be presented. In general, we call nuclear reactions

those processes in which a nucleus interacts with another, or with an external particle, producing new nuclides typically of different nature. Usually, a release or an absorption of energy is also observed during the process. The amount of energy, and whether it is released or absorbed, is fixed for a given reaction, as it is determined by the nature of the particles involved. In fact, from the energy balance across the initial and final state of the reaction, it can be shown that this energy, referred to as the Q-value, is given by the difference between kinetic energy in final and initial states, which can equivalently be expressed by the difference of energy associated to the rest masses of initial and final states [4].

$$Q = (m_i - m_f)c^2 \tag{1.1}$$

We can now observe that the mass of a nucleus slightly differs from the sum of the masses of its constituents by a quantity related to its binding energy.

$$m = Zm_p + Nm_n - \frac{\epsilon_b}{c^2} \tag{1.2}$$

Thus, assuming the number of nucleons is conserved, we can express the Q-value as the difference between binding energies of final and initial states.

$$Q = \epsilon_{b,f} - \epsilon_{b,i} \tag{1.3}$$

Therefore, to obtain a positive Q-value, hence a net release of energy, the produced nuclei must have greater binding energy than the initial ones, meaning they must be more stable.

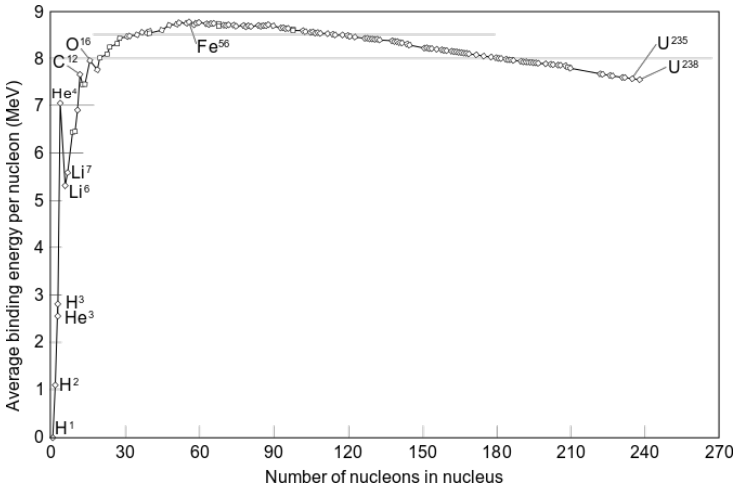

Figure 1.2: Nuclei binding energy per nucleon

In Figure 1.2 the average binding energy per nucleon for the most common nuclei is

represented. It shows a steep increase going from the lightest to heavier ones, then a peak around ^{56}Fe and finally a steady decrease towards transuranic elements. In fission reactions, the heaviest nuclides, on the far right of the plot, are struck by a neutron and split into two lighter elements which are located nearer to the binding energy peak, meaning that the new nuclides are overall more stable and the reaction will release energy in the form of kinetic energy of the produced nuclei. Similarly, in fusion reactions the lightest elements are combined to form a heavier and more stable one, again releasing energy.

Both kind of reactions involve interaction through the strong force, which is short-ranged and needs the interacting particles to get close to each other down to the femtometer scale. So here lies the main difference: while the electrically neutral neutron easily reaches the proximity of the heavy fissile nucleus, two electrically charged light nuclei must overcome Coulombian repulsion before being able to undergo nuclear fusion. Therefore, they must be supplied with energy first, before being able to produce it .

Here are some examples of fusion reactions exploitable for energy production [4]:

$$D + D \rightarrow He^3 + n + 3.27\ MeV \qquad br = 50\% \tag{1.4}$$

$$D + D \rightarrow T + p + 4.03\ MeV \qquad br = 50\% \tag{1.5}$$

$$D + He^3 \rightarrow \alpha + p + 18.3\ MeV \tag{1.6}$$

$$D + T \rightarrow \alpha + n + 17.6\ MeV \tag{1.7}$$

Notably, they all involve isotopes of H and He, because not only they are able to give large Q-value outputs being on the steeply increasing side of the binding energy curve, but they also have a weaker coulombian barrier as it scales with the square of Z. The former two involve only D as reactant, which is a stable and available in nature nucleus. However, their low cross section and the inferior energy output make them a less desirable choice. The latter two yield a very large Q-value having He4, an extraordinarily stable nucleus, in the output channel. Despite the slightly lower energy produced, the D-T reaction emerged as the favorite to be performed in the first fusion power plants mainly due to the characteristics of its cross section: in fact, Figure 1.3 shows that it reaches higher values and the peak is located at lower energies, making it more feasible.

The drawbacks of the D-T reaction are mostly due to the poor availability of T (also true for ^{3}He in D - ^{3}He reactions) and the production of a very energetic neutron, which retains 14.1 of the 17.6 MeV produced in the reactions, that escapes the core and causes activation issues along with radiation damage on surrounding materials. In relation to these topics, the role of Li can be mentioned. Two reactions between Li and the escaping

n can be exploited [5] :

$$Li^6 + n(slow) \rightarrow \alpha + T + 4.8\ MeV \tag{1.8}$$

$$Li^7 + n(fast) \rightarrow \alpha + T + n - 2.5\ MeV \tag{1.9}$$

Therefore, surrounding the core with a blanket of Li could be a solution to the T supply, while also stopping the energetic neutrons and potentially collecting the heat to be exploited in the conventional part of the plant.
Figure 1.3 also shows cross sections for other, more exotic, fusion reactions than the ones mentioned before. Among them it is worth mentioning the p - ^{11}B reaction:

$$p + B^{11} \rightarrow 3\alpha + 8.7\ MeV \tag{1.10}$$

Which is gaining renewed interest in recent years thanks to its aneutronic nature coupled with the absence of radioactive reactants or products [6, 7].

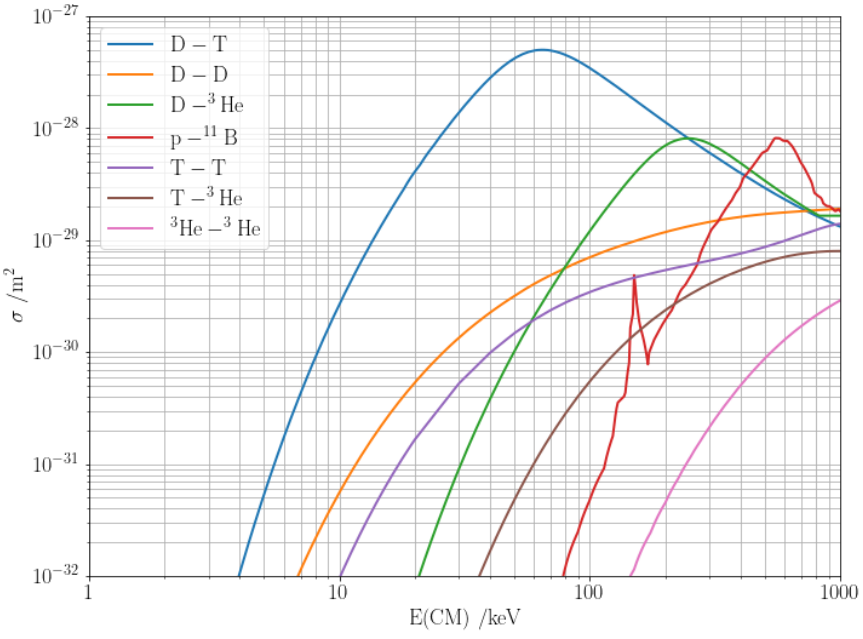

Figure 1.3: Cross section dependence on center of mass energy for each fusion reaction

It is possible to observe the extremely high temperatures necessary to reach acceptable values of the cross section; for reference, D-T reaction peaks in the tens of KeV range, which equals to hundreds of millions of K. For this reason the majority of nuclear fusion

research nowadays aims at achieving it in a thermonuclear plasma, the only state of matter capable of existing in such conditions, which will now be described briefly.
A plasma is a partially or fully ionized gas, whose collective behaviour is dominated by long-range electromagnetic interactions [8]. It is the most abundant state of matter in the universe and can range over extremely different density conditions, from those of the intergalactic medium ($1m^{-3}$) to the ones in the core of stars ($10^{32}m^{-3}$)[9]. Although it is overall neutral, it is interesting to highlight the self-shielding effect that takes place for an individual charge interacting with all the others in a plasma. A point charge potential is shaped like:

$$\phi \propto \frac{q}{r} \tag{1.11}$$

However, in a quasi-neutral plasma charges of the opposite sign will affect this potential, being attracted by it and screening its effect over a certain distance. The potential then assumes the form:

$$\phi \propto \frac{q}{r} e^{-\frac{r}{\lambda_d}} \tag{1.12}$$

Where the bare potential is multiplied by an exponentially decaying factor which represents the screening [5]. This shape is known as a Yukawa potential. The characteristic length appearing in the screening factor, λ_d, expresses the scale below which it is possible to feel charge imbalance effects in the plasma. It is called Debye length and is defined as follows:

$$\lambda_d = \sqrt{\frac{T}{4\pi e^2 n_0}} \tag{1.13}$$

Under the hypothesis that temperatures for the ionic and electronic populations are equal. The next section will be dedicated to describing and quantifying the conditions needed to grant the self-sustainability of nuclear fusion reactions inside the plasma, through an energetic analysis of the processes involved.

1.3. Energetic balance: the Lawson criterion

In a nuclear fusion reactor core we can describe an energetic balance like:

$$P_{ext} + P_\alpha = P_Q + P_R \tag{1.14}$$

On the left hand side we find the terms of power production, while on the right hand side we have power dissipation.

- P_{ext} represents any kind of external power supplied to the thermonuclear plasma.

- P_α is the power produced in fusion reactions and retained as alpha particles kinetic energy. It is only around 20% of the actual power released because alpha particles retain only 3.5 MeV of the total 17.6 Q-value of the D-T reaction. The remaining part is taken by the neutron which cannot be confined in the core. Can be expressed as [5]:

$$P_\alpha = \frac{1}{4} n^2 \langle \sigma v \rangle E_\alpha \tag{1.15}$$

  Where n is the density of D and T, assumed to be equal, $\langle \sigma v \rangle$ expresses the fusion reaction rate as the product of the cross section and relative velocity of the nuclei averaged over the Maxwellian distribution, E_α is the aforementioned 3.5 MeV energy of the alpha particles.

- P_R is the term representing Bremsstrahlung radiation losses of the system, expressable as [5]:

$$P_R = c_B Z_{eff}^2 n^2 T^{0.5} \tag{1.16}$$

  Where c_B is a constant, Z_{eff} represents the average ionization state of ions in the plasma, possibly considering also foreign heavy impurities, which cause an enhancement of radiation losses; this will be recalled in section 2.2.

- P_Q represents diffusive thermal losses. The strategy to express it is to define a time parameter τ_e, named confinement time, used to relate the energy content of the system to the energy loss rate with the following expression [5]:

$$P_Q = \frac{3nT}{\tau_e} \tag{1.17}$$

It is evident that the ultimate goal in a fusion reactor would be to maximize the power produced through fusion reactions, thus the P_α term, while minimizing the need of an external power supply. To measure performances towards this goal, a useful figure of merit can be defined as:

$$Q = \frac{P_\alpha}{P_{ext}} \tag{1.18}$$

Referred to as the gain factor. When $Q > 1$ the energy output surpasses the external energy supplied to the system, giving a positive net balance. The condition $Q = 1$ is called break-even. It must be noted though, that this parameter only accounts for the energy balance of the plasma; in the perspective of a realistic fusion power plant, the energy balance must be performed over the whole system involved, considering for instance the efficiency of transforming electric power input into power supply to the plasma, or transforming power produced by the plasma back to exploitable electric energy.

A modified version of the Q parameter, known as the engineering Q, is then useful:

$$Q_{eng} = \frac{P_{el,out} - P_{el,in}}{P_{el,in}} \tag{1.19}$$

It can also be related to the original Q [5]:

$$Q = \frac{E_\alpha + E_n}{E_\alpha + E_n + E_{Li}} \frac{Q_{eng} + 1 - \eta_e \eta_t}{\eta_e \eta_a \eta_t} \tag{1.20}$$

E_{Li} is the energy possibly extracted from n-Li reactions in the blanket surrounding the core. η_e is the efficiency of energy conversion towards energy forms exploitable for plasma heating, while η_a expresses the fraction of energy actually absorbed by the plasma. η_t is the efficiency of a conventional steam cycle to convert thermal power produced into electricity. Inserting typical values ($\eta_e = 0.7$, $\eta_a = 0.7$, $\eta_t = 0.4$ of these quantities in equation 1.20 it can be reduced to:

$$Q = 4(Q_{eng} + 0.72) \tag{1.21}$$

It can be observed that to achieve useful values of Q_{eng} a much higher Q is needed: $Q = 3$ equals Q_{eng} 0, while to obtain $Q_{eng} = 10$, $Q = 45$ is needed.
Going back to the energy balance in equation 1.14, we can examine the interesting case in which P_{ext} is set to zero, meaning that the system is in a steady state in which P_α is sufficient to compensate for the power losses and the fusion reaction is self-sustained, a regime known as ignition. Substituting the expressions in equations 1.15-17 into the balance, a condition for this to happen can be obtained:

$$n\tau_e \geq \frac{12T}{E_\alpha \langle \sigma v \rangle - 4c_B T^{0.5}} \tag{1.22}$$

Here Z_{eff} has been put =1 as would be for a pure D-T plasma without heavy impurities. This relation is known as the Lawson criterion [10] and gives a threshold value for the product of density and confinement time above which ignition is achieved. The term on the right-hand side is a function of the temperature with a minimum around $T = 25\ KeV$ for D-T reaction as shown in figure 1.4 , thus setting this value of temperature we get:

$$n\tau_e \geq 2 * 10^{14}\ s\ cm^{-3} \tag{1.23}$$

An equivalent formulation can be made using the triple product of n, T and τ_e on the left-hand side, instead of just n and τ_e. Figure 1.5 shows the relation between the gain

factors and the Lawson parameter; notably, the gain parameters tend to infinite when the ignition threshold is approached, as the external power goes to 0.

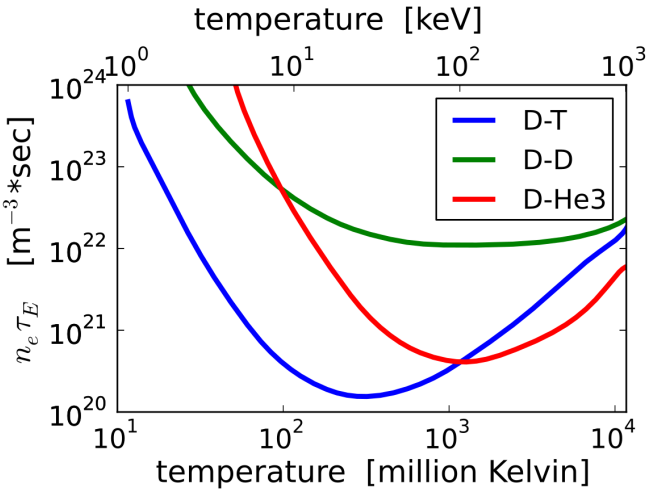

Figure 1.4: Lawson criterion threshold curve for different fusion reactions. Similarly to the cross section curves, D-T is the most favorable reaction having the lowest threshold and the minimum of the curve at a lower temperature. Taken from [11]

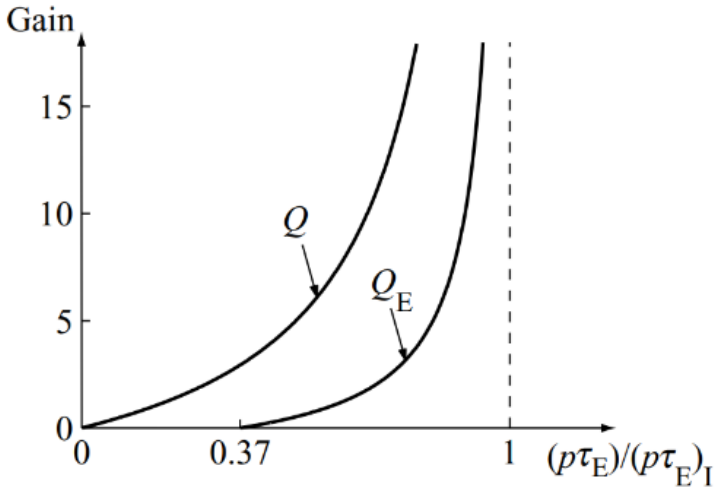

Figure 1.5: Q and Q_{eng} as functions of the triple product relative to the ignition threshold value [5]

The next step is to describe the strategies adopted to achieve high values of the $n\tau_e$ product. Over the years, two major branches have developed, focusing on confinement methods headed towards maximizing either the density or the confinement time.

- **Inertial confinement (ICF)** revolves around obtaining very high density values. The general principle, proposed by Nuckolls in 1972 [12], is shown in figure 1.6. It is based on a high power transfer to a millimeter-sized fuel pellet containing the D-T mixture, by means of many lasers. This causes a high velocity collapse of the target, strongly compressing it to the high densities needed to achieve ignition. The collapse can be performed by directly shining the lasers onto the pellet, a scheme called direct drive, or by using an auxiliary cavity named Hohlraum that converts light from the lasers into x-rays, which is instead the indirect drive; this second scheme has the benefit of a more uniform irradiation of the pellet, hence a more stable implosion process, at the expense of efficiency.
  It is called inertial confinement because in this case the task of confining the plasma is done simply by the inertia of the implosion process, which ends when the system naturally expands subsequently. This actually happens very rapidly, giving a characteristic scale of the confinement time τ_e of nanoseconds ($10^{-9}s$). Therefore, according to equation 1.23, densities of about $10^{23}cm^{-3}$ are required for ignition.

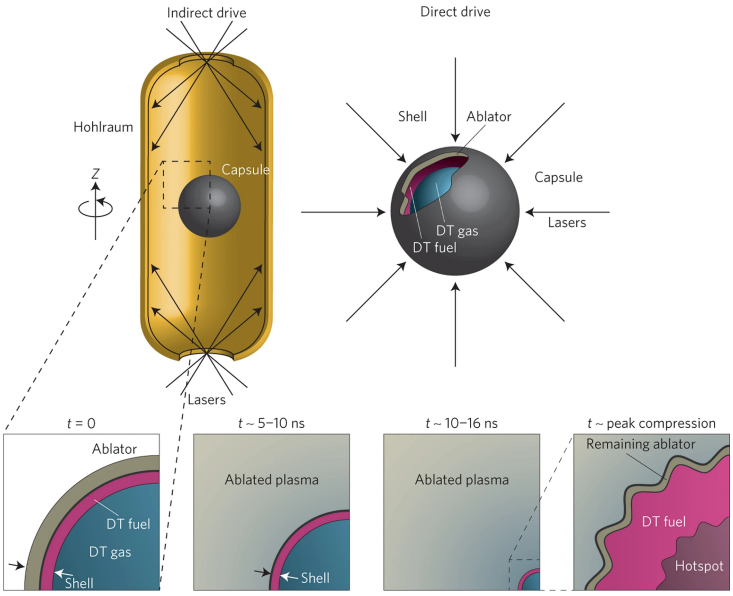

Figure 1.6: Scheme of implosion of the fuel pellet in inertial confinement fusion [13]

- **Magnetic confinement (MCF)** instead aims at keeping the plasma confined for longer times. Since the plasma is made of charged particles, magnetic fields can be employed to guide them through trajectories contained in a finite region of space, thus achieving confinement. The scale of τ_e is around seconds, instead of nanoseconds, allowing for a much more rarefied plasma compared to inertial confinement, of about $10^{14}cm^{-3}$ according to equation 1.23. This thesis work is

enclosed in the MCF framework, therefore it will be explained in more detail in the next section.

To end this section a brief overview of the state of the art of the progress towards ignition will be given. Figure 1.7 shows the experimentally inferred values of the Lawson parameter for many experiments carried out up to now, both in ICF and MCF. It can be observed an overall improvement over time, approaching the break-even threshold in more recent experiments, although slightly different considerations must be made for the two confinement methods.

The most relevant ICF facility is the National Ignition Facility (NIF) at the Lawrence Livermore national laboratory (US), and it produced many times values of the Lawson parameter close to the threshold line for ignition in the hot-spot, actually even surpassing it in one occasion. However, since the ignition is achieved only in a small region of the fuel, the overall balance still yielded a gain factor lower than 1, in particular $Q = 0.72$ [14], thus still below the break-even. More recent experiments seem to have produced even better results, actually going over break-even for the first time, as 3.15 MJ were released while only 2.05 MJ were supplied to the plasma, yielding $Q = 1.54$ [15].

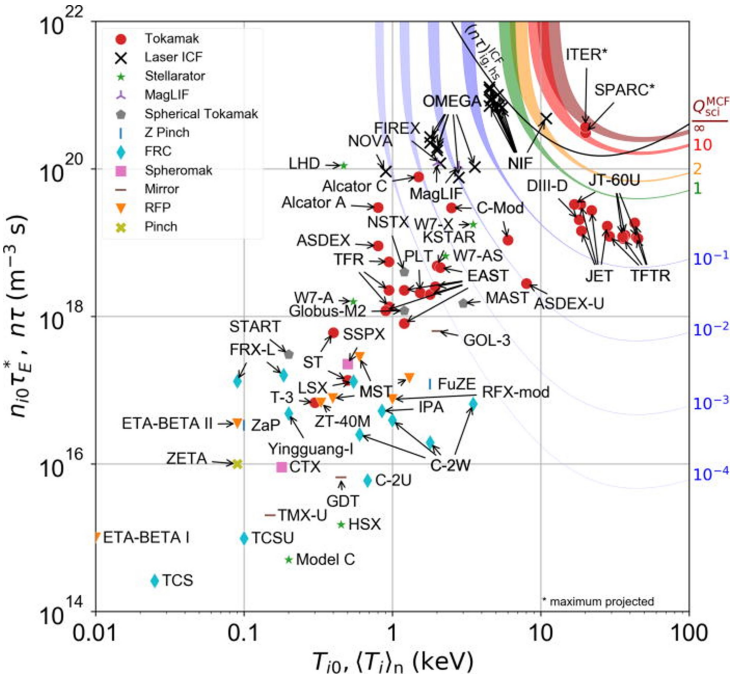

Figure 1.7: Estimated Lawson parameter for ICF and MCF experiments. The colored lines mark the thresholds for the specified value of the gain factor Q for MCF, while ICF data are compared against the hot-spot ignition threshold represented by the black line [16]

In MCF the best results up to date were given by the Tokamak Fusion Test Reactor (TFTR) and the Joint European Thorus (JET), which achieved respectively $Q = 0.27$ in 1995 [17] and $Q = 0.64$ in 1999 [18]. Both machines belong to the family of tokamaks, a kind of toroidally shaped magnetic confinement devices that are nowadays considered the most promising technology.
Figure 1.7 also shows forecasts for future MCF tokamak experiments, which are expected to exceed break-even. SPARC, located in Massachussets, is set to begin operation in 2025, with the main goal to achieve Q at least equal to 2 [19]. The International Thermonuclear Experimental Reactor (ITER) will be the largest tokamak in the world, to be built in southern France thanks to the international cooperation of many countries. The main goal of this device will be to reach at least $Q = 10$, producing 500 MW with 50 MW in input [20]. After ITER, another tokamak, the DEMOnstration power plant (DEMO), is set to be built on the same site to demonstrate electricity production and the feasibility of a real nuclear fusion power plant [21]

1.4. Magnetic confinement

In this section a more detailed description of how magnetic fields are exploited to confine the plasma will be given. We start by showing how single particles behave when moving in a magnetic field. A charged particles is subjected to the Lorentz force:

$$m\frac{d\boldsymbol{v}}{dt} = q(\boldsymbol{E} + \boldsymbol{v} \times \boldsymbol{B}) \tag{1.24}$$

First of all, we examine the simplest possible case, being the one in which no electric field $\boldsymbol{E}$ is present and the magnetic field $\boldsymbol{B}$ is constant, assumed directed along z. In this case the following system of equations is obtained:

$$\begin{cases} \dfrac{dv_x}{dt} = \dfrac{qv_yB_z}{m} = \omega_L v_y & \text{(1.25a)} \\ \dfrac{dv_y}{dt} = \dfrac{-qv_xB_z}{m} = -\omega_L v_x & \text{(1.25b)} \\ \dfrac{dv_y}{dt} = 0 & \text{(1.25c)} \\ v_x(0) = v_{x,0} = v_\perp \cos\Phi & \text{(1.25d)} \\ v_y(0) = v_{y,0} = v_\perp \sin\Phi & \text{(1.25e)} \\ v_z(0) = v_{z,0} = v_\parallel & \text{(1.25f)} \end{cases}$$

Where Φ is the angle of the velocity in the transverse plane with respect to the x axis, $\omega_L = \frac{qB}{m}$ is the so called Larmor frequency and its role will be clarified shortly. It is possible to observe that the magnetic field is not able to affect the motion parallel to it, which will therefore go on undisturbed, while it can act on the transverse components of the velocity.
The evolution of the particle's position can then be derived by integrating in time:

$$\begin{cases} x(t) = x_g + r_L \cos(\omega_L t - \Phi) & \text{(1.26a)} \\ y(t) = y_g + r_L \sin(\omega_L t - \Phi) & \text{(1.26b)} \\ z(t) = z_0 + v_\parallel t & \text{(1.26c)} \end{cases}$$

So, along z, parallel to the magnetic field, uniform motion is observed, while on the transverse plane particles are forced into a circular motion, called gyromotion, where the frequency of revolution is indeed the Larmor frequency. Other quantities shown in the expression must be further explained: $r_L = v_\perp/\omega_L$ is the Larmor radius, which is the radius of the circumference travelled by the particles in their gyromotion, $x_g = x_0 + r_L \cos\Phi$ and $y_g = y_0 - r_L \sin\Phi$ are the coordinates on the transverse plane of the guiding center, which is the center of said circumference. The Larmor frequency, hence the Larmor radius, depend on the magnetic field and on the mass of the particles. In fact, increasing the magnetic field leads to a higher frequency and a smaller radius. On the other hand, a higher mass means a lower frequency and a bigger radius, meaning that ions will rotate slower and at wider circumferences than electrons, considering also the added effect of ions having generally smaller velocities.

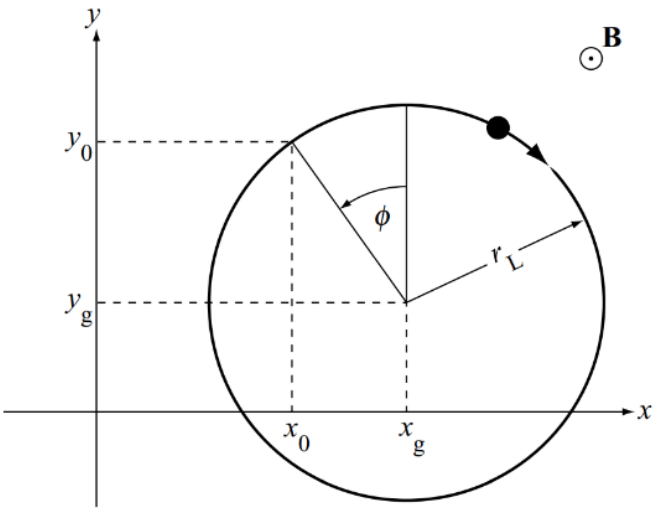

Figure 1.8: Gyromotion on the transverse plane [5]

A first idea of confinement can be noted: in the plane transversal to the magnetic field lines, particles are not able to go beyond a distance equal to the Larmor radius, and this effect can be tuned with the strength of the magnetic field, since a stronger field forces the particles to stay closer to the guiding center. However, this is not enough, because along the longitudinal direction the motion is still totally unrestricted, plus things become more complex if the hypothesis specified before are relaxed, introducing the electric field and space and time variations of $\boldsymbol{E}$ and $\boldsymbol{B}$.
To treat these cases an important assumption can still be made, under suitable conditions; in fact, if the field can be viewed as slowly varying, so that particles during their gyromotion do not experience a significant variation in the fields, the overall motion of the particles can be described as the composition of the gyromotion, just as described in the simple case, and the motion of the guiding center. The latter tends to be directed along the magnetic field lines, but when the electric field and variation of the fields in space and time are taken into account, it may experience deviations known as drifts, which will now be briefly presented.
In presence of an electric field both the longitudinal and the transverse motion are modified. Along B, the parallel component of the electric field will apply a force in that direction, which results in the motion being no more uniform. In the transverse plane, it can be demonstrated that a drift of the guiding center arises, in this form:

$$\boldsymbol{v}'_{\boldsymbol{E}\times\boldsymbol{B}} = \frac{\boldsymbol{E}\times\boldsymbol{B}}{B^2} \tag{1.27}$$

The resulting motion is thus perpendicular to both the electric and magnetic field and is called $\boldsymbol{E}\times\boldsymbol{B}$ drift. This kind of drift actually arises for any kind of force applied to the particles, to which the electric field is a particular case. For instance we could derive a similar expression for the gravitational field.
Another drift appears when the magnetic field has a gradient in the transverse direction; the form is similar to the $\boldsymbol{E}\times\boldsymbol{B}$ drift:

$$\boldsymbol{v}'_{\boldsymbol{\nabla B}} = \pm\frac{v_\perp^2}{2\omega_L}\frac{\boldsymbol{B}\times\nabla_\perp B}{B^2} \tag{1.28}$$

As before, the drift is directed perpendicularly both to the field and its transverse gradient.
A third drift term arises from the curvature of the magnetic field lines, sharing again a similar form with the previous ones:

$$\boldsymbol{v}'_{\boldsymbol{curv}} = \pm\frac{v_\parallel^2}{\omega_L}\frac{\boldsymbol{R_c}\times\boldsymbol{B}}{R_c^2 B} \tag{1.29}$$

Where R_c is the radius of curvature, thus giving a drift directed perpendicularly relatively to the curvature plane.
Another term is due to the time variation of both the electric and magnetic field:

$$\boldsymbol{v'_{pol}} = \frac{1}{\omega_L}\frac{d}{dt}(\frac{\boldsymbol{E}_\perp}{B}) \tag{1.30}$$

It is called polarization drift.
So, to correctly confine the plasma particles on the cross-field direction, all these effects must be handled, a complex, but still feasible, task. We must now consider how to achieve confinement in the longitudinal direction. We start by describing a phenomenon known as magnetic mirror effect, which in turn requires the description the motion in a parallel magnetic field gradient. Two quantities can be defined as constants of the motion; the first one is the kinetic energy, as the magnetic field does not transfer energy to the particles, expressed as:

$$E = \frac{1}{2}m(v_\parallel^2 + v_\perp^2) = const. \tag{1.31}$$

The second one is the magnetic dipole moment:

$$\mu = \frac{mv_\perp^2}{2B} = const. \tag{1.32}$$

Which is only approximately a constant, as it requires averaging over a period of gyromotion, in the hypothesis that the field is slowly varying. For this reason it is said to be an adiabatic invariant.
Now let's assume that a particle is moving along the field lines, starting from a low field position towards a higher field, experiencing thus a positive gradient. According to equation 1.32, when going into a higher B field, to keep μ constant, $v_\perp$ will also increase. In turn, as the kinetic energy is conserved, increasing $v_\perp$ implies that $v_\parallel$ must decrease according to equation 1.31, meaning that particles will experience an effective force opposite to the field gradient and will be decelerated longitudinally. The clear consequence is that if the magnetic field keeps increasing, it will reach a critical value that corresponds to $v_\parallel = 0$. At this point, the particle will not be able to further increase its $v_\perp$ and thus will not travel in regions with higher fields, but will instead be reflected back in the lower field region.

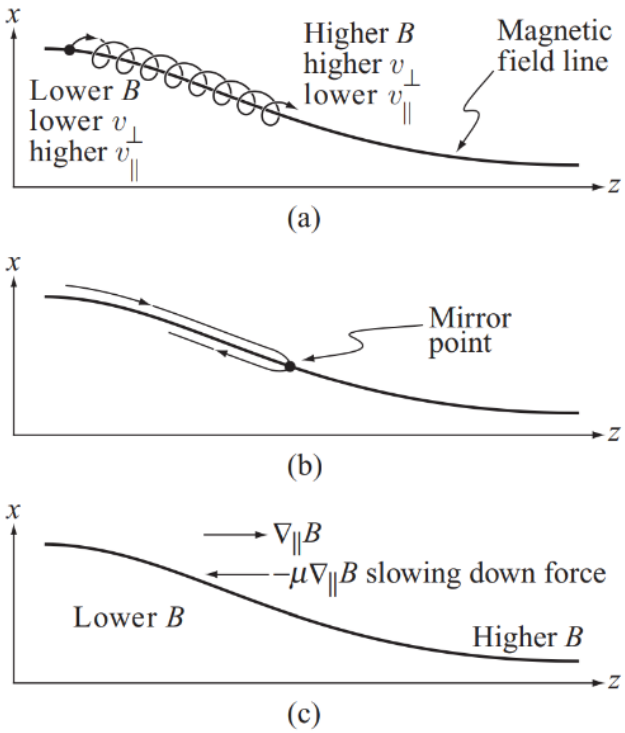

Figure 1.9: The mirror effect (a) Particle motion from low to high field region. (b) Reflection of the particle at the critical value of B for which parallel velocity goes to 0. (c) The longitudinal force experienced, opposite to the field gradient.

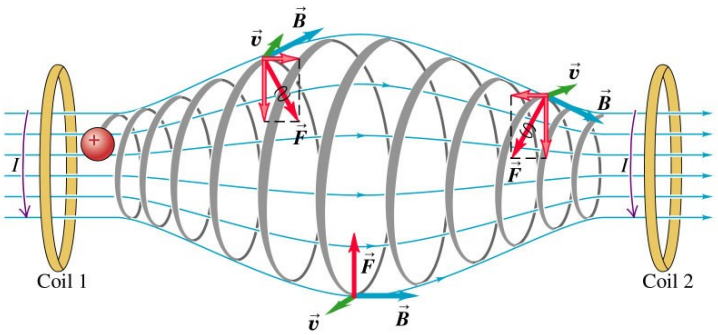

Figure 1.10: The configuration of a simple magnetic mirror machine [22]

This principle has been used to develop the first concept of magnetic confinement devices for thermonuclear plasmas, named magnetic mirrors, whose conceptual scheme is

presented in Figure 1.10. The field develops linearly in a cylindrical geometry, while it is increased at the extremes of the cylinder by additional coils, producing the mirror effect, thus containing the particles inside the cylinder. However, this concept proved to be ineffective at obtaining the desired confining capabilities, mostly due to losses at the ends, despite the use of the mirrors. In fact, the mirror confinement is not perfect, particularly due to the fact that the possibility to reflect the particles depends on the initial value of the transverse velocity; particles with too low initial $v_\perp$ need too high fields to be reflected, hence when they reach the cylinder ends they will be lost.
The following attempts at developing confinement schemes abandoned the reliance on the mirror effect to confine longitudinally, in favor of concepts where the magnetic field lines are closed in the confined region, so that a particle moving along the field will not escape confinement. The natural evolution is to consider the previous cylinder, bending it and closing it on itself so that it becomes a thorus, where the previously straight field lines are now closed on circular loops. This configuration is not able to confine the plasma without further adjustments, because some of the aforementioned drifts arise in this circular motion, particularly the curvature drift and the grad-B drift, since it can be demonstrated that the toroidal field has an inherent radial dependence. This issue can be fixed by adding another field component that forces particles to rotate on the poloidal plane, so that they experience different drifts in the inner and the outer radius that compensate each other. Therefore, the field lines will not be simple closed circular loops, instead they will wind around toroidally shaped surfaces infinitely, defining a set of nested magnetic surfaces as shown in figure 1.11.

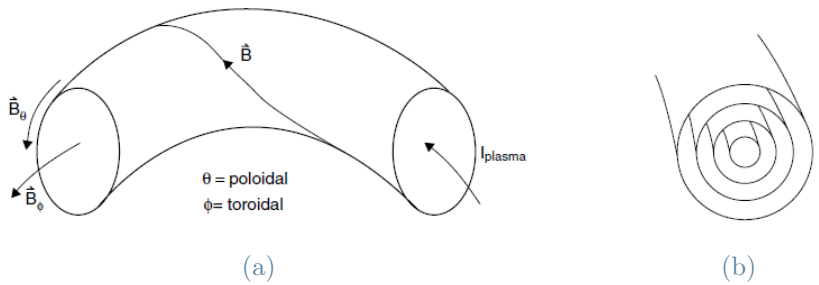

(a) (b)

Figure 1.11: Toroidal and poloidal magnetic field components (b) The nested magnetic surfaces defined by the winding of the magnetic field lines [23]

While the toroidal component of the field is always generated through currents in coils located in the poloidal plane, the poloidal component may be produced in different ways. This has led to a branching in two major families of toroidal devices.

The first one has already been mentioned in the previous section, the tokamak concept, that is the most considered and studied in today's research. In this kind of machine, the poloidal component of the field is produced by a toroidal current circulating in the plasma, which in turn is induced by means of a transformer [24]. For this reason the confinement in a tokamak cannot be performed in steady state. Many tokamak are operating or under construction a the moment around the world [25], some of them were already cited in the previous section, and each focuses on specific aspects of reasearch, ranging from basic plasma physics to power plant related topics.
The second family is that of stellarator machines. They are far less studied than tokamaks due to their initial poorer performances, and there is not a unique concept at the moment; for instance the japanese Large Helical Device (LHD) and the german Wendelstein 7-X (W7-X), the current two biggest stellarators in the world, have different approaches, the former belonging to the heliotron variant, while the latter is a heliac [26, 27]. Nonetheless, they do share the general principle, being able to produce a steady state confining field, at the expense of much more complexity in the geometry of the coils and other components, as shown in figure 1.12.
In conclusion, this chapter has presented the basic physics underlying magnetically confined thermonuclear plasmas. The next section will introduce the particular subtopic that will be the subject of the study presented in this thesis work: plasma-wall interaction (PWI). In fact, although it was stated that particles are confined by the magnetic field, it does not mean that the contact of the plasma with the physical boundaries of the machine can be completely avoided. Instead it will be shown how the correct understanding and management of such phenomenon is crucial to the successful operation of a magnetic confinement device.

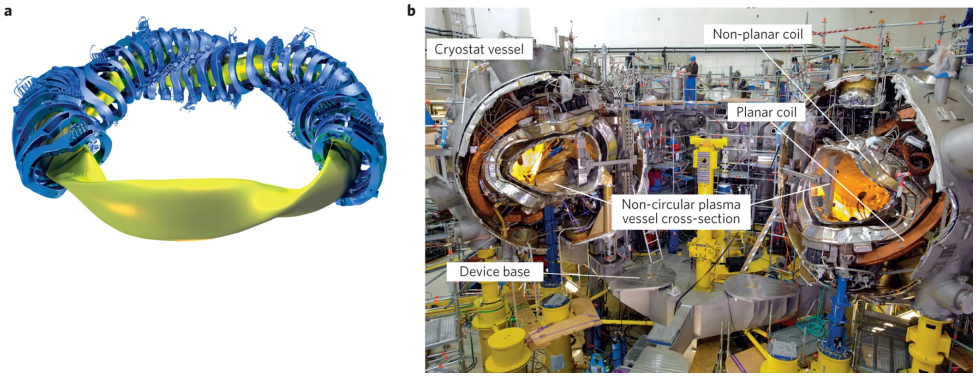

Figure 1.12: (a) Scheme of coils and magnetic surfaces in a stellarator. (b) Photograph of the W7-X during construction. From [28]

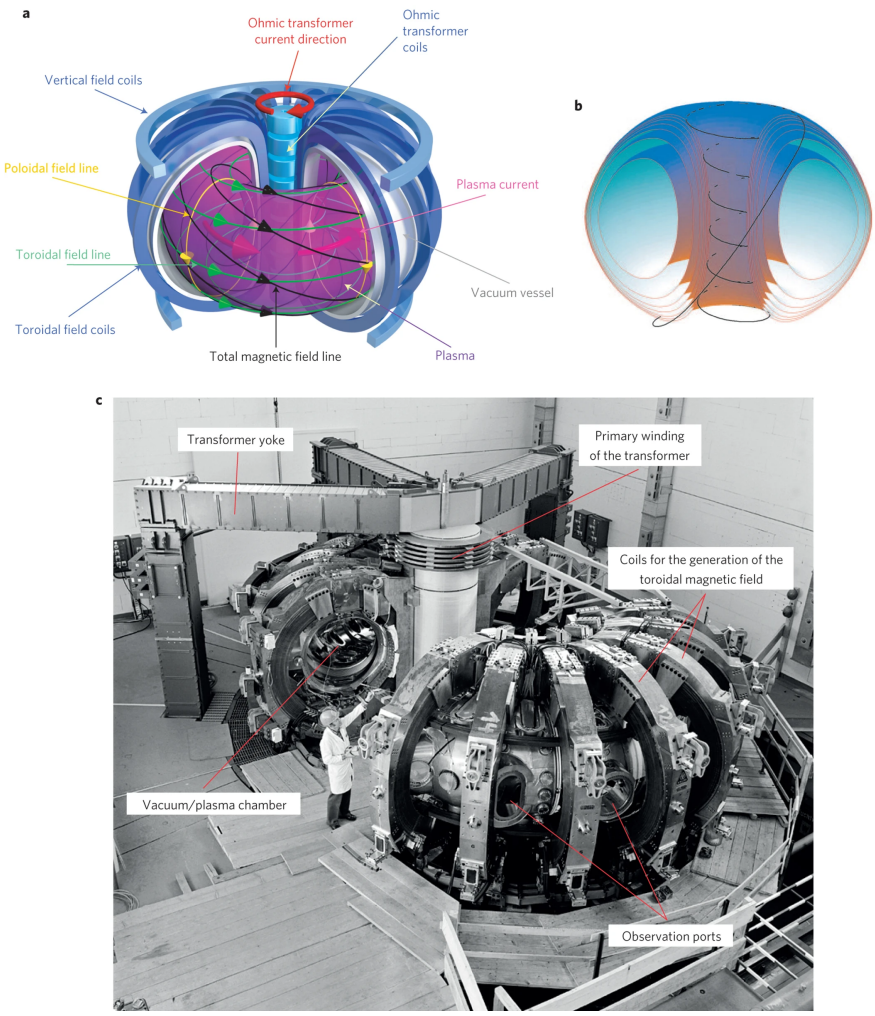

Figure 1.13: (a) Scheme of the coils system and the field lines in a tokamak. (b) Magnetic surfaces in a tokamak. (c) Photograph of the now dismantled Tokamak Experiment for Technology Orientated Research (TEXTOR) in Julich, Germany. From [28]

1.5. Introduction to plasma-surface interaction

This section aims to delve deeper into the topic of plasma-surface interaction (PSI) in magnetic confinement devices, which is the focus of this thesis work. The interface between the plasma state and the solid state of the machine walls gives rise to a variety of complex and coupled phenomena, that can seriously influence the performance thermonuclear plasma confinement, even compromising its ability to reach the desired plasma conditions if not properly handled. This introduction particularly focuses on the consequences of introducing a solid wall into a plasma, describing the arising of a boundary region named scrape-off layer and the plasma sheath. The most common plasma facing components (PFCs), such as limiters and divertors, will also be presented. Finally, an

overview of the phenomena caused by ion impact on the wall surface will be given.

1.5.1. Plasma facing components and the scrape-off layer

As shown in the previous section, a properly shaped magnetic field is able to force the particles to move along trajectories enclosed in a finite region of space, achieving confinement. However, turbulence and collisions can cause the particles to undergo an anomalous cross-field diffusion, moving through magnetic surfaces, escaping confinement and finally colliding against the machine walls. Moreover, a perfect confinement would not be ideal, as for practical reason it is important to be able to remove undesired particles in the plasma, e.g. impurities and He produced in fusion reactions. It is then of primary importance to be able to control where and how the contact between the plasma and the walls happens and to adopt strategies to mitigate the negative effects on the plasma.
To understand how to do it, let's start from a simple cylindrical geometry as shown in figure 1.14. In an unconfined plasma, ions and electron roam freely in the volume and will easily reach the lateral walls of the cylinder. However, as an axial magnetic field is added, a preferential motion along the field lines will be established, according to the confinement behaviour shown in the previous chapter. The motion across the field is not completely prevented, but it is very slow compared to the longitudinal motion, and the rate at which particles reach the lateral wall is greatly reduced [29].

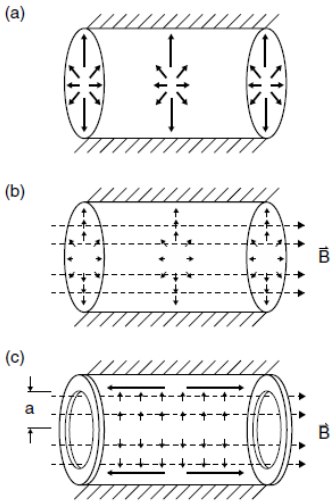

Figure 1.14: (a) Unconfined plasma in a cylinder. (b) Longitudinal magnetic field is applied. Radial motion is greatly reduced and only limited to diffusion processes. (c) Annular limiters are inserted, the stronger longitudinal motion brings the particles to collide with the limiters' sides. [23]

Now let's consider the addition of some annulus shaped components along the cylinder, with an outer radius equal to the cylinder's and a generic inner radius a as depicted in figure 1.14(c). A charged particle starting on the cylinder axis will move along the field lines, where the cylinder is assumed to be infinite in that direction, while slowly diffusing radially. At some point, the particle will diffuse enough to reach a radial position equal to the annulus inner radius a; evidently, as the stronger longitudinal motion carries on, in this condition the particles are quickly brought to impinge on the sides of the annulus component, thus limiting the ability of particles to explore radial regions much further than the inner radius. For this reason this component is called limiter. The addition of such component then allows to almost erase the particle flux impinging on the lateral wall, as the particles escaping confinement are redirected on these limiters, which therefore will be the place where the majority of the plasma-wall interactions occurs. This enables us to specifically design these components to properly perform this task in a more controlled way.

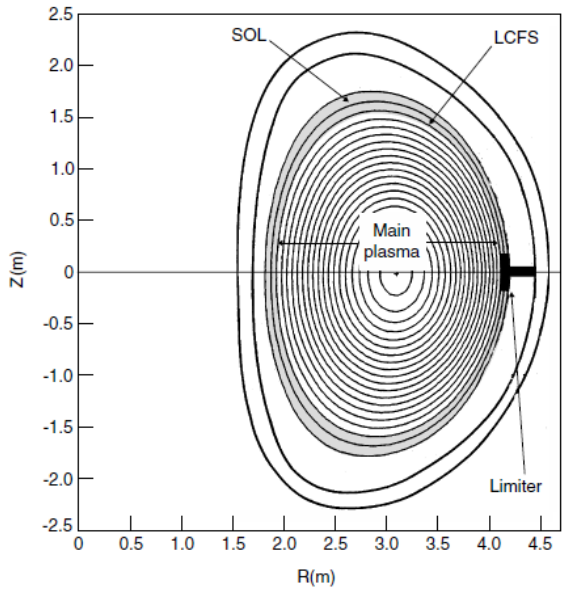

Figure 1.15: Toroidal limiter in a tokamak. [23]

Now let's turn our attention to the tokamak geometry. Adding an annular extrusion in the poloidal cross section would reproduce the behaviour described in the simple cylinder. But this is not the only limiter configuration possible in a tokamak; for instance, figure 1.15 shows a toroidal limiter, which has the same effect, since when particles cross the poloidal radius equal to the limiter innermost point they will impact on it because of their rotation in the poloidal plane. The magnetic surface corresponding to that value of

the poloidal radius is then called last closed magnetic flux surface (LCFS), as it is the surface defined by the outermost field lines that do not impact on the limiter. Magnetic surfaces lying beyond the LCFS belong to the so called scrape-off layer (SOL), the layer of boundary plasma where magnetic fields lines are destined to end on a solid surface.
The thickness of the scrape-off layer depends on the ratio between the cross-field velocity and the parallel velocity, as well as the length of the free path in the SOL, also known as connection length L [30, 31]:

$$\delta_{SOL} = \frac{v_\perp}{v_\parallel} L \tag{1.33}$$

To determine L, another important quantity must first be defined:

$$q = \frac{r B_\Phi}{R B_\theta} \tag{1.34}$$

where r is the smaller poloidal radius, R is the major toroidal radius, B_Φ and B_θ are respectively the toroidal and poloidal components of the field. q gives an estimate of the number of toroidal revolutions needed by the field lines to fulfill one poloidal rotation. It is named safety factor because it is linked to stability issues, which require it to be bigger than 2 at the LCFS [24]. This implies that B_Φ is signficantly greater than B_θ and that particles will perform multiple toroidal revolutions before completing one poloidal rotation, thus we can consider the trajectories to be approximately circular.
Having clarified this aspect, we can now give an extimate of the connection length. In the poloidal limiter configuration it will be:

$$L \approx \frac{\pi R}{n} \tag{1.35}$$

n being the number of limiters along the thorus. So that if there is one single limiter, L is equal to the toroidal circumference, while it will be shorter if there are more. Instead, in the toroidal limiter case:

$$L \approx \pi R q \tag{1.36}$$

Which is bigger, since a full poloidal rotation is needed to finally impact on the limiter, thus the toroidal circumference must be travelled q times. L can be as high as tens of meters, but thanks to the very small $v_\perp / v_\parallel$ ratio, the thickness of the SOL is still confined to the centimeters range [23].
Limiters are not the only kind of plasma facing component specifically designed to interact with the plasma. In fact, nowadays most tokamaks operate with a more complex kind of devices called divertors. Such name is due to the fact that these components divert the field lines, usually on the poloidal plane, to modifying the shape of the magnetic

field. This is done through an additional current loop parallel to the one circulating in the plasma as depicted in figure 1.16(a), creating the eight-shaped LCFS, which is also known as the separatrix. The imposition of a solid surface cutting the magnetic surfaces of the secondary loop acts similarly to the limiter, as the particles crossing the separatrix will find themselves on open field lines connected to the surface, on the so called divertor targets. The connection length can be considered approximately equal to the toroidal limiter case.

This configuration increases the magnetic volume, a notoriously expensive feature, but brings an important advantage in moving away the contact point between the SOL field lines and the target from the main plasma, whereas in the limiter configuration it was in close proximity. Figure 1.16(b) also gives a detail of the x-point of the separatrix, where a region called private plasma is observed. It is located inside the separatrix in the diverted region and mostly formed by plasma transported in the SOL and diffused back inside the separatrix near the divertor targets.

Having clarified this aspect of plasma confinement, the next section will proceed to show what happens where the SOL magnetic field lines impact on a solid target and a plasma-wall interface is formed.

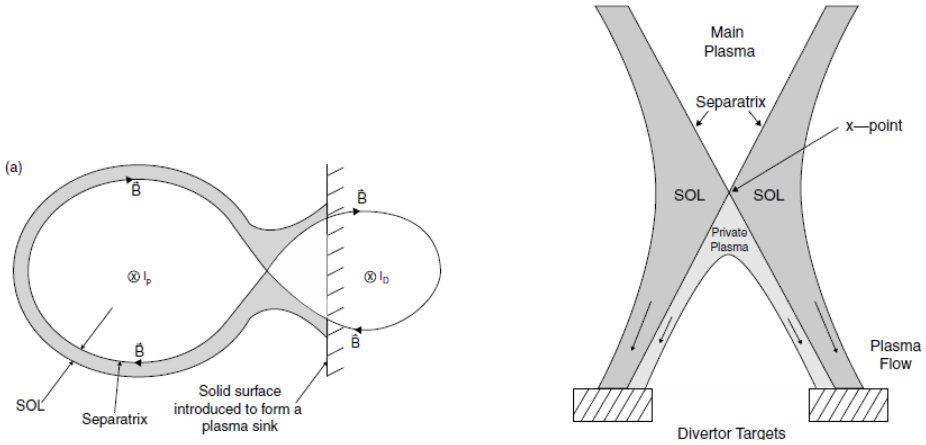

(a) (b)

Figure 1.16: (a) A diverted poloidal magnetic field, with an added solid surface and the formation of the relative SOL. (b) A zoomed view of the separatrix x-point. [23]

1.5.2. The plasma sheath

We now focus on what happens at the interface between the two states of matter. In the SOL, the field lines strike the divertor targets, causing the particles that move along the field to collide on the wall. Since the electrons are lighter than the ions and much more

mobile, they move faster and impact on the walls at a higher rate. Therefore, when the plasma is first generated, a higher number of electrons will arrive on the wall surface, depositing on it and causing an accumulation of negative charge. The consequence is that new electrons approaching the wall will feel a repulsive force, thus decreasing the electron flux to the surface; the opposite occurs for ions, that instead will feel an attractive force. This process then continues until the charge accumulation is enough to obtain equal ion and electron fluxes, establishing an equilibrium.
After this condition is reached, the self-shielding behaviour of the plasma introduced in section 1.2 arises. In fact, the net negative charge accumulated on the surface will generate a net positive charge region in the proximity of the wall, so that the integrated positive charge in that layer approximately equals the negative one deposited on the surface, almost shielding the rest of the plasma from charge imbalance effects. This net positive charge layer is called plasma sheath, was first described by Langmuir [32] and its extension is of the order of the Debye length [33] as expressed in equation 1.13. Thus, a potential drop is imposed across the sheath, and its magnitude can be demonstrated by imposing equal electron and ion fluxes to be:

$$V_{sh} = 0.5\frac{kT_e}{e}\log\left(2\pi\frac{m_e}{m_i}(1+\frac{T_i}{T_e})\right) \tag{1.37}$$

Which, for hydrogenic ions, is approximately:

$$V_{sh} \approx -3\frac{kT_e}{e} \tag{1.38}$$

The result is that ions arriving at the edge of the plasma sheath undergo an acceleration, with an energy gain equal to qV_{sh} where q is the charge of the ion, meaning that heavier ions, able to reach higher ionization states, experience a stronger acceleration in the sheath before impacting on the walls. Hence, the mean impact energy will be:

$$E = 2kT_i + \frac{3qkT_e}{e} \tag{1.39}$$

The first term is the mean energy of the ions before entering the sheath according to a Maxwellian distribution, while the second is indeed the energy gain across the sheath. This aspect will be very important in the next chapter when describing sputtering and other phenomena occurring when ions impact on the solid surface.
Figure 1.17 shows the profile of some quantities in 1D along the SOL field lines, where solid surfaces are placed at the two extremes. The potential is almost constant throughout the SOL, showing that it is mostly unaffected by the charge imbalance at the walls, and

suddenly drops in the sheath. Actually, a slight drop can be observed even in the pre-sheath region, because the shielding effect is not perfect, however must be noted that the pre-sheath drop is approximately:

$$V_{pre-sh} \approx -0.7\frac{kT_e}{e} \tag{1.40}$$

which is ≈4-5 times lower than the drop in the sheath. Moreover, the sheath drop occurs in the scale of a Debye length, which is around $10^{-5}m$ for typical tokamak conditions, while the pre-sheath takes place in the scale of the connection length, which can be several meters long. Hence, the electric field in the sheath exceeds the one in the pre-sheath region by a factor $\approx 10^5$. Nonetheless, the pre-sheath field still plays a role in driving the particles towards the sheath edge.
The velocity and density profiles are also reported in figure 1.17. Velocity matches the potential profile, as it is almost 0 where the potential is flat, while increasing dramatically across the sheath where the ions are strongly accelerated. The density of both ions and electrons also drops in the sheath, since the wall acts as a sink for charged particles, depleting the layer. The electron density though, decreases more, leaving the net positive charge in the layer, whereas in the pre-sheath region electron and ion densities are equal, according to the quasi-neutral nature of the plasma.

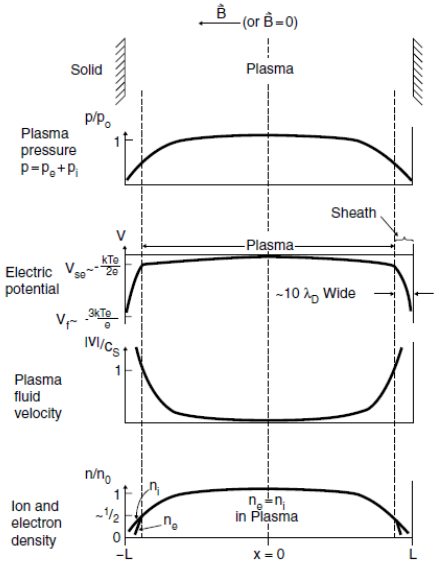

Figure 1.17: The pressure, potential, velocity and density profiles along a 1D profile following the field lines in the SOL between the two walls.

It is interesting to examine the case in which a bias is imposed to the wall, depicted in figure 1.18(a). It is possible to demonstrate that the self-shielding effect still holds, as the sheath absorbs also the additional potential difference and potential drop increases or lowers depending on the sign of the bias applied, still leaving the rest of the plasma unaffected.

Another meaningful particular case is the one in which the magnetic field lines do not fall perpendicularly to the wall surface, which is very common in tokamaks where very small grazing angles are preferred, so that the heat and particle flux on the surface is reduced, being distributed over a bigger surface. The observed effect is the formation of an additional layer, called magnetic pre-sheath or Chodura sheath, since it was first described by Chodura [34, 35], placed between the sheath and the pre-sheath. Its depth is of the order of the ion Larmor radius and its main effect is to tilt the direction of ions towards normal incidence, as shown in figure 1.18(b). The pre-sheath and the sheath retain the same characteristics previously explained.

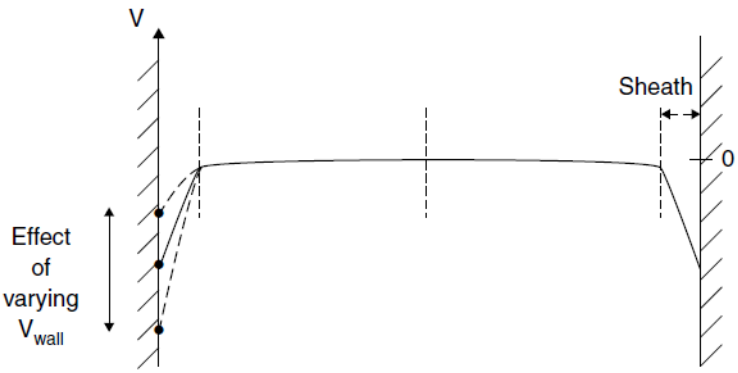

(a)

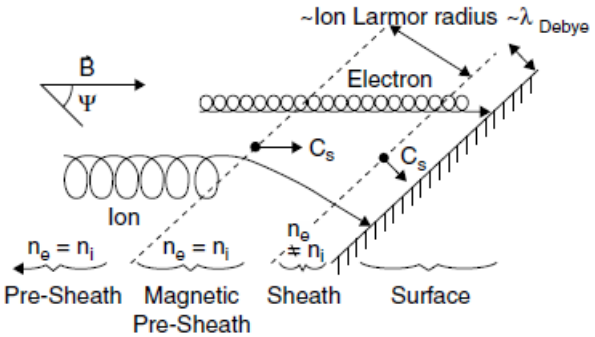

(b)

Figure 1.18: (a) The potential profile with a biased wall. The potential drop in the sheath varies accordingly to the bias, while the rest of the plasma and the right, unbiased wall remain unaffected. (b) The magnetic pre-sheath formed by oblique field-surface incidence

1.5.3. Consequences of ion impact upon plasma facing components walls

We must now describe what happens when an ion, accelerated through the plasma sheath, strikes the wall surface. The impinging ion can undergo two main destinies: it is either promptly back-scattered towards the plasma with a certain fraction of the impact energy, or penetrate the material and be implanted in it, then be thermally released after a more or less extended period of time. Regardless of which of the two events occurs, most of the ions striking the solid surface will be neutralized by picking up electrons from the wall. This happens because, as showed in the previous section, the walls are negatively charged and the time scale of the dynamics of ions is much longer than that of electrons, which are able to stick to the ions and fully neutralize them, even those carrying a high degree of ionization. This also explains the ion density profile in figure 1.17, which decreases towards the walls, as this is a recombination region and a higher density of neutrals is found. The neutral atoms thus re-enter the plasma, not being subjected either to the magnetic field or to the plasma sheath potential. However, it will be soon ionized again and it will start again moving towards the walls. Thus, a steady state regime called recycling is established, where a flux of charged particles goes from the plasma to the walls, while a neutral flux goes from the wall to the plasma. Figure 1.19 shows a scheme of the neutralization process at the walls.

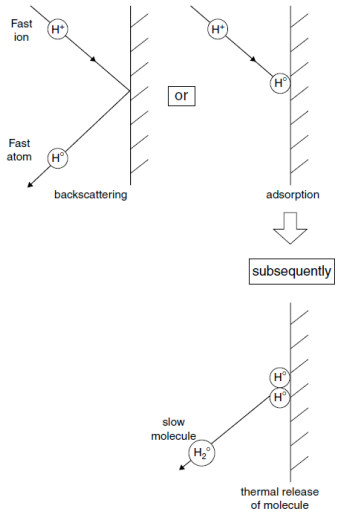

Figure 1.19: Neutralization process at the wall for a H ion, by prompt reflection (left), or by adsorption and thermal desorption in molecular form. [23]

The reflection is modelled through the use of reflection coefficients [36]:

$$R = \frac{\Gamma_R}{\Gamma_0} \tag{1.41}$$

Defined as the ratio between the flux of reflected particles to the total flux of impinging particles. An alternative definition can be given in terms of energy reflection coefficient, where the ratio between the total energy of reflected particles and the total energy of impinging particles is made. These coefficients are mostly found through experimental measures, or with the aid of codes [37, 38]. They depend on impact energy and angle, as well as on the projectile and target species, however a general behaviour can be observed: they tend to decrease at increasing energy, as more energetic projectiles penetrate deeper in the material and are less likely to be reflected out, while they increase with the m_{targ}/m_{proj} ratio, since a light projectile transfers energy to a heavy target less efficiently, hence it retains most of its energy and it is easily reflected.
Ions not immediately backscattered instead are implanted in the wall material, the concentration of the implanted species then increases up to a saturation concentration, after which new arriving ions are not retained in the material and are promptly released. This saturation level is controlled mainly by the impact energy and by the temperature [39–42], since increasing the temperature means that the implanted ions can be supplied with the energy needed to escape from traps and more easily diffuse out of the material.

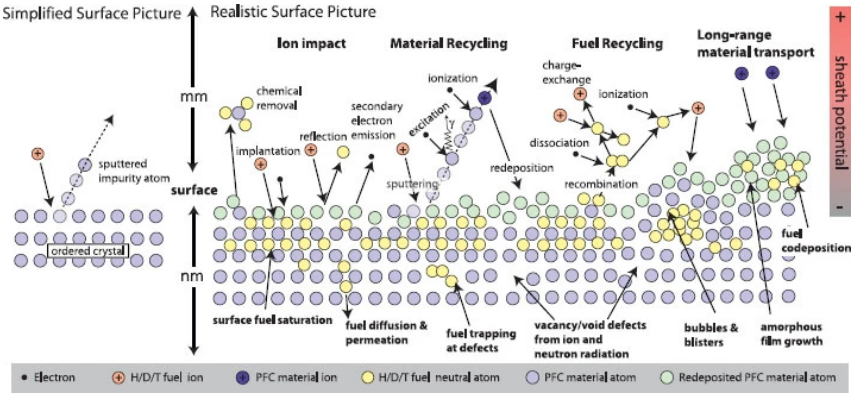

Figure 1.20: Scheme of main processes involved in plasma-surface interaction. [43]

Energetic ions striking the walls can transfer their energy to a wall atom, ejecting it from the solid and shooting it into the plasma. There, it will be ionized and driven again towards the wall, where it can redeposit and it turn cause further sputtering, in this case called self-sputtering, of the wall material. This process has a double negative effect: These sputtering processes can cause the erosion of the plasma facing component over time, possibly compromising its integrity and ability to perform, while on the other hand

the plasma gets contaminated with foreign species from the wall, altering its performance. Moreover, other processes can take place simultaneously, for instance the so called co-deposition mechanism, which contributes to fuel retention for longer time spans than previously described. Here, a previously sputtered atom from the material redeposits on the wall, but also buries a plasma ion in doing so, causing a fuel accumulation in the net deposition zones of the plasma facing components [44]. This can be problematic particularly in the case of T, which is radioactive and it is not ideal to have it accumulated in large quantities inside the material. The study of erosion and subsequent transport of impurities in the plasma constitutes the core of this thesis work, therefore they will be presented in more detail in the next chapter.
To conclude, while other processes occuring at the plasma interface could be presented, a schematic summary of the main phenomena is given in figure 1.20.

2 | Wall material erosion and impurity migration inside the plasma

This chapter is dedicated to the description of the erosion of plasma facing components and the migration of the eroded impurities inside the plasma. The physics of these processes will be presented in section 2.1, while section 2.2 will focus on reviewing erosion studies carried out in tokamaks and linear plasma devices, both from the experimental and modelling point of view. Finally, section 2.3 will present the motivations behind this thesis work, along with its main objectives.

2.1. The physics of sputtering and impurity migration

The erosion of the first wall material and the following transport of eroded impurities poses a serious threat to the successful realization of a nuclear fusion power plant. Too high erosion rate would be impossible to sustain, as the plasma facing components would face a strong deterioration and frequent substitutions would not be feasible in practical reactors. At the same time, the eroded material would enter the plasma, possibly even inside the separatrix, causing a dilution of the fuel and strongly enhancing radiation losses, hence undermining its performances. This section aims at giving an in-depth description of the physics of these processes.

As presented in section 1.5.3, an energetic ion impinging on the wall can give rise to many processes. One of them is the collision with an atom of the solid, which can in turn receive some of the energy carried by the projectile ion and even possibly be ejected from its lattice location. We must then quantify this energy transfer, and it can be demonstrated, by applying energy and momentum balances, that the fraction of energy transferred in an

elastic collision is:

$$\gamma = \frac{4M_1M_2}{(M_1+M_2)^2}\frac{1-\cos\theta}{2} \tag{2.1}$$

For a given pair of projectile and target, it has a maximum when the scattering angle θ is equal to π, which implies a perfectly head-on collision. It then becomes:

$$\gamma_{max} = \frac{4M_1M_2}{(M_1+M_2)^2} \tag{2.2}$$

It can be noted that the amount of transferred energy depends only on the masses of the two nuclei involved. In particular, the energy transfer is most efficient when the nuclei have similar mass, reaching a maximum in the limiting case where they are perfectly equal, which yields $\gamma = 1$, hence the total kinetic energy is transferred from the projectile to the target.

In order to observe sputtering, the target atom must be broken free from its bonds with other atoms of the solid. This implies that the transferred energy must be greater than the binding energy of said atom. Sputtering is therefore a threshold process, it only happens if projectile atoms satisfy a minimum energy requirement. An estimate of the value of this energy threshold can be given by assuming the simple two-collisions model depicted in figure 2.1 [23]. Here, the impinging ion penetrates in deeper layers and is backscattered by them, retaining a fraction of its energy equal to $(1-\gamma)$; then, it strikes an atom of the more superficial layers from below, transferring an energy fraction γ to it. Thus, the sputtered atom leaves the solid with the following energy:

$$E_{sput} = E_0\gamma(1-\gamma) - E_b \tag{2.3}$$

where E_0 is the initial energy of the projectile and E_b is the binding energy. Of course, E_{sput} must be greater than 0 to observe sputtering, which enables us to derive the threshold condition on E_0 by imposing $E_{sput} = 0$:

$$E_{th} = \frac{E_b}{\gamma(1-\gamma)} \tag{2.4}$$

The binding energy depends on the properties of the considered material and are in general known values. It can be considered to be the heat of sublimation and the values for relevant materials can be found in [45]. It must be noted that this simple model fails in case of identical projectile and target, which would give $E_{th} = \infty$, preventing the self-sputtering phenomenon, which is instead observed to occur.

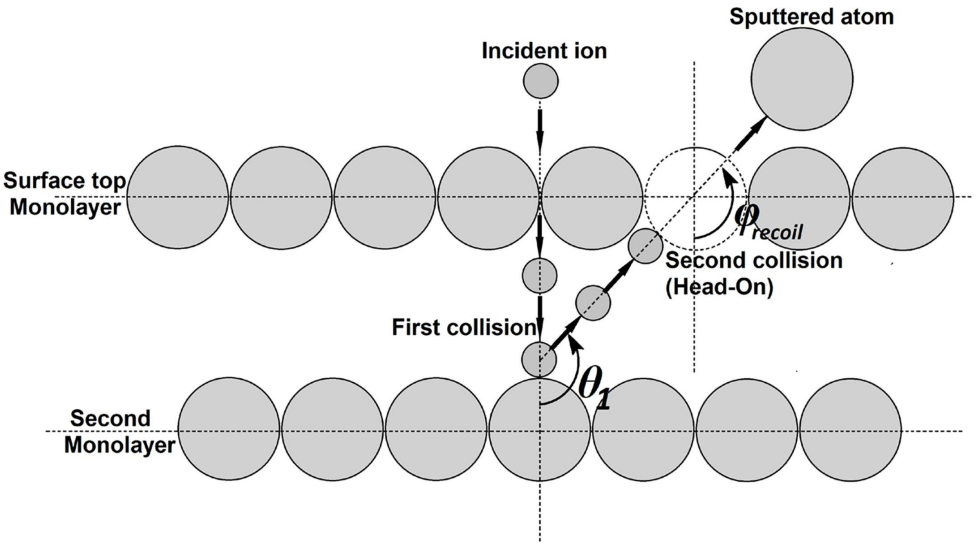

Figure 2.1: Two-collision model for physical sputtering energy threshold. From [46]

The sputtering process is characterized mainly by the definition of a suitable coefficient, known as sputtering yield. Similarly to the reflection coefficients described in section 1.5.3, it can be defined as:

$$Y = \frac{\Gamma_s}{\Gamma_0} \tag{2.5}$$

Where Γ_s is the flux of sputtered atoms and Γ_0 is the flux of incident ions. Therefore, it gives an estimate of the number of sputtered atoms per projectile. Obtaining reliable values of the sputtering yields is crucial to correctly predict the erosion rate of the wall for a given flux of incident particles, however it is not an easy task, since it depends on energy and angle of incidence, as well as the atomic species of the projectile and the material.
The first way to obtain them, is by means of experimental measures. They must be carried out using very mono-energetic and collimated ion beams to reduce the error, however they do not allow to draw general conclusions, since each measure refers to the specific energy, angle and projectile-target pair used. Therefore, experimental measures constitute a useful database to be compared with other tools that allow a more general approach, helping to refine them to higher degrees of accuracy.
A step towards a more universal description is made by developing a fitting formula, a theoretical expression of the sputtering yield which aims to well represent the available experimental data, while also trying to predict other cases through a suitable representation of the observed dependencies on relevant quantities. In general, the expression of the sputtering yield is given as a product of an energy factor, valid for normal incidence, and an angular factor:

$$Y(E, \theta) = Y(E, 0)A(E, \theta) \tag{2.6}$$

The normal incidence energy term is generally well described by the Bohdansky formula [47–49]:

$$Y(E,0) = qS_n(\epsilon)g\left(\frac{E_{th}}{E}\right) \tag{2.7}$$

q is called yield factor and depends on the surface binding energy and the projectile-target mass ratio. S_n is the so called nuclear stopping cross-section and depends on the reduced energy ϵ, whose definition may vary in different formulations. The g function expresses the threshold behavior of the phenomenon. An improved version was proposed by Eckstein and Preuss [50]:

$$Y(E,0) = qS_n^{Kr-C}(\epsilon)\frac{\left(\frac{E}{E_{th}}-1\right)^{\mu}}{\lambda+\left(\frac{E}{E_{th}}-1\right)^{\mu}} \tag{2.8}$$

Here the nuclear stopping is described using the Kripton-Carbon interaction potential, which is:

$$S_n^{Kr-C}(\epsilon) = \frac{0.5\ln\left(1+1.2288\epsilon\right)}{\epsilon+0.1728\sqrt{\epsilon}+0.008\epsilon^{0.1504}} \tag{2.9}$$

Where the reduced energy ϵ is defined as:

$$\epsilon = E\frac{M_2}{M_1+M_2}\frac{a_L}{Z_1Z_2e^2} = E\epsilon_L \tag{2.10}$$

M_1,Z_1,M_2,Z_2 are the masses and atomic numbers of the projectile and the target respectively, while a_L is the Lindhard screening length, expressed as:

$$a_L = \left(\frac{9\pi^2}{128}\right)^{\frac{1}{3}} a_B\left(Z_1^{\frac{2}{3}}+Z_2^{\frac{2}{3}}\right)^{-\frac{1}{2}} \tag{2.11}$$

In which a_B is the Bohr radius. The μ and λ parameters were not present in previous formulations of the Bohdansky formula, their addition proved to give a better fit of the behaviour near the energy threshold.
The angular part was described by Yamamura [51], but again improved by Eckstein and Preuss [50], in the form:

$$A(E,\theta) = \left[\cos\left[\left(\frac{\pi\theta}{2\theta_0}\right)^c\right]\right]^{-f}\exp\left[b\left(1-1/\cos\left[\left(\frac{\pi\theta}{2\theta_0}\right)^c\right]\right)\right] \tag{2.12}$$

Where b, c, f are fitting parameters, while the term θ_0 is:

$$\theta_0 = \pi - \arccos\sqrt{\frac{1}{1+E/E_{sp}}} \tag{2.13}$$

Where E_{sp} is the surface binding energy which may be experienced by the projectile.
Another important resource to improve the description of sputtering yields, is the calculation through dedicated codes, such as TRIM [47–49], or its recent upgraded version SDTrimSP [52, 53].

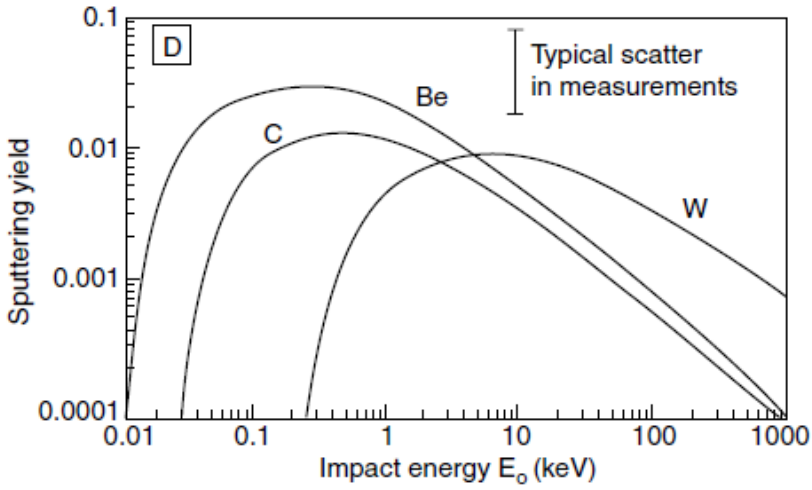

Figure 2.2: Energy dependence of normal incidence sputtering yields for a D projectile on common wall materials

Figure 2.2 shows the sputtering yields for a D ion striking materials commonly used in plasma facing components, such as Be, C and W. Some general characteristics can be observed, which remain true even for other projectile-target pair. For instance, the threshold behavior can be noted, as the curves vanish below E_{th}, and a steep increase of the yields is observed right above the threshold energy. This leads to great uncertainties when evaluating the yields in the threshold region, because a slight fluctuation in energy can lead to a very different sputtering yield value. The curve then saturates to a maximum value and subsequently decreases at very high energy, as an energetic projectile will penetrate deep in the material, depositing less energy in the surface layers.
Heavier elements, such as W, show a higher threshold, as well as generally a lower value of the sputtering yield. In fact, as formerly described, a light D ion will transfer very little energy to a heavy atoms, making sputtering more difficult. In principle, if the D/T energy could be controlled in order to stay below the threshold, the sputtering would not occurr at all; however, in reality this is very difficult, since the plasma ions are never monoenergetic and a high energy tail in their distribution able to sputter always exist. Moreover, once the wall material has been eroded, it may be ionized in the plasma, driven back through the sheath and accelerated towards the wall, where it redeposits and causes

a new sputtering event, called self-sputtering. The erosion-deposition cycle is depicted in figure 2.3.
While sputtering yields for D/T on common wall materials are about a few percent, self-sputtering yields are much higher, as the energy transfer between two equal nuclei is extremely efficient, and they can even be higher than 1, meaning that they can give rise to a self-sputtering cascade event. Hence, even a very small concentration of impurities can have a relevant impact on the erosion process. It must be specified that the sputtering yields do not depend on the charge state of the ions explicitly, fully ionized ions or neutral atoms of the same species cause the same sputtering if striking with the same incidence energy and angle; however, the charge state affects the energy gain in the sheath potential drop, granting higher incidence energies to higher charge state ions and resulting in a different sputtering yield, which is usually higher if the ion is on the increasing side of the sputtering yield curve.

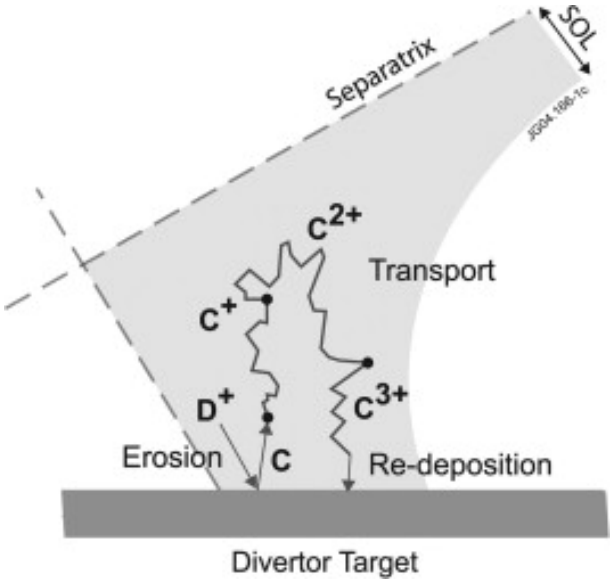

Figure 2.3: The local erosion-deposition process for impurities eroded by a C divertor target. From [54]

For some plasma-material pairs, another kind of sputtering process may play an important role: chemical sputtering. In this process the bonds of the target atom are not broken just by kinetic energy transfer, but a chemical interaction occurs to favor sputtering even at energies below the energy threshold. For instance, this phenomenon occurs in the case of hydrogenic plasma interacting with a C wall, with yields in the order of a few percent. If O is present, it becomes even more important, since the O on C chemical sputtering yield reaches values around 1. Hence, good vacuum conditions are desirable to have the

lowest amount possible of residual O.

The problems related to the sputtering processes do not end in the erosion of the first wall material. In fact, the subsequent migration of the eroded impurities inside the plasma also plays a crucial role, affecting the plasma behaviour, which would otherwise be unaltered if all the eroded particles promptly re-deposited near their erosion location. Instead, long range transport mechanisms take place in the scrape-off layer of a tokamak [55], leading eroded particles to re-deposit very far from their starting spot, or even entering the separatrix, causing contamination of the main plasma. The consequence can be the formation of net erosion or net deposition regions around the main chamber, causing for instance the aforementioned tritium retention issue. If the impurities are transported to the main plasma, the negative effect is a dilution of the fuel and the enhancement of radiation cooling, possibly lowering the temperature too much for fusion to occurr and compromising the core performance. For this reason divertor configurations are preferred over limiter ones, as they allow to move the impurity sources away from the core boundary, increasing the screening capability. In fact, while in limiter machines the core contamination is dominated by erosion on the limiter itself, in divertor tokamaks impurities originating on the divertor targets are usually well screened from the core, and core contamination is mainly due to processes occurring on other first wall components [56].

The role of the impurity species can be highlighted, in particular its atomic number Z. We have already shown how high Z elements, such as W, are desirable plasma facing components materials as they are less easily eroded. Furthermore, they are more easily ionized, meaning that after being eroded they will very quickly be driven again towards the surface, re-depositing in proximity of the erosion location. They will often experience the so called prompt deposition, where they are re-deposited within one Larmor revolution, also thanks to the fact that heavier atoms have a higher Larmor radius, increasing the chances of hitting the wall during the gyromotion. These are helpful features in the perspective of core screening, as heavy impurities are less easily transported. However, if they manage to cross the main plasma boundary, a heavy impurity is much more detrimental than a light one. In fact, recalling equation 1.16, radiation losses depend on the square of the effective atomic number in the plasma Z_{eff}. It can be defined as [57]

$$Z_{eff} = \frac{\sum n_i Z_i^2}{\sum n_i Z_i^2} = \frac{\sum n_i Z_i^2}{n_e} \tag{2.14}$$

Where Z_i and n_i are the atomic number and ion density of the i-th species, while n_e is the electron density. Further complexity is added to the picture by the use of extrinsic impurities in the divertor region. In fact, increasing radiation losses in this spot may be

helpful, in order to dissipate some of the heat load that would otherwise be focused on a tiny surface on the divertor. However, we must make sure that we are able to control the migration of these impurities, so that they do not cause significant core contamination. Migration in the scrape-off layer is still less understood than the transport in the main plasma [58], hence, improving our knowledge will be crucial to correctly predict the consequences of erosion and transport. Figure 2.3 shows some examples of global migration accounts attempted in three different tokamaks: TEXTOR [59], JET [54, 60] and ASDEX Upgrade [61].

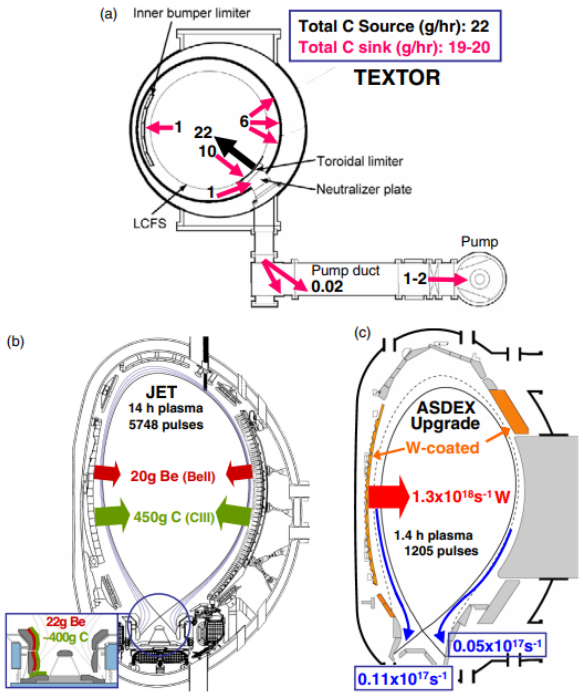

Figure 2.4: Examples of global impurity flows observed in different tokamaks. From [58]

2.2. The study of erosion and transport in tokamaks and linear plasma devices

The previous section presented the erosion mechanisms in magnetic confinement devices, as well as the following impurity transport process, highlighting how they could negatively affect the performance of the thermonuclear plasma. It should now be clear how a good understanding and control of these phenomena could be of interest, in the perspective of operating the next step device ITER, and even further towards a working nuclear fusion power plant. Therefore, plasma-wall interaction, and in particular erosion and core con-

tamination, is unsurprisingly a relevant field of research in the nuclear fusion scientific community. This section is devoted to presenting the available literature in the topic of erosion and migration, in order to contextualize the work presented in this thesis.
The study of erosion is challenging for many reasons. The process obviously depends on the plasma conditions, which can vary over a wide range, often within the same device. Geometries of machines and magnetic fields may also be very different, as well as the kind of materials employed. Further complexity is given by the insufficient comprehension of some mechanisms, such as migration in the SOL, and by the presence of transient events, known as edge localised modes (ELMs) and disruption, where violent outbursts of particles and heat fluxes towards the plasma facing components occur in tokamaks. Additionally, no machine operating today is able to reproduce all the conditions expected to be found in the next step device ITER; they may focus on matching some of the parameters, but will fall short in some others, making it difficult to extrapolate todays results to future, bigger devices. For instance, an experimental campaign carried out between 1999 and 2001 in JET , the largest existing tokamak, was composed of 5478 discharges for a total plasma time of 14 hours, a total energy of 220 GJ and $\sim 1.8 * 10^{27}$ total ion fluence of the divertor. Compared to ITER parameters, this equals about 125 ITER discharges in terms of time of operation, about 4 discharges in terms of energy and only one third of a discharge in terms of divertor fluence [62]. Moreover, it is also very difficult to assess experimental results in these complex machines. Erosion measures in tokamaks may be done after long experimental campaigns, comprising a large number of discharges often performed in different conditions, making it difficult to link a certain results with one or another parameter.
All these elements combined make it necessary to find complementary tools to better investigate these topics. In this sense, help comes from a different kind of machines, known as linear plasma devices (LPDs). These are very simple devices, whose general layout is usually constituted by a cylindrically shaped main chamber, with coils wrapped around to generate an approximately constant and straight magnetic field, directed along the cylinder axis. Although tokamak experiments remain of primary importance, LPDs have proven to be an extremely useful additional resource for many reasons [63]. In some cases they are able to reproduce conditions foreseen in ITER, particularly the ion fluxes and fluences, which are instead always one or two orders of magnitude lower in todays tokamaks. Moreover, their simplicity makes them more flexible and accessible, allowing better control of the exposure parameters and their independent variation to gain more insight on their effects. This also favors reproducibility of experiments and eases the gathering of experimental data, whereas in tokamaks the accessibility to diagnostics and samples analysis may be limited. They are also much more cost effective both in construction and

operation. Figure 2.5 shows an example of LPD: PSI-2.

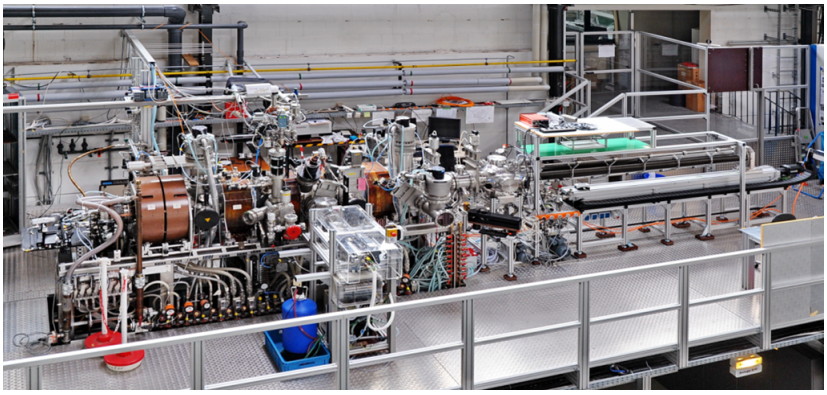

(a)

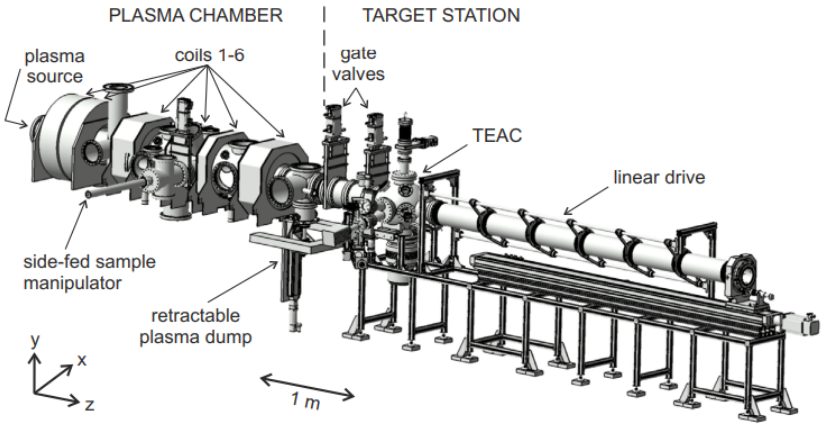

(b)

Figure 2.5: (a) A picture of the PSI-2 device located at Forschungzentrum Julich. (b) A pictorial scheme of PSI-2 [64]

The other way to help the study of erosion and migration phenomena is the development of suitable codes to simulate the process. An important example is represented by the ERO code [65, 66] and its enhanced version ERO2.0 [67], which will be presented in detail in section 3.1, as it plays an important role also in this thesis work. A reliable code with general validity would allow to gain much more insight than the often scarce experimental data alone. However, its accuracy only goes as high as our understanding of the involved processes and ability to reproduce them in the model, providing results far from reality when the model is not sufficiently complete. Therefore, working towards obtaining good agreement between the experiments and the simulations is essential in order to increase the reliability of the code, strengthening in turn our ability to predict future experiments,

also in view of the next step device ITER.
The next subsections will be dedicated to presenting the main studies on wall erosion and impurity migration, carried out in the experimental framework and in the modelling one, both on tokamaks and LPDs.

2.2.1. Experimental studies

This subsection will present the main experimental works about erosion and migration. In the tokamak world, the main active devices interested by this kind of studies are JET, the Tungsten Environment in Steady-state Tokamak (WEST) [68], and ASDEX Upgrade (AUG) [69]. This last one will be also the subject of part of this thesis work.
JET is the biggest existing tokamak and therefore the best available testbed for ITER among the present day devices, although still quite far from it in many ways. For this reason it was used to carry out tests in all relevant aspects of fusion research, including the plasma-wall interaction. In particular, first wall materials were investigated in JET, employing two different configurations throughout its operation, the so called JET-C and JET-ILW. The former refers to a full carbon (C) composition of the first wall, while the latter stands for ITER-like wall, as it is the wall configuration foreseen to be used in ITER, composed of a beryllium (Be) first wall and full tungsten (W) divertor. A picture of the two setups is reported in figure 2.6. A comparison of the two cases was made in [70], where material erosion and migration, fuel retention and impurity concentration were assessed. The results showed a much better behaviour of the ILW configuration, also highlighting the need to reinterpret former results in the C wall, where the influence of the PSI processes was underestimated. The erosion was greatly reduced due to the absence of low impact energy chemical sputtering processes, thus reducing the primary source of impurities and with it the migration from the main chamber towards the divertor, which was observed in JET-C. In turn, also the impurity content was found to be lower, yielding a $Z_{eff} = 1.2$ for D plasma in JET-ILW compared to the $Z_{eff} = 2$ observed in JET-C. Fuel retention was also improved with a reduction of a factor 10-20. Further results on JET-ILW were presented in [71], focusing particularly on the behaviour of the tungsten in the divertor. Gross erosion, measured through optical emission spectroscopy (OES), and net erosion, measured with post-mortem analysis, were assessed, highlighting the strong role of prompt re-deposition for W. The impact of ELM transient events was also investigated by separating their contribution to erosion with respect to steady state regime, and were found to be the dominant source of erosion in this kind of plasma.

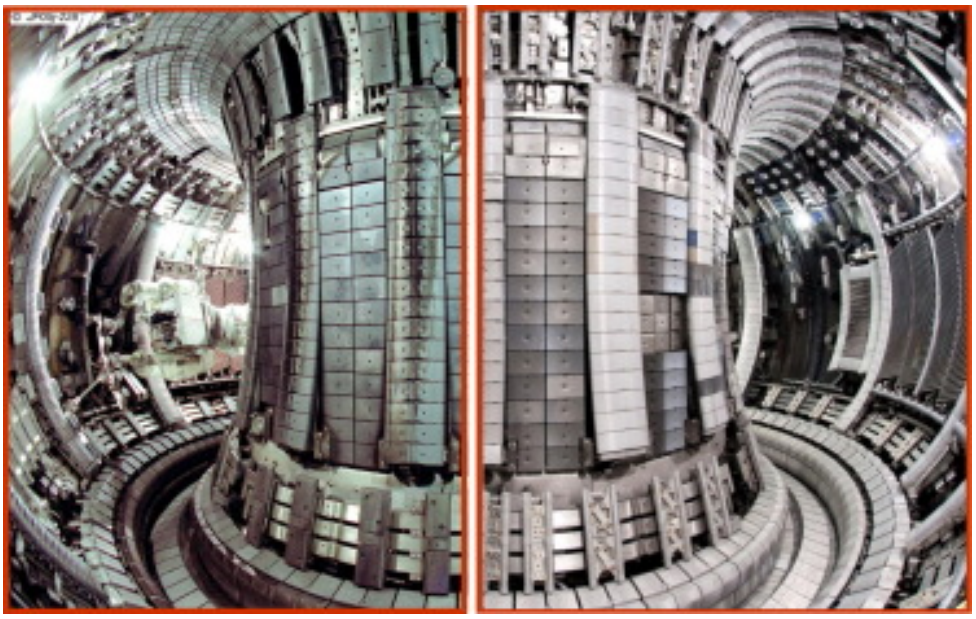

Figure 2.6: Pictures comparing all-carbon JET (JET-C) on the left, and JET equipped with ITER-like walls (JET-ILW), so with Be first wall and W divertor, on the right [70]

Tungsten was further investigated in full-W tokamak environments, such as the aforementioned AUG and WEST. A very complete description is given in [72], where experiments on both devices were presented, investigating many different aspects: gross and net erosion were evaluated during and outside of ELM events and the role of surface roughness was also inquired. Gross erosion was evaluated with the use of markers designed to locally minimize the prompt re-deposition, and its comparison with net erosion once again shows the importance of prompt re-deposition behaviour, which was also seen to increase with the electron density in the proximity of the wall. The analysis of ELM transients further evidenced the role of prompt re-deposition, where the gross erosion is enhanced by 1-2 orders of magnitude, while net erosion only goes up by a factor 2-3. The surface roughness was observed to impact the net erosion locally, suppressing it more on rougher surfaces, while also favoring the formation of thick co-deposited layers.
Helium (He) plasmas were also investigated in this study, and their behaviour was compared to the one of D plasmas. The study of He plasma will be a crucial piece of this thesis work, therefore it is worth explaining further the motivations behind the study of this plasma species. He is the reaction product of the D-T fusion reaction, hence its presence in the plasma is inevitable during the operation of a nuclear fusion reactor. In the perspective of correctly describing PWI, it must be studied how it interacts with the wall materials and its differences relatively to hydrogenic species, to be able to predict how a certain He content in the D-T plasma will affect erosion and transport mechanisms.

In general, He is expected to cause significantly higher gross erosion than the hydrogenic ions. This is due to the fact that its higher mass lets it sputter heavy material atoms such as W more easily. Moreover, the possibility to reach a higher charge state also doubles the energy gain in the plasma sheath potential drop, increasing its impact energy, which means further increasing the sputtering yield if we are on the increasing side of the curve, which is usually the case.
Going back to the results presented in [72], He plasma predictably were seen to increase the gross erosion compared to D plasma, as explained above. However, strong long range migration was observed towards the divertor region, as ion cyclotron resonance heated (ICRH) He plasmas were seen to produce much more W impurities from the main chamber with respect to D plasmas [73]. This produces the effect of turning some high gross erosion divertor regions into apparent net deposition zones. Results from AUG and WEST were also combined to give an estimate of the average net erosion rate in the range of $0.1 - 0.4 nm/s$, except for the strike point region where it may be higher. Further results on full W tokamaks, coherent with the ones presented, may be found in [74–76].
Linear plasma devices are specifically thought to investigate plasma-wall interaction, hence most of the experiments carried out in them are related to this specific topic. The main LPDs around the world are PISCES-A and B [77, 78] in the USA, NAGDIS-II [79] at Nagoya University in Japan, PSI-2 [64] at FZJ in Germany, Pilot-PSI [80] and Mangum-PSI [81], both in the Netherlands. A summary of their parameters may be found in [63]. It is worth mentioning the GyM linear device as well [82], located at ISTP-CNR in Italy, which will be a part of this thesis work. These devices have been employed to investigate many phenomena, trying to fill the gaps in PSI knowledge which were difficult to study in tokamaks, in particular, as mentioned before, with regards to the high fluence conditions expected in ITER and not replicable in existing tokamaks. Particular interest has developed around the role of morphology at the microscopic level, especially in the case of He interacting with W material. W exposed to He irradiation has been seen to undergo morphology changes, forming nanostructures called "fuzz" [83–85] at temperatures above 1000 K and He impact energies above 20 eV, although below the sputtering threshold. This highlights another important reason to study PWI relatively to a He plasma, as inducing these modifications may alter the behaviour of the material. The impact of morphology is also studied with respect to the resulting erosion, as shown in [86], the original morphology of the surface can affect the measured erosion, with the calculated effective sputtering yield being in general lower as roughness increases. Another topic studied in linear devices is the D retention in W materials and its comparison to the case where D plasma is seeded with He impurities, which has proven to reduce the retention effect [87, 88].

As was mentioned, it is important to combine experimental activities with modelling techniques to gain better insight, while also strengthening the accuracy of the model. The next subsection will shift the focus towards modeling studies performed in tokamaks and LPDs, which will also be the core of the present thesis work.

2.2.2. Modelling studies

This subsection aims at presenting the main modelling activities available in literature, focusing on the ERO code, and particularly on its updated version ERO2.0, which will be then described in more detail in section 3.1, being the key component of this thesis work. ERO is a powerful tool to simulate plasma-wall interaction in many different geometries, plasmas and wall materials, allowing to calculate erosion of plasma facing components, the migration of impurities in the simulation domain and many other relevant PWI phenomena. It is worth mentioning that along the ERO code, codes for the simulation of the boundary plasma are often used in combination with it, being able to provide a simulation of the plasma condition that can be used as an input to the background plasma used in ERO. An example of such plasma boundary codes is SOLPS-ITER [89].
The first version of ERO was developed in the 90s [65] and it was characterized by the possibility of simulating only small volumes, thus computing erosion and transport only locally, in the proximity of the wall surface. Nonetheless it has proven to be a useful resource to aid PSI experiments. A notable example can be found in [66], where the code is employed in its ERO-TEXTOR variant, specifically designed to simulate a volume near a limiter surface in the boundary layer of the TEXTOR tokamak. It was used to simulate the erosion of different material in different plasma conditions and compare the obtained results with experiments, finding good agreement.
The main enhancement of the 2.0 version concerns a great expansion of the simulation domain, making it possible to simulate even the full volume of the boundary of large machines, giving a much more complete description of long range phenomena. The first example was presented along the introduction of the new code in [90]. Here, The code was employed to simulate the boundary of JET-ILW in limiter configuration, assessing the erosion of Be and the contributions to it due to the D background plasma and the Be impurities self-sputtering. A comparison with a former study performed with ERO1.0 [91] was also evidenced. Further results on JET-ILW are presented in [92], where again erosion in limiter configuration was investigated, with emphasis on the role of Be self-sputtering and inquiring the role of D concentration in the wall surface, where a high erosion case, with 0% D concentration, and a low erosion case, with 50% D concentration, were examined. The study was also extended to diverted configurations for the first time,

where migration of Be towards the divertor regions was observed, particularly to the inner divertor, in agreement with experimental observations.

In [93] an ERO2.0 modelling of the WEST tokamak is presented, aiming at studying the contamination of the core with W impurities coming from PFCs erosion. The contribution of each PFC to the core contamination was studied, showing that PFC experiencing higher fluxes, like the lower divertor, are well screened and produce little contamination of the main plasma. On the other hand, other PFCs of the main chamber experiencing lower fluxes, while producing lower W impurities, they are less screened and strongly contribute to main plasma contamination. The effect of plasma density was also studied, examining two density scenarios. In agreement with former publications [94, 95], the high density case, compared to the low density one, leads to an enhancement of the erosion, thus of the W impurity sources, but the screening is improved and the core contamination is seen to decrease. The role of self-sputtering was also examined, evidencing very different consequences in the two density cases. In low density, self-sputtering slightly increases the erosion, but the self-sputtered particles are ejected with sufficiently high speed that core contamination significantly increases. In high density, prompt re-deposition is much more important, meaning that W impurities have less time to be ionized and gain energy in the plasma, so self-sputtering does not impact significantly neither the erosion nor the contamination.

ERO2.0 can be used also to predict erosion and migration in future machines, as it was done for the first time in [96] for ITER. This study was able to give an estimate of the erosion rate predicted to occurr in ITER, and also compare it to previous results obtained with the older ERO version [97, 98]. In ERO, Be impurity concentration was treated as a free parameter, and varying it significantly impacted the erosion and deposition results. In ERO2.0 instead, it is treated in a self-consistent way, being able to simulate the impurity production by plasma sputtering, their migration in the whole domain, the following deposition and the possible self-sputtering. The migration of Be was also assessed, finding that around 80% of Be re-deposits on the main chamber, while the remaining part migrates towards the inner and outer divertor approximately in equal parts, depositing near the strike points.

The use of ERO2.0 in linear plasma devices has been directed mainly towards the study of surface morphology studies. In [86, 99] simulations performed in PSI-2, with both D and He plasmas, can be found, aimed at modelling the effect of the surface roughness and morphology of Mo surfaces on the calculated sputtering yields, the angular and energy distributions of sputtered particles and their re-deposition patterns. A variety of different morphologies were investigated, both regular and stochastically constructed samples. The results showed that, in general, a rougher surface will tend to inhibit erosion, decreasing

the calculated effective sputtering yield. ERO2.0 also allows to describe the evolution of the surface morphology over time and it is generally observed that the surface peaks are preferentially eroded, while deposition occurs more in the valleys, leading to a flattening of the surface during irradiation. The results of the simulations were then validated through dedicated experiments, showing good agreement.
A similar study was presented in [100], again in PSI-2, but this time focusing on reproducing JET-ILW divertor conditions, thus employing W surfaces. In particular, surfaces representing the smooth Tile 5 W bulk and the rough Tile 6 W-coated CFC of the JET divertor were considered. Results are in line with the previous ones, showing a decrease of erosion up to 50% of Tile 6 with respect to Tile 5, and again the preferential erosion of the peaks and deposition in the valleys is observed.
Surface evolution was further analyzed in [101], where the evolution model implemented in ERO2.0 was compared with models available in literature, and its applicability domain was evaluated. Simulations were performed with He and Ar plasmas on W surfaces, both numerically generated and realistic ones, detected through AFM measurements. The smoothing process was again observed and it was stronger in the Ar case, due to the higher sputtering yield. He simulations could be compared with experiments, finding good agreement on the estimated erosion rates.
A different kind of ERO2.0 simulations in linear devices is proposed in [102]; here, unlike the other works where the focus is on surface morphology at the micro-scale, the simulation is performed over the whole volume of the GyM device, by coupling the plasma boundary simulation code SOLPS-ITER to ERO2.0. Global erosion rate, as well as the deposition patterns, were investigated in a He plasma, with varying biasing voltage applied to the PFCs, while also investigating different wall materials, namely C, Fe, Cu and W. This study will be explored more in depth in section 3.2, as it will be used as the basis of some of the work developed in this thesis.

2.3. Motivations and goals of the present thesis work

The main elements needed to understand the interest of the present thesis work have now been introduced. To summarize what has been presented so far, chapter 1 introduced the general framework of nuclear fusion, particularly the magnetic confinement approach, and presented the fundamentals of plasma-wall interaction in the boundary layer of magnetic confinement devices. Chapter 2 focused on the description of specific PWI phenomena, namely the erosion of the wall material and the following migration of eroded impurities in the plasma, highlighting their negative impact on a successful realization of a nuclear fusion reactor. First, the physics of erosion and migration processes was presented, while

then a focus on the study of these phenomena was given. In this context, the importance of linear plasma devices was highlighted, being able to investigate plasma conditions not replicable in the available tokamaks, which can be relevant to the next step device ITER, in a much simpler and more flexible environment. The crucial role of PWI simulation codes such as ERO2.0 was also underlined, as their coupling to experimental activities enables to gain better insight from them, while strengthening the ability to predict future experiments. Finally, an overview of the main works present in literature about the topic of erosion and migration was given, both by the experimental and by the modelling point of view.

The role of helium and the interest in studying He plasmas was also emphasized. He is the reaction product of the D-T reaction, therefore its presence in the plasma is unavoidable during the operation of a fusion reactor. Its greater mass with respect to hydrogenic species, coupled with its possibility to reach a higher charge state, make it more effective at sputtering heavier wall elements. Moreover, He has been observed to interact with fusion relevant materials, such as W, to produce peculiar nanostructures on the wall surface, that may alter the material properties. Thus, the investigation of PWI involving He plasmas is required to gain knowledge useful to future reactor operations.

Not many articles in literature deal with the topic of modelling the PWI in He plasma, especially with the global approach, made possible by ERO2.0, thanks to its much larger capabilities in terms of simulation volume relatively to its predecessor. Thus, this thesis work aims at covering this subject, employing the ERO2.0 code to simulate erosion and migration processes for a He plasma both in a tokamak environment and in a linear plasma device one.

Chapter 3 will be dedicated to present the main tools needed, starting from a description of the ERO2.0 code, and the strategies adopted to setup the simulations in the two machines of choice, namely ASDEX Upgrade for the tokamak part, and GyM as a linear plasma device.

Chapter 4 and 5 will then present the results of such simulations in GyM and AUG respectively.

In GyM, global erosion and deposition simulations will be performed, focusing on the effect of considering different wall materials and varying the bias applied to the PFCs. Another key aspect will be the introduction of an additional component in the simulation, namely the sample-holder, which was not present in previous studies, therefore a comparison between the two cases will be made. A part of the work will be dedicated also to local erosion simulations conducted at the micro-scale, to calculate the effective sputtering yields on a set of W samples with different morphologic characteristics actually employed in real experimental exposures in GyM, thus allowing to make a comparison and establish

a link between the modelling results and the experimental ones.
In the AUG tokamak, simulations will be performed over the whole boundary volume of the device, focusing particularly on estimating the net erosion of the outer divertor and comparing it to the experimental results. Preliminary simulations showed a large gap between the two, therefore most of the work will be directed towards exploring different parameters that may explain this difference and improve the agreement.

3 | Tools and simulation strategies

This chapter will define the tools employed in the modelling activity of this thesis work, in particular the characteristics and the working principle of the ERO2.0 code will be presented in section 3.1. Section 3.2 and 3.3 will be dedicated to describing the GyM device and the AUG tokamak respectively. They will also introduce the strategies adopted to simulate their environment in ERO2.0, while also presenting some preliminary data needed as the starting point of the results presented in the next chapters.

3.1. ERO2.0 code for the simulation of erosion and impurity migration

As already mentioned in the previous chapter, ERO2.0 is a 3D Monte Carlo code designed to simulate the erosion of the walls of magnetic confinement devices and the following migration of eroded impurities in the boundary plasma of said device. The general workflow of the code, depicted in figure 3.1, can be summarized as follows. The first part is made by the calculation of the PWI processes, such as reflection, physical and chemical sputtering, basing on databases such as SDTriSP or the Eckstein formula to retrieve the interaction data for a given projectile-target pair. In the second part, the code generates an ensemble of computational particles, called "test particles", representing the eroded impurities, accordingly to the calculated PWI processes. These test particles are followed in their trajectory inside the boundary plasma, which is determined by a set of deterministic equations, the ones describing the electro-magnetic fields interaction with charged particles, and stochastic ones, which describe processes such as ionization and recombination. The code also calculates further PWI processes caused by the traced impurities, e.g. self-sputtering, and the time step of the simulation ends when all the test particles terminate their migration by depositing on some surface. Following time steps may be simulated where the test particles will be generated accounting also for the PWI processes caused by the test particles of the previous step.

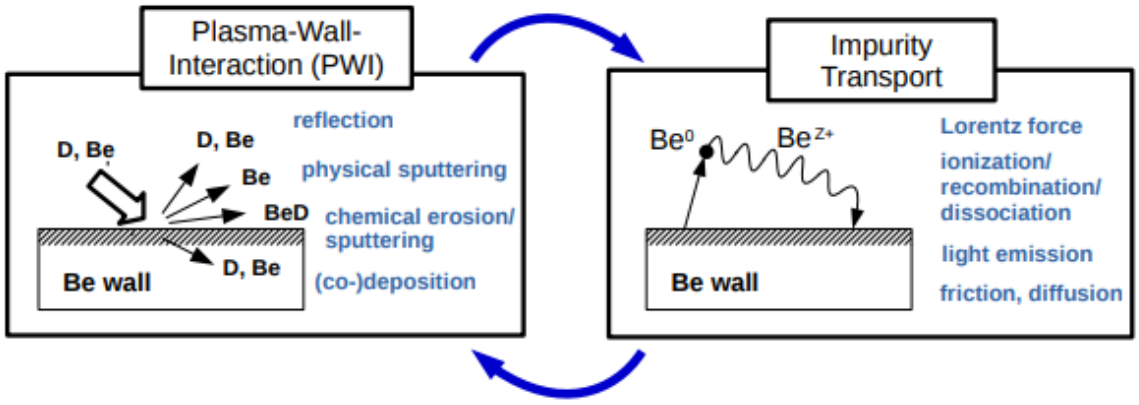

Figure 3.1: ERO 2.0 general workflow, with the example of D plasma irradiating a Be wall. [67]

The code works under the so called test particle approximation. This assumption considers the concentration of eroded impurities to be low enough that the generated test particles do not interact with each other, and also their influence on the electro-magnetic fields and the plasma parameters is neglected. It has generally proven to be a reasonable approximation in typical SOL conditions, producing results in agreement with experiments, although it may fail in case of intense impurity sources, such as when external injection is performed. The plasma therefore is unperturbed by the impurities and for this reason it is usually referred to as the background plasma.

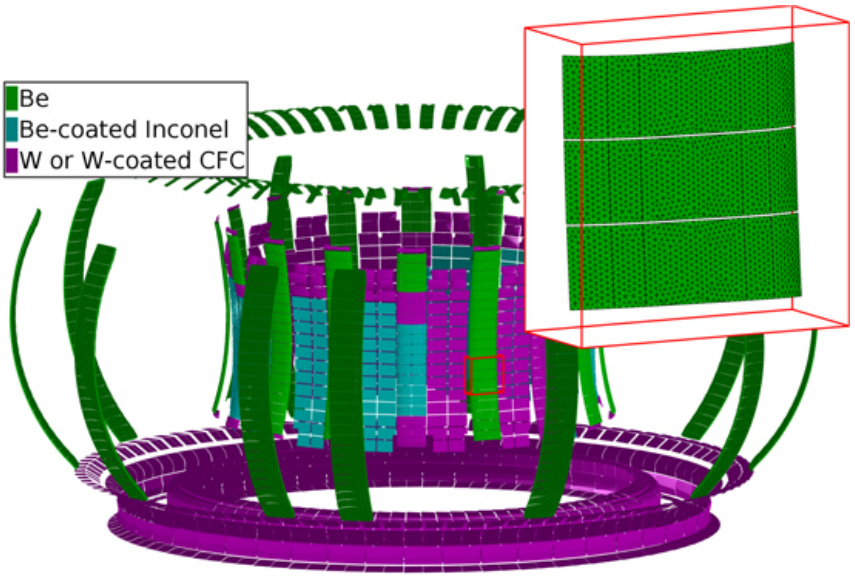

Figure 3.2: JET-ILW polygon mesh used for ERO2.0 simulations in [90]

The main ingredients needed as input in ERO2.0 to perform simulations are:

- **Background plasma**: The set of parameters describing the plasma in the simulation domain, the main ones being the electron density, the electron and ion temperatures and the fluid velocity. These data can be retrieved from experiments or can be modelled through dedicated boundary plasma codes such as SOLPS-ITER [89], EDGE2D-EIRENE [103], SOLEDGE2D-EIRENE [104] or EMC3-EIRENE [105].
- **Wall geometry**: The polygon mesh representing the surfaces of the 3D geometry of plasma facing components to be simulated. An example is given in figure 3.2, where the wall of JET used in [90] is represented.
- **PWI data**: The data needed to describe PWI processes, for instance the sputtering yields and the reflection coefficients, retrieved from known databases as explained above.
- **impurity transport model**: the model for the computation of the trajectory of impurities. It accounts for the ionization and recombination, whose rates are obtained from the Atomic Data & Analysis Structure (ADAS) [106]. It computes the gyromotion of particles through the Boris algorithm [107], which accounts for drifts and electric field forces, including the sheath potential, which is modelled according to [108]. Coulomb collisions and anomalous transport are also taken into account.

ERO2.0 is the enhanced version of the former ERO code. As anticipated, the main upgrade is the ability to handle much larger simulations volumes. Because of this, it is possible to shift from a local approach, where the simulations concern only a small volume in the proximity of a selected surface, to a global one, where the full volume of a machine can be simulated. The latter follows eroded particles everywhere in the boundary plasma, accounting for long range migration effect, while also allowing a self-consitent description of the impurities. In fact, in the previous ERO version, the content of impurities was a parameter to be imposed, whereas with the global approach it is an outcome of the simulation itself. Figure 3.3 shows a comparison of the simulation volumes of the two ERO versions.

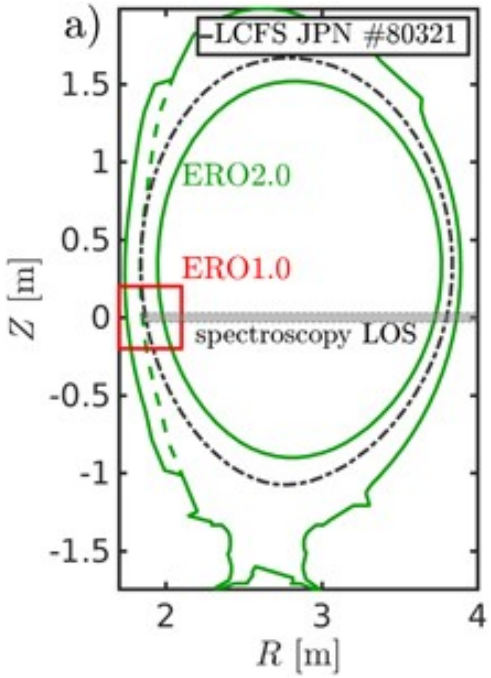

Figure 3.3: Comparison of the simulation volumes of ERO (red line) and ERO2.0 (green line) in JET. The dashed black lineline is the separatrix [90].

This increase in volume comes with a computational cost, since it means that particles must be traced in much longer trajectories and more of them are needed to obtain good statistics over the entire volume. Moreover, larger and more complex wall geometries are described and more data for the background plasma must be stored. For this reason, ERO2.0 was developed by a massive parallelization of the code, allowing to run it on supercomputers [67]. This is done through two popular standards for code parallelization: the Message Passing Interface (MPI)[109] and the Open Multi-Processing (OpenMP)[110]. In MPI, different processes are started simultaneously in different CPUs and are carried out indipendently, although each process has a unique ID used to identify which part of the global process it is and also used to communicate between different processes. OpenMP instead executes a principal process until a parallel region is entered, where the the master thread is forked into multiple ones and solved in parallel by different CPUs. Figure 3.4 shows a schematic of the working principle of the two approaches. Both are used in ERO2.0 and one can freely choose to shift more towards one or the other, as depicted in figure 3.5.

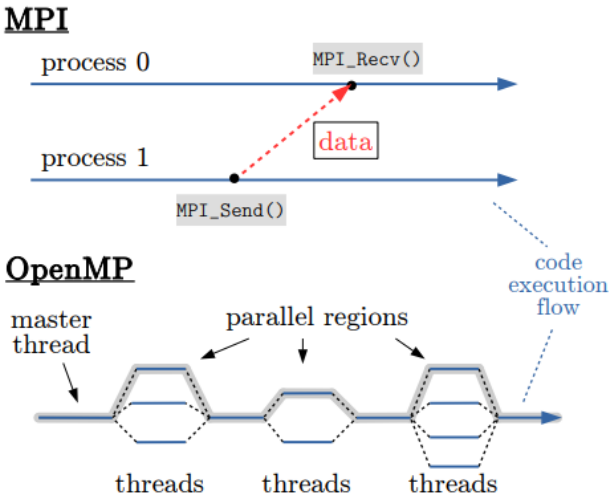

Figure 3.4: Schematic representation of the execution of MPI and OpenMP processes [67].

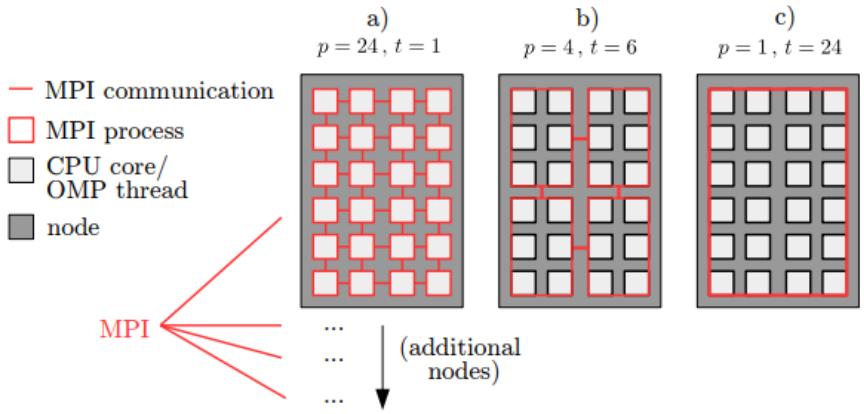

Figure 3.5: Different hybdridation of MPI and OpenMP. p is the number of MPI processes, t is the number of OpenMP threads per MPI process. The two extreme cases are (a) where each CPU in a node starts an MPI process and no OpenMP forking is used and (b) where just one MPI process is used in the whole node, leaving all CPUs available for OpenMP forking [67].

3.2. GyM linear device

GyM is a linear plasma device located at the Istituto per la Scienza e Tecnologia dei Plasmi - Consiglio Nazionale delle Ricerche (ISTP-CNR) in Milan. Like most LPDs, it is basically composed OF a cylindrical stainless steel vacuum chamber of 2.11 m in length and 25 cm in diameter, around which coils are placed to produce an approximately uniform axial field. Figure 3.6(a) shows a detailed scheme of the machine components.

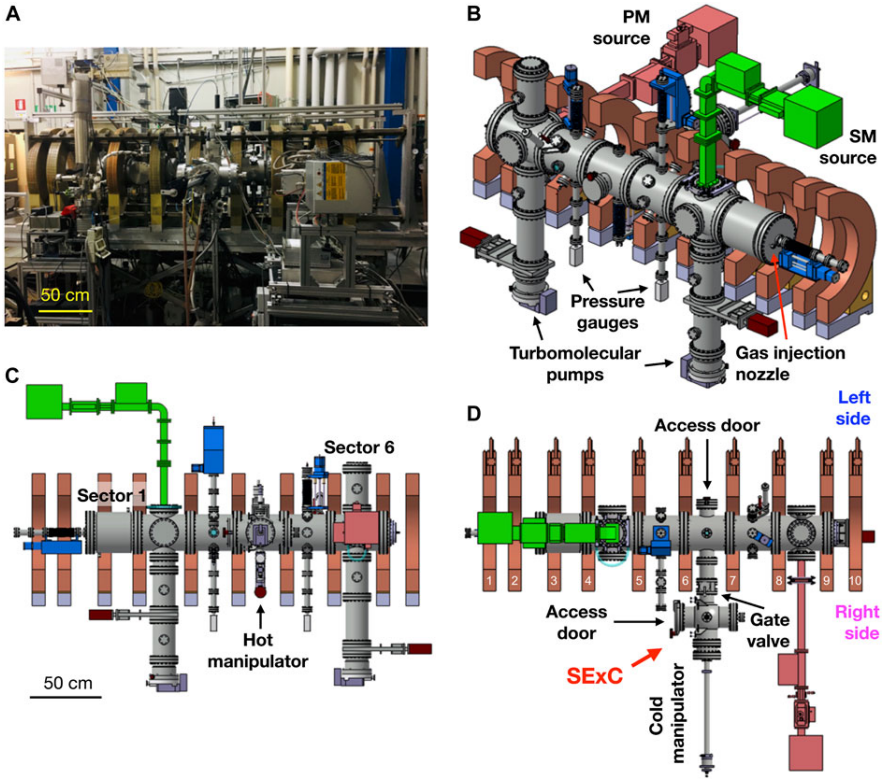

(a) A photograph (A) and schematic representation by different viewpoints (B-D) of the GyM linear device

Sources	2 Magnetrons at 2.45 GHz Power of 1.5 kW and 3 kW Steady-state
B field	≤0.13 T
Base pressure	5.0×10^{-6} Pa
Working pressure	1.0×10^{-1}–1.0×10^{-3} Pa
Electron density n_e	$\leq 1.0 \times 10^{17}$ m^{-3}
Electron temperature T_e	≤15.0 eV
Ion temperature T_i	≤0.1 eV
Ion flux Γ	$\leq 1.0 \times 10^{21}$ ions·$m^{-2}s^{-1}$
Ion fluence Φ After 7 h experiment	1.0×10^{25} ions·m^{-2}
Plasma diameter	0.25 m

(b) Main parameters of the linear plasma device

Figure 3.6: GyM linear plasma device layout and characteristics [82]

LPDs are thought as complementary devices to tokamaks, being able to test specific conditions, especially concerning particle fluxes and fluences, that may not be available in current tokamaks, but could be relevant to ITER and DEMO in the future. In ITER, an ion flux of $10^{25} m^{-2} s^{-1}$ is expected at the divertor [82]. The wall of the main chamber will

have to face a less extreme environment, although still demanding by the point of view of PWI. In particular, a flux of neutrals due to the charge exchange interaction of about $10^{21} m^{-2} s^{-1}$ is foreseen [111]. A similar value is obtained for the recessed elements in the first wall of DEMO [112]. Looking at the parameters of the GyM device reported in figure 3.6(b), we can see that the ion flux experienced in it is on the same order of magnitude. A full day (∼7 h) of operation yields a total fluence of about $10^{25} m^{-2}$, comparable to the one obtained in ITER after ∼50 discharges. The expected energy of charge exchange neutrals in ITER may also be replicated, by imposing a bias to the selected plasma facing component. Thus, assuming that ions and neutrals at the same energy behave in the same way in terms of PWI, which was concluded to be reasonable in section 2.1, GyM is a good testbed to mimic PWI occurring in the first wall of ITER and the recessed components of DEMO. The machine has been employed with a variety of gas, including hydrogen, deuterium, helium, argon and nitrogen, and even some mixtures, for instance nitrogen seeded deuterium plasma [82].

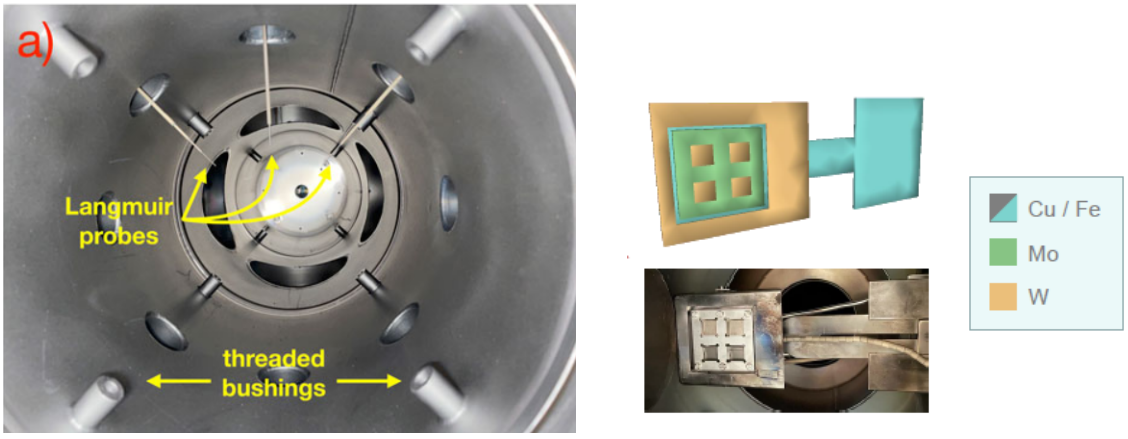

(a) (b)

Figure 3.7: Photographs inside of the GyM vacuum chamber (a) and of the sample-holder inserted in GyM (b) [82]

A photograph of the inside of the machine is reported in figure 3.7(a). It is possible to observe the main plasma facing components interacting with the plasma: the lateral wall of the cylinder, the two circular bases at the extremes and a set of threaded cylindrical bushings extruded from the lateral wall. These are the plasma facing components modelled in the global erosion study presented in [102]. In reality they are made of the AISI 304L stainless steel, although in the study they were considered made of a single element, and different elements were investigated, particularly C, Fe, Cu and W. It is possible to note that, as the magnetic field lines are directed axially, they never impinge on the lateral

wall. This implies that in ERO2.0 simulations the lateral wall is never directly eroded by the background plasma, but only by the impurities initially eroded from other PFCs. On the other hand, the bases and the bushings are eroded by the plasma, and a variable biasing voltage is applied to them in the simulations to tune the impact energy of the ions, observing its effect on the erosion.
During PWI experiments, another plasma facing component is introduced in the plasma volume: the sample-holder. It is the device used to carry the samples studied in experiments. It was not described in [102], therefore part of the aims of this thesis is to include it in the simulations and compare them with the previous results. As shown in figure 3.7(b), the sample-holder can be considered composed of four main elements. The support is the element that connects with the lateral wall and is made of the same material of the main chamber, which is indicated as Fe or Cu in the picture, as these will be the materials considered in this thesis. An external tantalium (Ta) mask is present, although in ERO2.0 is modelled using W as a proxy for high Z elements like Ta. There is then an internal molybdenum (Mo) mask, which directly holds the W samples, as W is the main material examined in these experiments. The Mo mask and the W samples can be biased in real experiments to select the impact energy on the samples, therefore also the simulations will include an analysis of a variable bias applied to these components and comparison with the same biases applied to the bases and bushings like in [102].

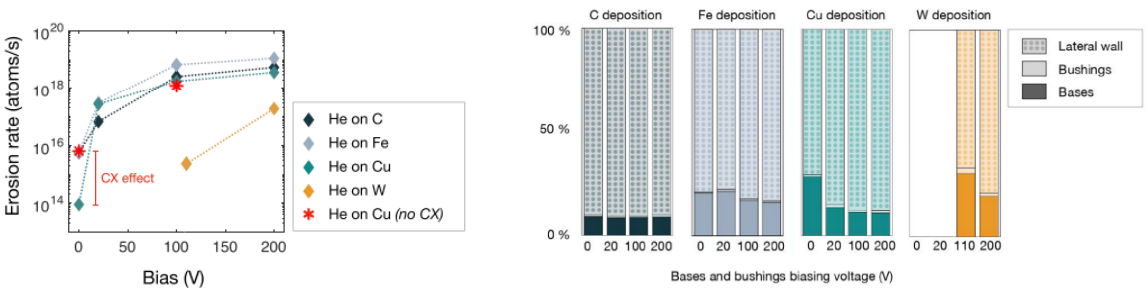

(a) (b)

Figure 3.8: Global erosion rate (a) and deposition distribution (b) in GyM with varying bias for different wall materials [102]

Some results about erosion and deposition from the previous publication are shown in figure 3.8. Figure 3.8(a) shows the global erosion rate in terms of particles/s at varying bias applied to the bases and bushings for the different materials inquired. Similar results were found for C, Fe and Cu, where the erosion rapidly increases at lower biases, while tending to saturation at higher ones, reflecting the energy dependence of the sputtering yield. W

shows a different behaviour, as its higher sputtering energy threshold completely prevents erosion at biases below 110 V. Moreover, the lower sputtering yield of He on W results in a significantly lower global erosion rate. Figure 3.8(b) instead focuses on the deposition of eroded impurities, focusing on how they distribute on the PFCs. Due to the long and narrow geometry of the vacuum chamber cylinder in GyM, most eroded impurities end up striking the lateral wall. It can also be noted that the share of deposition on the lateral wall increases with the bias, which can be attributed to the fact that at higher biases the impurites are ejected with higher energies, traveling faster to the lateral wall and having less time to be ionized and re-directed along the magnetic field lines. This does not occur for C, because in that case the ejection energy is maxed out already with no bias applied and the share of impurities depositing on the wall does not increase.
It is important to note that these simulations are performed using a background plasma retrieved by SOLPS-ITER, which is a 2D plasma boundary simulation code. Its results are produced over a 2D mesh which lies in the (R,z) plane, z being the cylinder axis direction, in cylindrical coordinates. On the other hand, ERO2.0 is a 3D code, therefore the coupling between the two is obtained by assuming rotational symmetry and interpolating the SOLPS quantities over a full (R,Φ,z) domain. It must also be specified that simulations including the sample-holder as a PFC will use a similar background plasma, that does not account directly for its presence, although with some benchmarking of the plasma parameters with experimental measures to improve the accuracy.
Figure 3.9 shows some preliminary results of simulations performed including the sample holder, presented at 19th International Conference on Plasma-Facing Materials and Components for Fusion Applications (PFMC-19)[113], useful to introduce the results presented in chapter 4. As the previous study, the main parameters of interest are the biasing voltage and the wall material. The investigated wall materials are Fe and Cu for the vacuum chamber components, while the sample-holder elements are modelled with W and Mo as previously described. Differently from the previous study, here the biasing voltage is applied to the W samples and the Mo mask of the sample holder, as it is in the experiments. Figure 3.9(a) and (b) show the resulting erosion rates of two specific PFCs: the samples and the lateral wall respectively. The samples are of interest since they are the subject of experimental studies; the lateral wall instead is not eroded directly by the plasma, thus it is interesting to study the erosion caused by impurities. Figure 3.9(c) shows the deposition distribution similarly to the one presented in figure 3.8(b). The same behaviour at increasing bias is observed for W and Mo impurities, as the share of deposition on the lateral wall increases. It is not observed for Fe/Cu impurities though, this is due to the fact that in this case the bias is applied to Mo and W components only, thus not affecting Fe/Cu deposition behaviour. These aspects will be recalled in chapter 4 as these results

will be further developed by the work done in this thesis.

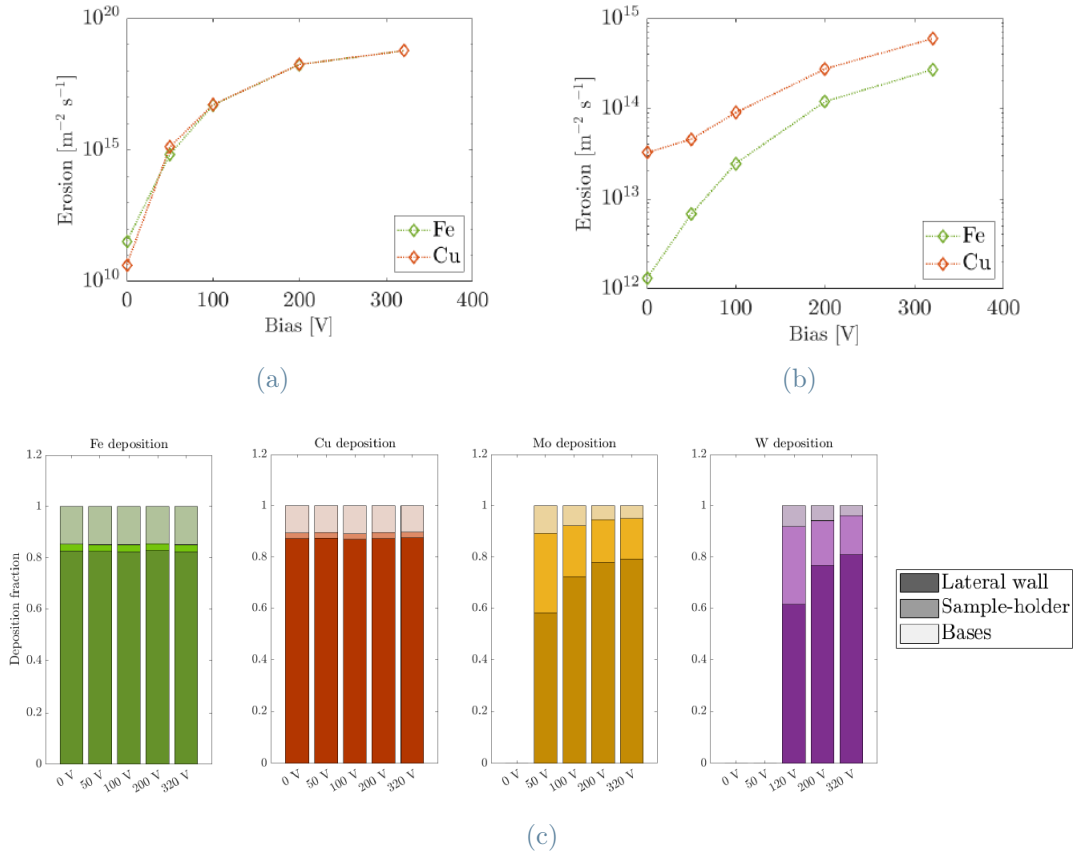

Figure 3.9: Erosion rates for the samples (a) and the lateral wall (b), deposition distribution of impurities (c) in presence of the sample-holder [113]

A part of this thesis work will be carried out in the local framework as well. These simulations are setup in a different way. The modelled surface is just a tiny spot on the samples, for instance a square of 20x20 μm, while the simulation volume extends for 100 μm inside the plasma. At this scale, it is possible to evaluate the morphology of the samples, which is detected through atomic force microscopy (AFM) and reproduced in ERO2.0. The background plasma is composed of fixed plasma parameters, coherent with the GyM typical conditions. The goal of these works is to simulate the erosion and the migration of impurities, evaluating the fraction of eroded particles that leave the simulation boundary in the direction perpendicular to the surface, which are considered to not be re-depositing on the sample. An effective sputtering yield (Y_{eff}) is thus determined by calculating the ratio between the flux of eroded particles leaving the boundary and the flux of plasma ions striking the surface. Then, the effect of different morphology on

this quantity is observed, by calculating Y_{eff} for samples with different morphologies, and a comparison with the experiments is made by comparing it with a Y_{eff} retrieved from mass-loss measures on the samples.

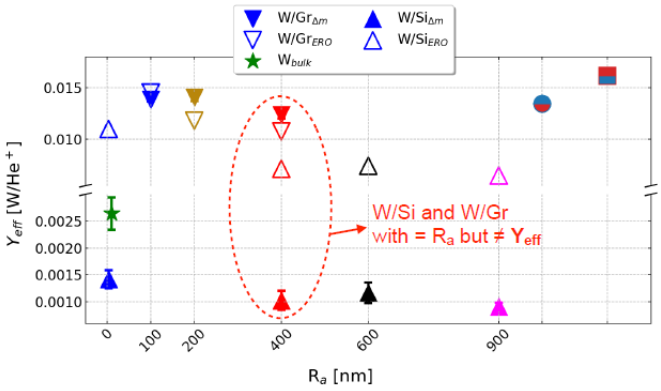

(a)

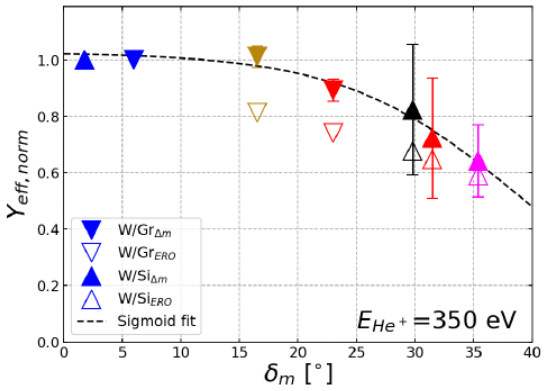

(b)

Figure 3.10: comparison of experimental and simulated Y_{eff} as a function of roughness (a) and as a function of the mean surface inclination angle, in this case normalized to the Y_{eff} of the flat samples [114]

Figure 3.10 shows results obtained with this kind of simulations, presented at PFMC-19 [114]. Here, two sets of samples were investigated, one composed of W coatings on graphite substrates, the other made of W coatings on Si substrates. Figure 3.10(a) shows the comparison between the effective sputtering yield calculated throgh ERO2.0 ($Y_{eff,ERO}$) and the experimental one ($Y_{eff,\Delta m}$) for each sample, as a function of its surface roughness. $Y_{eff,ERO}$ proved to significantly overestimate $Y_{eff,\Delta m}$ for W/Si samples, while accidental good agreement was found fo W/Gr samples, suspected to happen because $Y_{eff,\Delta m}$ in this case was greatly enhanced by some spots where the W coating was depleted and di-

rect sputtering of C occurred, although this is still an ongoing investigation. The surface roughness proved to not be a good predictor of the effective sputtering yield, as it can be seen that different samples with the same surface roughness provided different Y_{eff}. A more meaningful dependence was found by considering the mean surface inclination angle, reported in figure 3.10(b). Here the effective sputtering yields, normalized relatively to the flat samples, show a decreasing trend at increasing mean surface inclination angle. Section 4.4 will present the results of similar simulations on a set of samples consisting of films made of W and W with some oxygen content, deposited on polished Mo substrates, which have been employed in experimental campaigns in 2023. Hence they will be useful as a link between simulations and experimental results.

3.3. ASDEX Upgrade

ASDEX Upgrade is a medium sized tokamak located at the Max Planck Institute for plasma physics in Garching, Germany, which has been operating since 1991, as a successor of the ASDEX experiment, which was active in the decade before. It is characterized by a major radius of 1.6 m and a minor one of 0.5-0.8 m, for a total plasma volume of about 13 m^2. The maximum confining field is 3.1 T and typical tokamak plasma densities of $\sim 10^{14} cm^{-3}$ are achieved. Pulse length is on the order of 10 s, while the total heating power is 27 MW, subdivided in 1 MW of ohmic heating, 20 MW of neutral beam injection and 6 MW of ion cyclotron resonance heating (ICRH), or alternatively electron cyclotron resonance heating (ECRH).

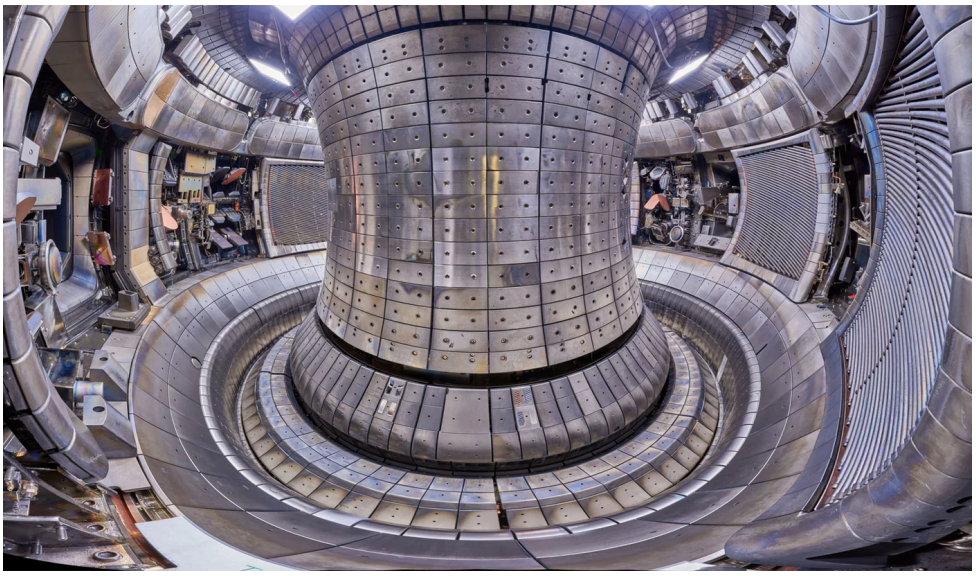

Figure 3.11: Photograph inside Asdex main chamber [115]

The goal of this study is to recreate through ERO2.0 the PWI processes experienced during real He plasma discharges, specifically the #36687 discharge performed in 2019 and the #41480 discharge performed in 2022, which will be now briefly described. These discharges belong to the L-mode type, which stands for low confinement, whereas high confinement ones (H-mode) also exist. This distinction refers to the confinement regime applied to the plasma. L-mode is the basic operating mode of a tokamak, where the confinement time is seen to decrease with the heating power, partially deleting the benefits of additional heating; however, above a certain power threshold, a transition occurs towards the H-mode, where a sudden doubling of the confinement time is observed. However, this operating regime carries some drawbacks, for instance the aforementioned ELM transient events arise in H-mode operation. Thus, L-mode discharges, like the ones of this study, are characterized by lower heating power and confinement time, and by the absence of transient events.
The two discharges share many characteristics, for this reason they are studied together, as they are thought to produce similar results. Table 3.1 presents the main global parameters, where it can be noted that most of them are very similar for the two discharges, particularly the magnetic field B_t, the plasma and ohmic currents I_P and I_{OH}, the safety factor at the 95% flux surface q_{95} and the discharge duration. Some discrepancy instead is found in the total heating power, obtained for both discharges through a pair of ECRH sources, and in the electron density n_e, which are both higher in the 2019 discharge by about 20% and 50% respectively.

	#36687 (2019)	**#41480 (2022)**
$\mathbf{B_t}$	-2.500 T	-2.523 T
$\mathbf{I_P}$	0.795 MA	0.795 MA
$\mathbf{I_{OH}}$	2.38e+04 A	2.49e+04 A
$\mathbf{q_{95}}$	5.160	5.286
$\mathbf{n_e}$	6.87e+19 m^{-3}	4.57e+19 m^{-3}
Flat top start	1.269 s	1.256 s
Flat top end	7.502 s	6.919 s
Heating power	1.323 MW	1.087 MW

Table 3.1: Main parameters of the #36687 and #41480 ASDEX Upgrade L-mode discharges.

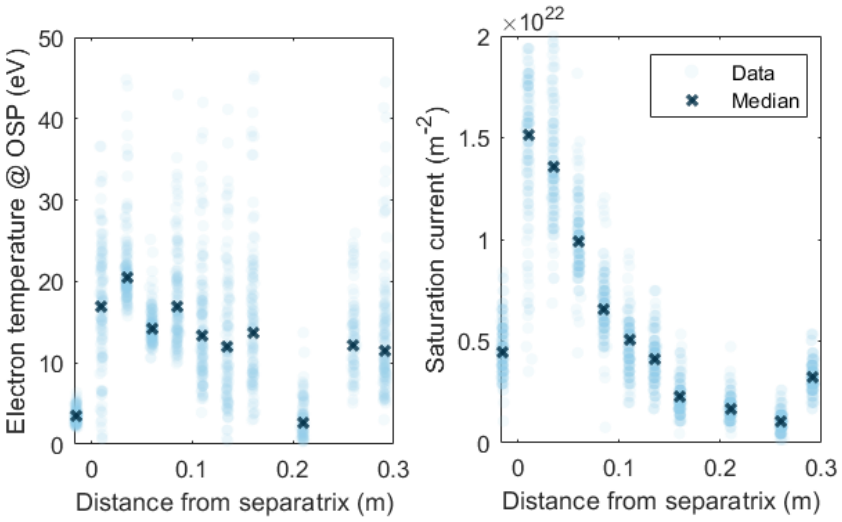

Figure 3.12: Experimental electron temperature and saturation current at the outer strike point in the 2019 #36687 discharge.

Like in the GyM simulations, the input background plasma is produced through the SOLPS-ITER code. To obtain an accurate plasma simulation, experimental data were taken at the outer strike point (OSP) and at the outer midplane (OMP), with the aim of reproducing the observed profiles in SOLPS. Figure 3.12 shows the experimental electron temperature and saturation current measured at the OSP for the 2019 discharge. Due to the similarity between the two discharges, the modelling of the background plasma was focused mainly on the 2019 discharge, although a more correct description of the 2022 discharge may be an interesting development for the future.

A presentation given at the 33rd Meeting of the ITPA Scrape Off Layer and Divertor Topical Group [116] showed some results of simulations performed in this framework, examining in particular the role of the charge state of the plasma He ions. Erosion simulations were performed considering three different scenarios: erosion by a full He^+ plasma,by a full He^{2+} plasma and by a realistic case with distributions of the two species retrieved from SOLPS. Figure 3.13 reports the plasma parameters produced by SOLPS and employed in the simulations, plotted along the poloidal profile of the divertor. The T_e profile was obtained by matching the experimental measures shown in figure 3.12(a), while T_i is purely an outcome of the SOLPS simulation, without experimental benchmarking. The electron density n_e is computed considering only the He^{2+} component, which constitute the vast majority of the background plasma, however this leads to a slight underestimation of n_e, especially near the OSP where the He^+ fraction is larger. This aspect may be improved by considering effective mass (M_{eff}) and atomic number (Z_{eff}) distributions in the volume, as will be done in section 5.3.

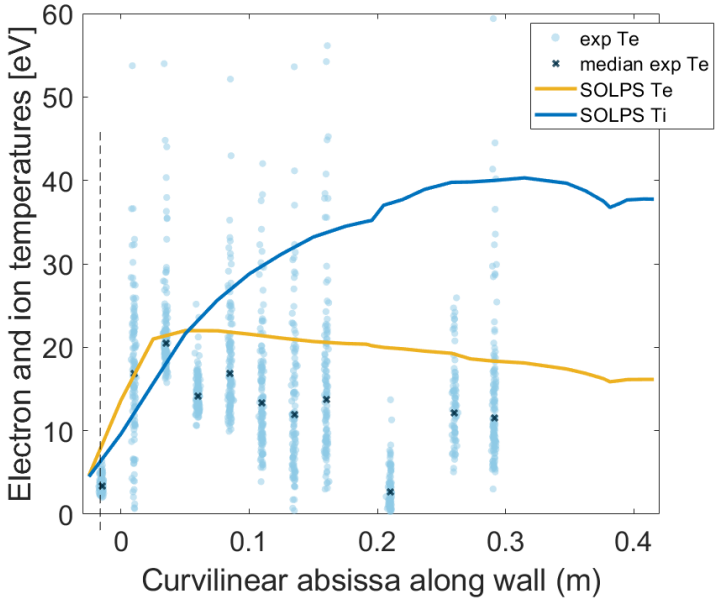

Figure 3.13: SOLPS-ITER profiles for the electron and ion temperatures, along the poloidal profile of the outer divertor, where the origin is in the strike point. The experimental data of the electron temperature at the outer divertor is also reported for reference.

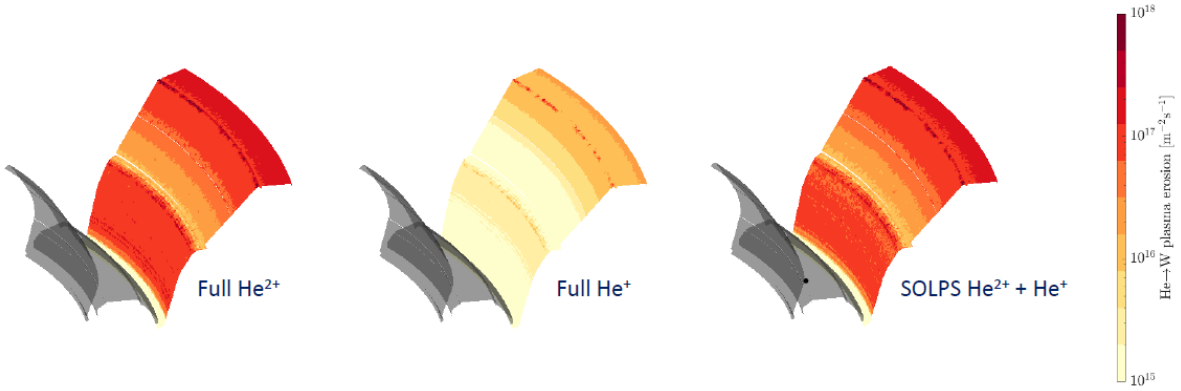

Figure 3.14: Outer divertor 2D gross erosion profile for the three cases: full He^+ plasma, full He^{2+} plasma and a mix of the two as described by SOLPS-ITER[116]

The results of these three simulations are shown in figure 3.14, where the erosion of the outer divertor in a 30° toroidal sector is depicted. Little difference is found between the realistic case and the full He^{2+} case, with the latter giving a slight overestimation of about 15% near the strike point, and even less farther from it. On the other hand, the full He^+ case provides a strong underestimation, by a couple of orders of magnitude.
The next step is to compare the outer divertor net erosion predicted by ERO2.0 with

the one measured experimentally during the two examined discharges. The experimental data consist of a reference value in the proximity of the outer strike point, which is in the order of 50 nm. This data was retrieved from the measures on a marker which could be assumed to be unaffected by the influence of other discharges performed in the same experimental campaign, unlike other markers where disentangling the contributions of different discharges may be difficult.

Preliminary simulations were carried out considering the erosion from both He species and under the assumption of fixed incidence energy and angle. The energy is considered equal to the mean impact energy expressed in equation 1.39, thus proportional to T_e and T_i, while the angle is a value of choice, and a parametric scan was performed in the range 72°-84°. Outer divertor gross erosion computed by these simulations is reported in figure 3.15. It easily notable that the erosion is heavily sensible to the incidence angle, as it increases by a few orders of magnitude when going from grazing towards normal incidence in the selected range.

However, considering the net erosion, in terms of eroded thickness after the total fluence experienced in the discharges, the results are very far from the experimental reference, greatly underestimating it. Even considering the highest erosion case, with 72° fixed angle, the net erosion is around 0.25 nm, a factor 200 lower than the reference.

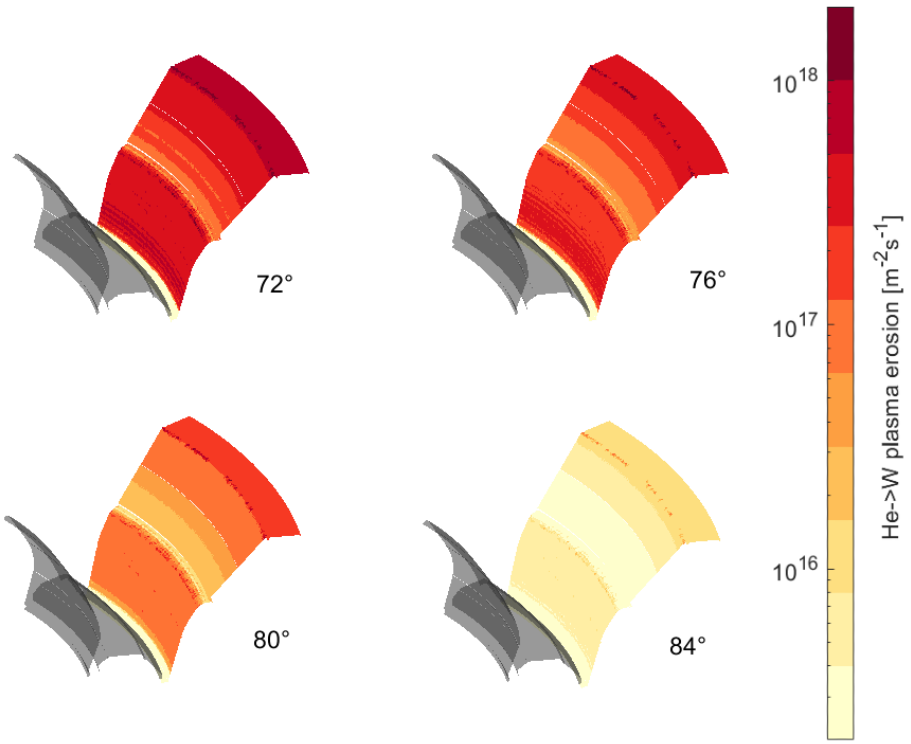

Figure 3.15: Outer divertor gross erosion at different fixed incidence angles [116].

The agreement between simulations and experiments must be improved, by considering different simulation paremeters that may explain this large gap. The first attempt at doing this was made by relaxing the fixed incidence energy and angle assumption, and considering more refined models, where both quantities are sampled by a Maxwellian distribution. Figure 3.16 shows the obtained net erosion profiles in 1D along the poloidal profile of the outer divertor, presented at CMD30 FisMat 2023 Joint Conference [117]. Three simulations are reported in figure 3.16: the first is again the one with fixed energy and angle at 72°, the second is performed with a maxwellian energy distribution but still fixed angle, while the third performs a maxwellian sampling of both energy and angle. Results show some progress in the right direction, with an increase of the net erosion by a factor 5 between the first and third simulation, although still below the reference by a factor 40.

Chapter 5 will present further results aimed at closing this gap, while also evaluating the evolution of the erosion profile with multiple time-steps simulations and examining the effect of considering realistic effective mass and atomic number distributions in the plasma volume.

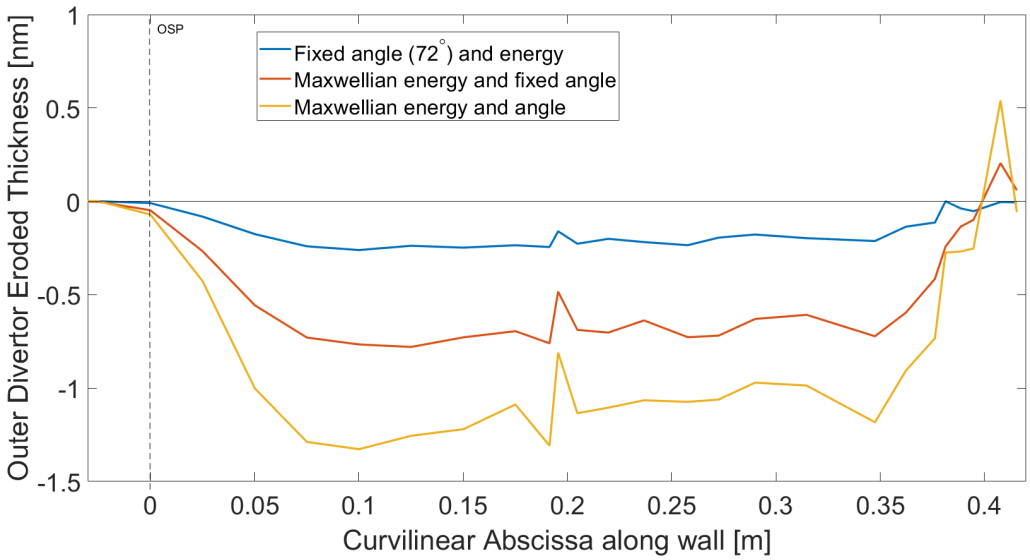

Figure 3.16: 1D net erosion profile along the outer divertor for different incidence energy and angle models.

4 | He plasma erosion simulations in GyM linear device

This chapter presents the results obtained in the ERO2.0 modelling activity for the simulations of the PWI processes in the linear plasma device GyM. As introduced in section 2.3 and 3.2, the simulations are performed with a He plasma, both in a global and in a local framework. The global approach aims at evaluating PFCs erosion while simulating the whole plasma volume, and particular focus is given to the effect of varying the bias applied to the PFCs, hence the ion impact energy, and to the employed wall material. The presence of an additional PFC, the sample-holder (SH), will also be considered, and comparisons will be made with a previous publication [102] in which it was not taken into account. The erosion of the lateral wall will be evaluated in section 4.1, the erosion of the samples in section 4.2, while section 4.3 will provide results about impurity deposition. The local erosion simulations, presented in section 4.4, focus on a small volume at the micro-scale, in the proximity of the surface of the W samples. Their aim is to evaluate the effect of different surface morphologies on the effective erosion, while also providing a comparison with experiments.

4.1. Global erosion results on the lateral wall

4.1.1. Material and bias investigation in sample-holder configuration

The lateral wall is a peculiar component of the GyM device. It is by far the largest in terms of surface extension, and due to the long and thin geometry of GyM, it is the recipient of most impurities eroded from the other PFCs, as highlighted by the deposition results reported in section 3.2. On the other hand, the magnetic field lines run parallel to the lateral wall surface in GyM, without ever crossing it; this implies that plasma ions are never directed towards it, thus the lateral wall is not eroded directly by the plasma, but its erosion is entirely due to the impurities coming from other PFCs. For this reason it

is interesting to observe how the gross erosion of the lateral wall changes when applying a bias to other PFCs like the bases, the bushings and the sample-holder. Moreover, this enables to make some comparisons between the kind of simulations performed in [102], where the SH was absent and the bias was applied on the bases and bushings, and the new ones in which the presence of the SH is accounted for and the bias is applied to it, specifically to the Mo mask and to the samples.
Two wall materials have been investigated: Fe and Cu. Fe is the main element in the stainless steel of the main chamber, while Cu is chosen as a proxy of other steel elements. This material refers to the bases, the bushings, the lateral wall and the sample-holder support, while the W and Mo sample-holder components are kept fixed with those materials. Five biases are also investigated: 0, 50, 100, 200 and 320 V. Actually, in simulations with bias on the SH, the 100 V simulations is instead performed at 120 V. This is done in order to be slightly above the W sputtering threshold, however we will see that this difference does not impact the general meaning of the results.

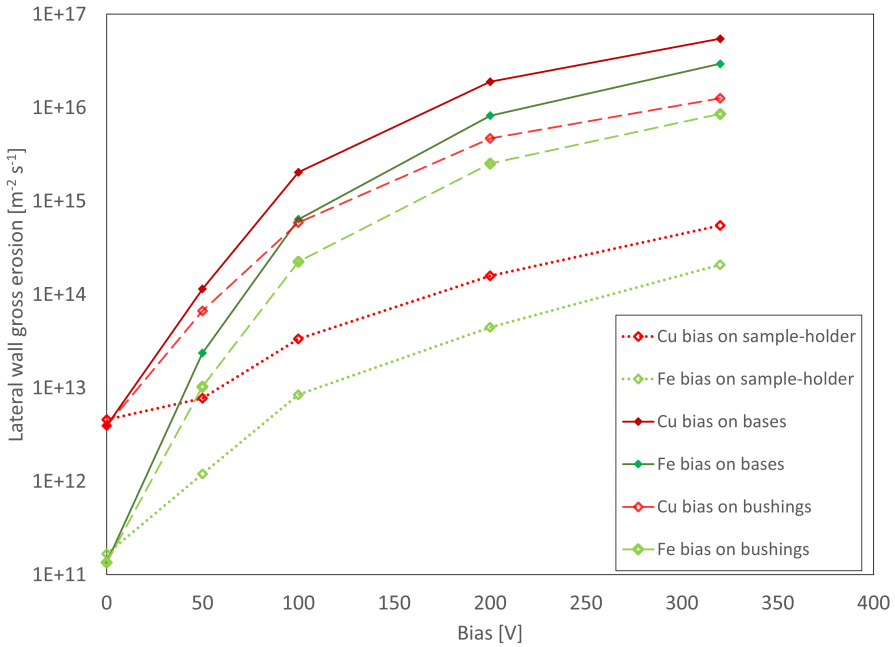

Figure 4.1: Lateral wall gross erosion for Fe/Cu wall configuration as a function of the biasing voltage, applied either to the sample-holder, the bases or the bushings.

To summarize, simulations with two materials and five biases, for a total of ten, are performed. This is repeated applying the bias to different PFCs, namely the bases, the bushings and the SH, totaling thirty simulations. The simulations in which the bias is

applied to the bases or bushings are carried out in absence of the SH, to reproduce the conditions studied in the previous work and allowing to compare them with the new ones. The lateral wall gross erosion retrieved from these simulations is reported in figure 4.1.

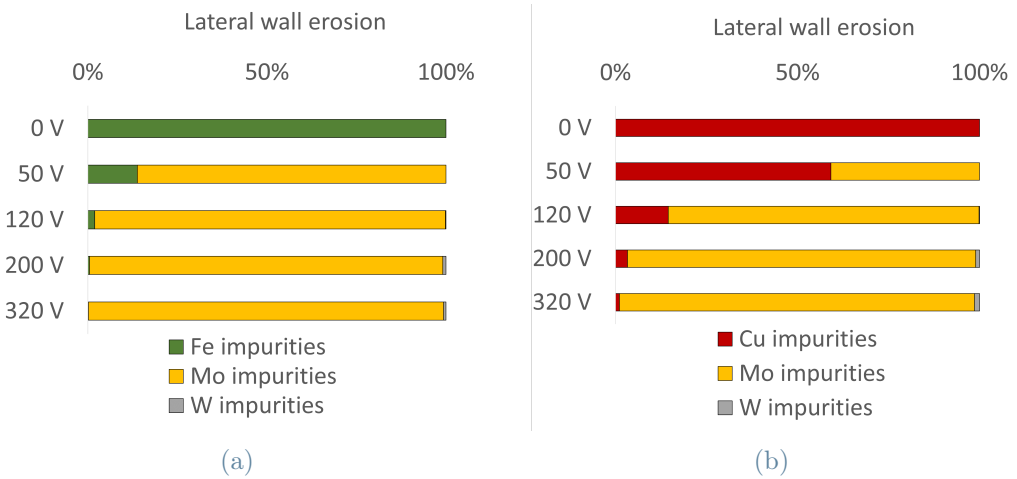

Figure 4.2: Contribution to the lateral wall erosion of each impurity species at the different biases in the SH configuration. Fe wall in figure (a), Cu wall in figure (b).

The first thing to note is that at 0 V the effect of the bias applied to different PFCs is absent, all the curves referring to same material almost coincide. The only difference observed is given by whether the SH was present or not. In fact, the presence of the sample-holder means an additional source of impurities that causes an enhancement of the lateral wall erosion, by about 15-20%. It must be precised that at 0 V the He ions impact energy is below the sputtering threshold of Mo and W, hence the only additional source of impurities is the support of the SH, which is made by Fe/Cu.
The bases and bushings curves share a similar shape, reflecting the typical energy dependence of the sputtering yield. In fact, as the bias increases, so does the He impact energy and consequently the Fe/Cu impurity source, according to the He on Fe/Cu sputtering yield curve; in turn, a higher production of impurities results in a higher lateral wall erosion. The bases curves yield a higher erosion with respect to the bushings ones, mainly due to the fact that the biased surface of the bases is bigger, hence it leads to a higher impurity source.
The SH curves instead are shaped differently. In this case, the bias is applied to Mo and W components which are not sputtered at 0 V, where the lateral wall is eroded only by Fe/Cu impurities. Then, the Mo and W sources are introduced as the relative sputtering thresholds are crossed, and their strength increases with the bias, while the initial Fe/Cu

source is held constant. This causes the different shape at the lower biases, in the Mo and W sputtering threshold region, while the sputtering yield-like trend is retrieved at the higher bias, reflecting the Mo and W sputtering yield curve. At higher bias the SH curves show a much lower lateral wall erosion than the others, by a few orders of magnitude, because the lower Mo and W sputtering yields compared to Fe/Cu, coupled with a smaller biased surface, lead to a smaller impurity source.
Overall, the Cu wall simulations provide a signifcantly higher erosion than the Fe wall ones. In particular, at 0 V it is higher by more than an order of magnitude, while at higher biases this difference narrows.

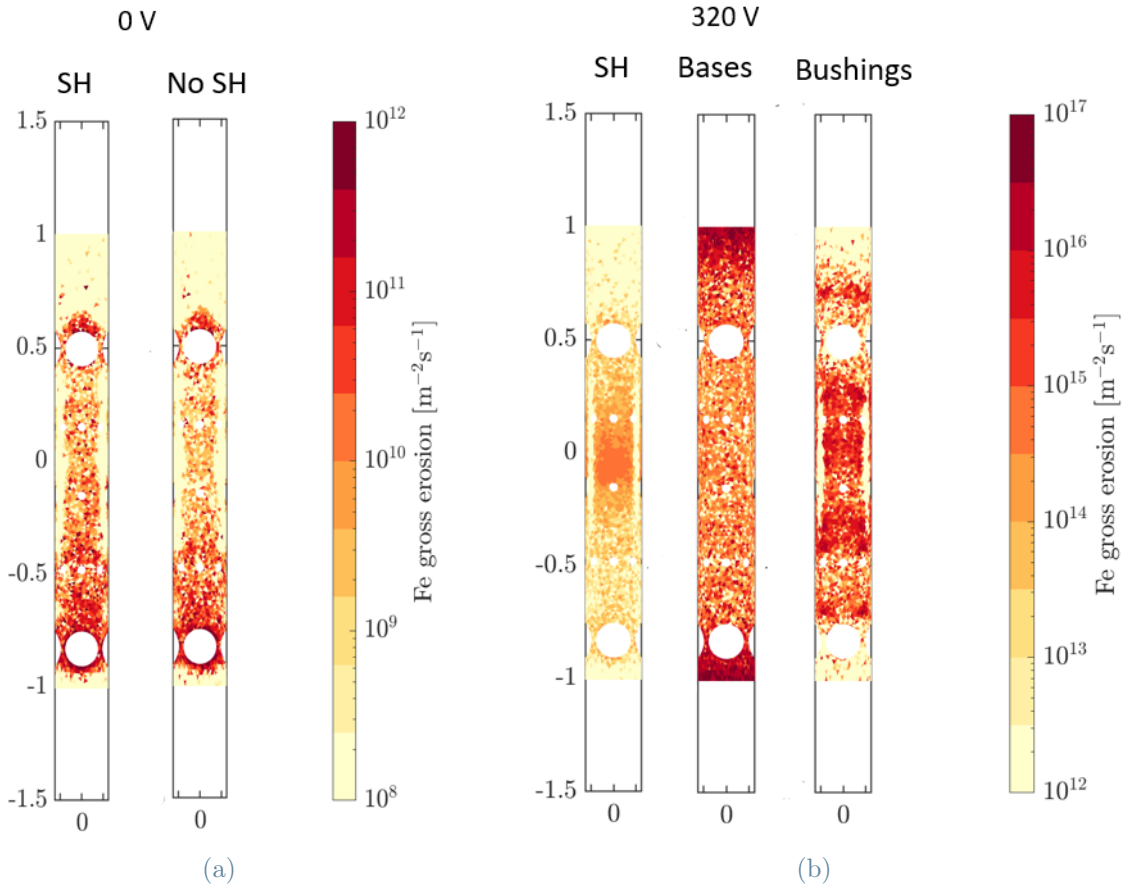

Figure 4.3: Erosion distribution on the lateral wall at 0 V (a) and 320 V (b).

Figure 4.2 shows the contribution to lateral wall erosion by each impurity species for the simulations where SH is present. As already mentioned, at 0 V only Fe/Cu impurities are produced, thus erosion is entirely caused by them. At 50 V the Mo sputtering threshold is overcome, thus erosion by Mo is introduced and its share increases as the bias is

raised, eventually becoming the dominant one. W erosion appears at 100 V, although its contribution to the erosion is less relevant than Mo. Similar behaviour is found for the Fe and Cu wall, although, since the initial Fe source is less strong than the Cu one, its contribution to the lateral wall erosion is overcome faster by the Mo component.
The erosion data reported in figure 4.1 refer to an averaged value over the whole lateral wall surface. However, since the surface is very large, it may be interesting to observe how the erosion is distributed on it. Figure 4.3 reports it, showing the data for 0 V and 320 V simulations with Fe wall, although equivalent results are obtained with Cu wall. At 0 V the SH and non-SH scenarios are distinguished. It is observed a very similar distribution for the two cases, although in the SH scenario a slight erosion enhancement in the central region, where the SH is located, can be noted. At 320 V the erosion distribution is heavily dependent on which PFC is biased. In general, it is observed that the erosion predictably intensifies in the proximity of the biased component, as that is where the impurity source is increasing with the bias. Thus, for the SH case erosion peaks in the middle region, for the bases case it peaks at the ends, while for the bushings case many small peaks arise near each bushing.

4.1.2. Realistic steel wall

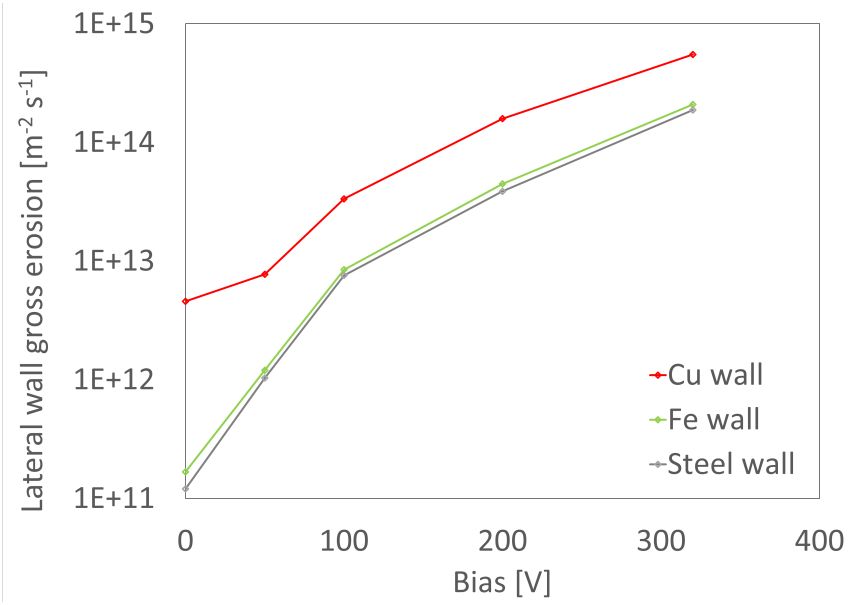

Figure 4.4: Lateral wall erosion as a function of the bias applied to the SH for a realistic steel wall, compared to the simplified Fe/Cu wall models.

A further step in the description can be made by replacing the simplified Fe/Cu wall model with a realistic, multi-element, steel wall. The stainless steel of the GyM chamber

is the AISI 304L, a steel in which the main components, other than Fe, are Cr and Ni, with an average concentration of about 18% and 9% respectively. New simulations are performed at the same biases as the previous ones and the lateral wall erosion is compared with the Fe/Cu wall one in the SH scenario, results are shown in figure 4.4. As evidenced by the plot, the realistic steel wall is well described by a full Fe wall approximation, providing similar results, especially at the higher biases. Fe wall consistently overestimates the erosion with respect to the steel wall, in a range between 10-40%, with the maximum gap being observed with no bias applied. Cu, on the other hand, proves to not be a good predictor for the alloying elements of this steel, yielding a much higher erosion.
These results can be well explained by looking at the sputtering yields of the involved elements, reported in figure 4.5. Figure 4.5(a) shows the energy dependence of the sputtering yields of plasma He ions striking the steel wall at normal incidence. It can be seen that Fe and Ni share very similar values, at low energies the Fe curve slightly exceeds the Ni one, while above ∼180 eV the opposite is observed. Cr instead shows a significantly lower sputtering yield at all energies. The Cu curve is also reported, evidencing a clearly higher yield, coherently with the much higher erosion observed in the results.
Equivalent comments can be made about the energy dependence of eroded impurities sputtering the steel elements, so figure 4.5(b-d) show the angular dependence instead, at a fixed energy impact energy of 20 eV, which is the mean impact energy of impurities on the lateral wall. Figure 4.5(b) and (c) show the curves for Mo and W projectiles respectively. Cr is again observed to carry the lowest yields, while Fe and Ni behave similarly, although a gap forms towards grazing incidence, where Fe exceeds Ni. Figure 4.5(d) instead shows the nine combinations of the steel elements impacting on themselves. Notably, three groups of curves can be distinguished, each characterized by sharing the same target element. This is due to the fact that, for the projectile, the mass is the main parameter influencing the sputtering process, which is similar for Fe, Ni and Cr, whereas for the target also the binding energy in the material plays a role. Hence, changing the target element leads to greater differences in the sputtering yield than changing the projectile element, leading to the behaviour reported in figure 4.5(d). Anyway, even in this case Cr is the steel element with the lowest sputtering yield.
Overall, it can be concluded that the difference observed between the steel wall and the simple Fe wall cases can be mainly attributed to the presence of Cr, whose lower sputtering yield causes the Fe wall to overestimate the erosion relatively to the steel one, whereas Ni behaves very similarly to Fe and should be expected to influence the results to a lesser extent. Nonetheless, the gap is limited to a 40% increase in the full Fe case at worst, making this assumption an acceptable approximation of the steel wall.

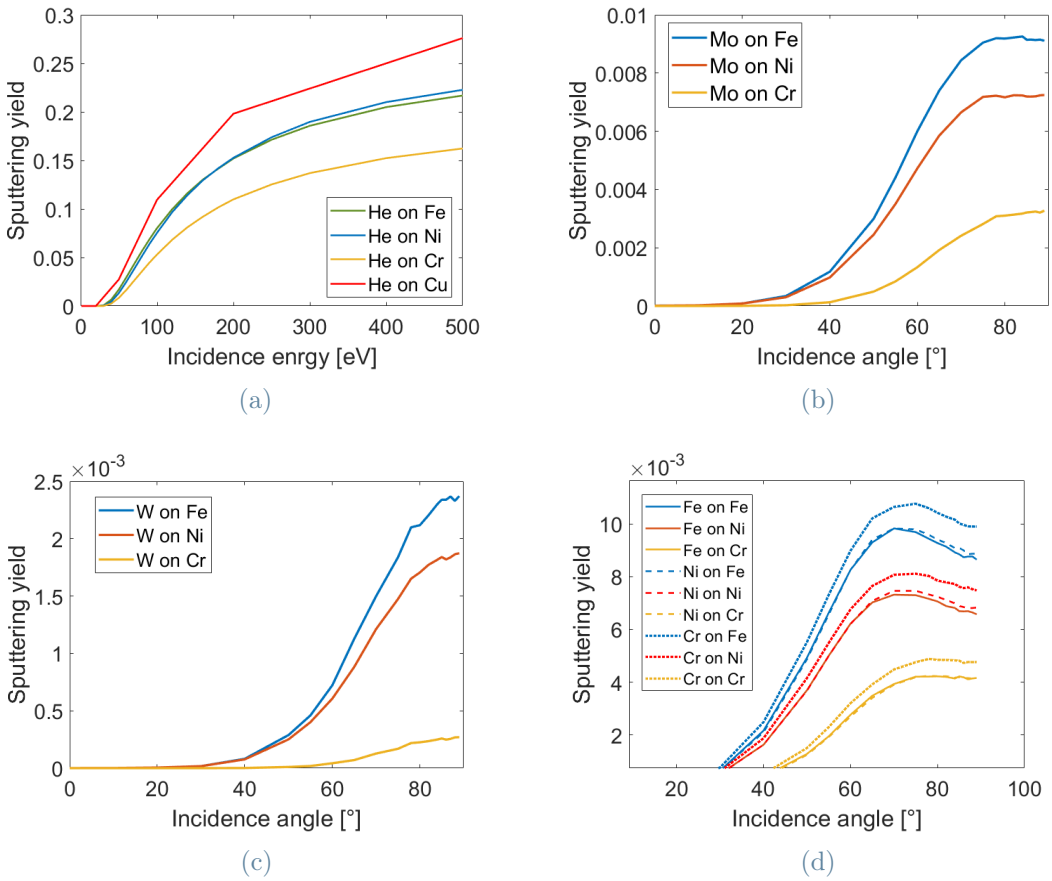

Figure 4.5: Sputtering yields of the plasma and impurity ions on the steel wall atomic species.

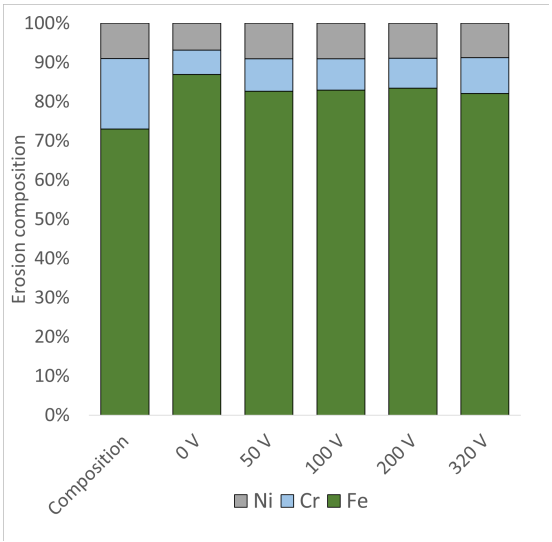

Figure 4.6: Composition of the eroded flux from the steel lateral wall at each bias, compared to the elemental composition of the steel

These considerations are confirmed by looking at the erosion results of each wall component, as reported in figure 4.6. The first column represents the wall composition, while the other column show the composition of the eroded flux at each bias. It can be easily seen that Fe holds a larger erosion share than its weight in the wall compostition, while the opposite is observed for Cr, meaning that the erosion decrease compared to the full Fe wall can be attributed mostly to Cr indeed.

4.1.3. Evolution in multiple time-steps simulations

The work carried out up to now concerns simulations performed in a single time step. This means that, since the lateral wall is never eroded directly by the background plasma, test particles are never launched from it. However, we have seen that most eroded impurities end up striking the lateral wall, causing further erosion, therefore it is of interest to evaluate the evolution of the system at the following time steps, as test particles are launched from the lateral wall as well. Thus, it will be done in this subsection.
The multi-steps simulation performed here are setup to calculate the erosion due to the background plasma only in the first step, while it is switched off in the following ones, in which, therefore, the new test particles are launched according only to the erosion caused by impurities traced in the previous step. This allows to observe the evolution of multiple generations of impurities, which can all be linked to the first instance of erosion by the plasma. Hence, the cumulative erosion on the lateral wall is computed by summing the contributions of each step, and it is compared with the erosion of the single step simulations. Results are shown in figure 4.7 and 4.8. From figure 4.8 it is evident that the total erosion decays at the following time steps, as the amount of impurities produced in each generation is lower than the preceding one by a couple order of magnitude, somewhat coherently with the sputtering yields, which are in the order of few percent at maximum. The consequence is that only the very first steps contribute to the cumulative erosion, while the following ones end up being negligible. In fact, as shown in figure 4.7, more than 90% of the cumulative erosion is due to the first step, which is the same erosion computed in the single time step simulations. The correction thus is limited to a 3-10% range, slightly increasing with the bias, and it is entirely due to the second time step, whereas the following ones provide negligible contributions.

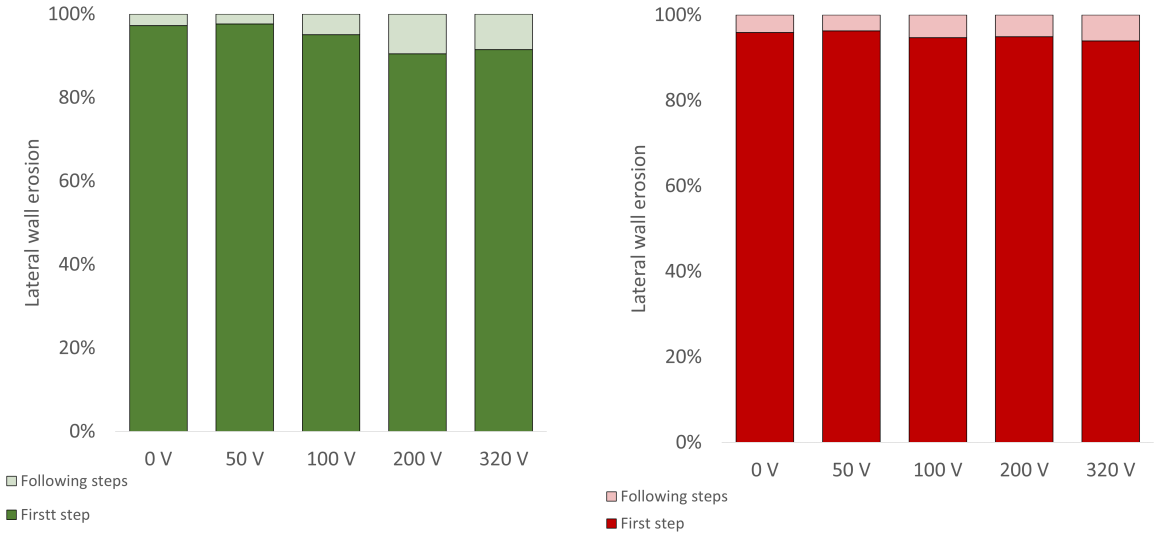

(a) (b)

Figure 4.7: Contribution to the cumulative lateral wall erosion of the first step compared to the following ones, at each bias for Fe (a) and Cu (b) walls

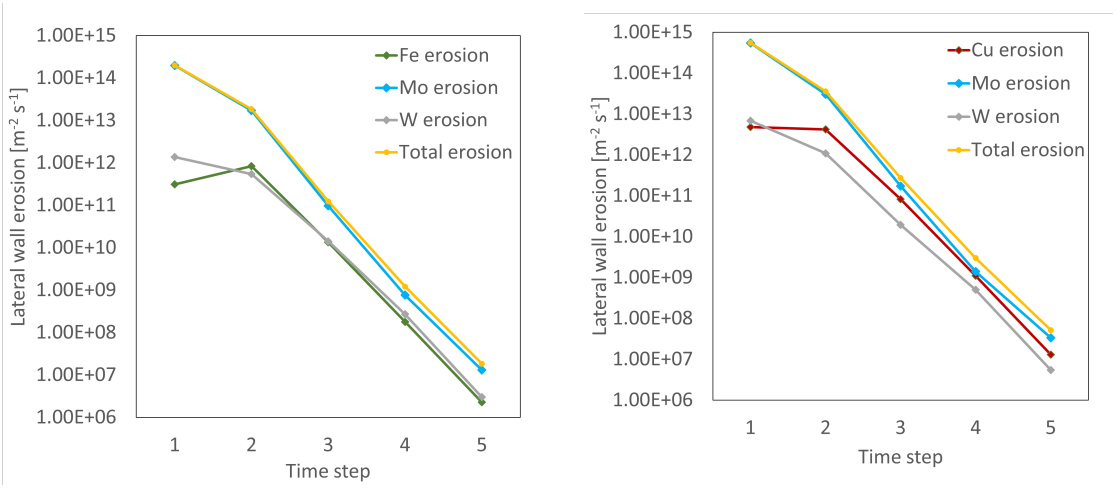

(a) (b)

Figure 4.8: Lateral wall erosion at each time step for each traced impurity, for Fe (a) and Cu (b) wall at 320 V

Further comments can be made by observing the erosion at each step, separating the contribution of different impurities. It is seen that, while the erosion due to Mo and W steadily decays, Fe/Cu one stays constant, or even slightly increases, between the first and second step, and then declines with the same rate of other impurities. This is attributable

to the aforementioned behaviour of the lateral wall. In fact, at the second time step, the lateral wall acts as an additional Fe/Cu impurity source, which was not present at the previous step, thus balancing, or even overcoming, the natural decay of impurity content for Fe/Cu.

The spatial distribution of the erosion can also evaluated through the following time steps. Figure 4.9 shows the erosion distribution on the lateral wall in the first three time steps for the 320 V case. Due to the decreasing trend of the erosion, the represented scales are different at each time step. However, the pattern can be compared, and it is observed that, while in the first one the erosion is focused near the SH region, in the following ones it tends to be more uniformly distributed on the lateral wall.

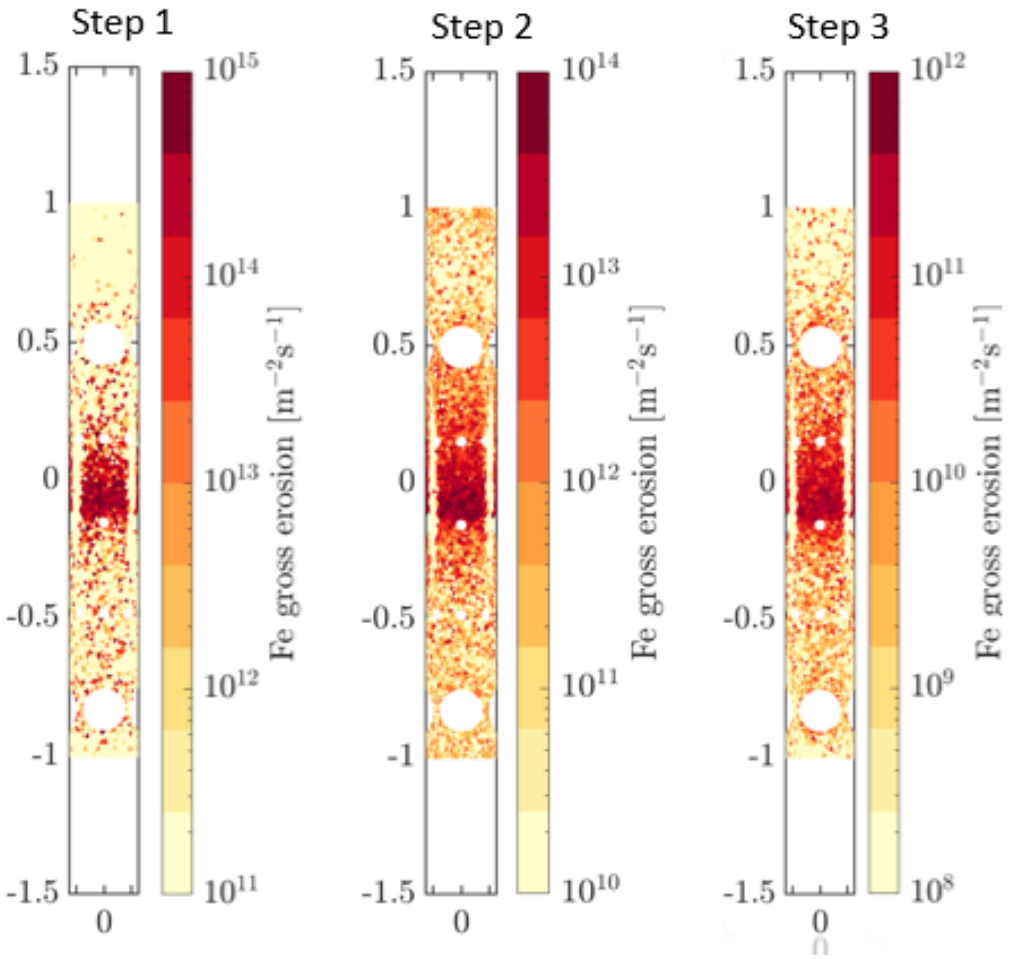

Figure 4.9: Erosion distribution on the lateral wall at different time steps

4.2. Global erosion results on samples

The samples are the plasma facing component actually investigated in experimental campaigns, therefore it is useful to model them in ERO2.0 simulations. We have seen that they can be simulated at a local level, where the surface morphology of specific samples is examinated. Instead, here they are studied at a global level, where they are modelled as generic W surface, thus not taking into account the peculiar characteristics of each sample, but on the other hand allowing to observe their behaviour in the complete GyM environment.
The results reported in figure 4.10 are retrieved from the same simulations of sections 4.1.1 and 4.1.2, thus investigating Fe, Cu and realistic steel walls, at the different biases applied to the Mo mask and the samples.

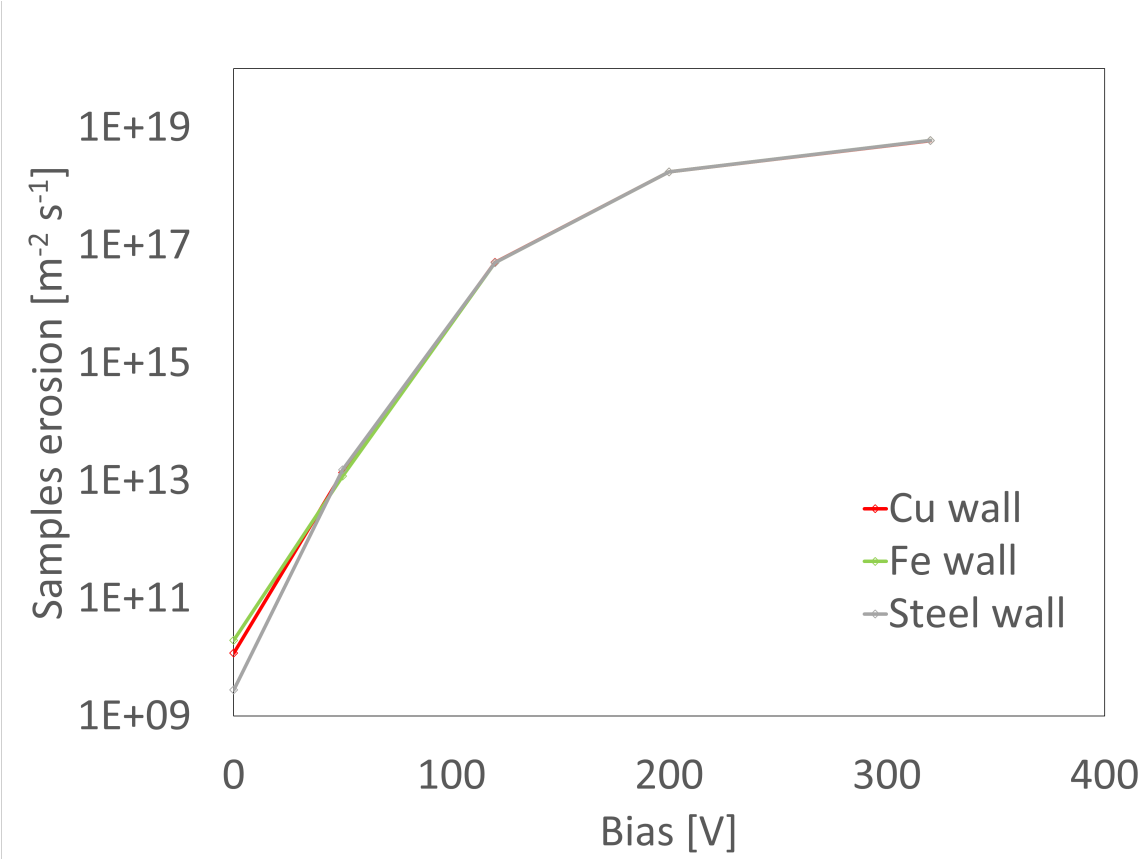

Figure 4.10: Gross erosion on samples at different biases and wall materials

Differently from the lateral wall results, here the bias is directly applied to the examined component. Moreover, the samples can be directly sputtered by the background plasma, unlike the lateral wall. The results show some difference for the different wall materials

at 0 V, but it vanishes at the higher biases. In fact, at 50 V, Mo impurities start to be sputtered from the Mo mask, and being in close proximity to the samples they easily become the dominant source of erosion, regardless of the material of the surrounding walls. Above 100 V the surrounding material becomes even more irrelevant, as the samples start being directly sputtered by the plasma, hence the erosion is dominated by He ions, as reported in figure 4.11.

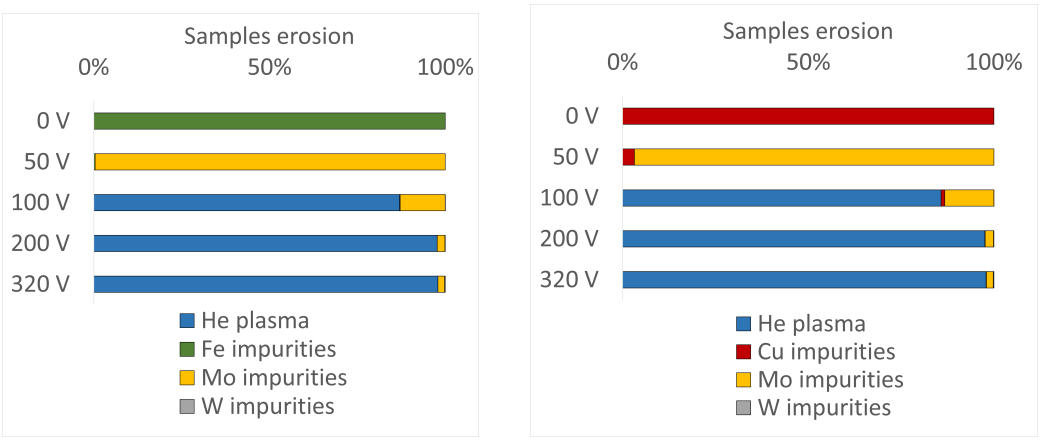

Figure 4.11: Contribution to the samples erosion by each ion species, in Fe wall (a) and Cu wall (b)

4.3. Global deposition results

The study of deposition patterns inside GyM allow to gain insight about the migration process of eroded impurities in the device. Results from [102] and [113] have shown how most eroded impurities end up hitting the lateral wall and depositing there, coherently with the fact that the lateral wall is by far the largest PFC in terms of surface and that the long and thin shape of the vacuum chamber cylinder favors the deposition on the sides.

Figure 3.9(c) showed the deposition distribution for each impurity species at varying bias applied to the SH. Fe/Cu deposition did not show a dependence on the bias, as it is applied to Mo and W materials. However, differently from Mo and W, Fe/Cu are eroded from multiple sources, namely the bases, the bushings and the SH support, thus it may be interesting to examine the deposition patterns separating the effect of each source. To do this, three simulations were considered:

- Test particles launching from all three Fe/Cu sources.

- Test particles launching from bases and bushings (disabled launch from SH support).
- Test particles launching only from the bases.

All of them are performed at 0 V, as results should be the same regardless of the applied bias. The contribution of each source can be retrieved working by subtraction between the results of these simulations.

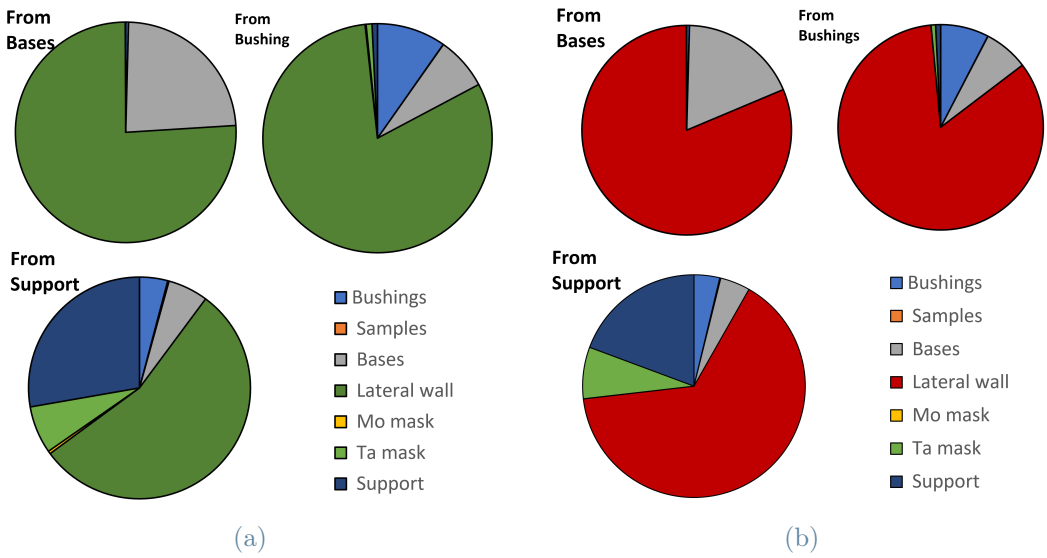

Figure 4.12: Deposition location of Fe (a) and Cu (b) particles launched from each of the three Fe/Cu sources

Figure 4.12 reports the resulting deposition distribution, separated by source, for Fe and Cu walls. As stated before, most impurities deposit on the lateral wall for all the sources, however some differences are observed for the three sources. Particles launched from the bases basically only have the bases themselves as a landing spot, other than the lateral wall, as the fraction of deposition on the bushings and the SH is very little. Particles launching from the bushings, instead, deposit roughly in equal amounts on the bushings and on the bases. The deposition fraction on the SH is still very low, but higher than the bases case, as some of them are nearer to the SH, about 1% of particles deposits both on the support and on the Ta mask. Particles launched from the support show the lowest probability of depositing on the lateral wall, only 54% of them do it compared to more than 75% in the previous two cases, considering Fe wall. A good portion of the remaining particles re-deposits on the support, while similar amounts of few % distribute on the bushings, bases and Ta mask, while also a 1% fraction is observed to deposit on the Mo mask. Due to their tiny surface, the deposition fraction on the samples is always

negligible relatively to other components. Differences are also observed for Fe and Cu walls, although the overall pattern is the same; in particular, in the Fe case each source sees a larger re-deposition fraction and a lower component of particles escaping to the lateral wall. This is coherent with figure 3.9(c), where Fe showed a lower overall deposited fraction on the lateral wall.
Further development in the study of the influence of each Fe/Cu source on the deposition patterns was made by shifting the focus to the target PFCs and examining the deposited particles by their original source. In particular, the SH components were investigated, and figure 4.13 shows for each of them the fraction of deposited particles launched from the bases, the bushings or the SH support. The same simulations previously presented were used to retrieve these data.

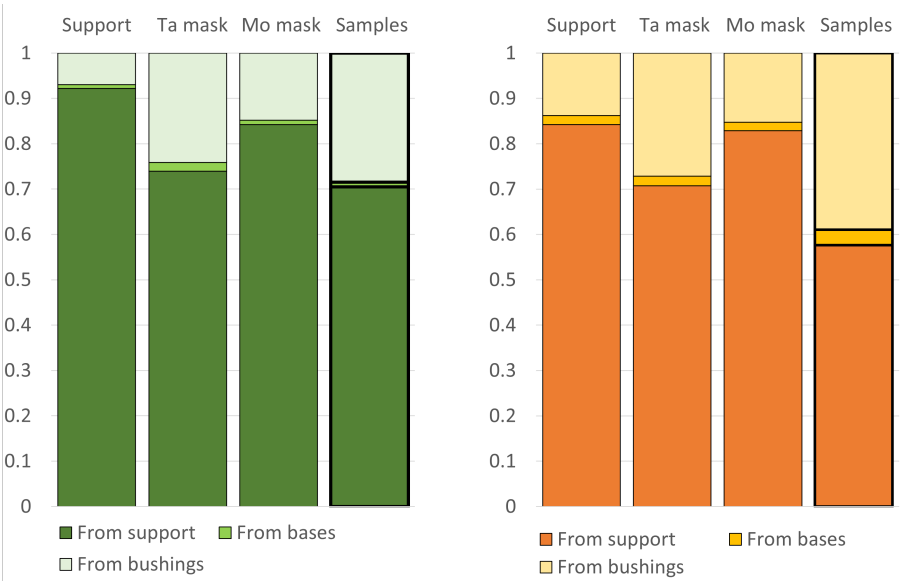

Figure 4.13: Deposition on each SH component subdivided by the share of particles coming from each Fe (a) and Cu (b) source.

A general comment is that the fraction originated from the bases is always tiny, never exceeding 3%, coherently with figure 4.12 showing that particles eroded from the bases usually only re-deposit on the bases or reach the lateral wall. The most relevant deposition source is the support for all components, being the nearest one, and it is obviously particularly true for the support itself, as particles re-deposit on it. The behaviour of Ta mask, Mo mask and samples can be explained by observing the geometry of the sample-holder, recalling figure 3.7(b) and looking at figure 4.14 where front and rear views of the

SH, highlighting the four components in different colors, are reported. The Mo mask and the samples face the same flux of impurities coming from the bushings and the support at the front side of the SH. However, particles eroded from the support can enter a region enclosed between the Ta mask and the back of the support, where they can deposit on the sides of the Mo mask, thus raising the share of deposition originated from the support, also thanks to the fact that the lower reflection coefficient of Mo with respect to W will favour deposition on the Mo mask instead of the internal wall of the Ta mask. The Ta mask on the other hand faces a higher flux of impurities coming from the bushings, as it shields the Mo mask from it on the sides, hence the share of deposited bushings impurities is higher than the Mo mask.

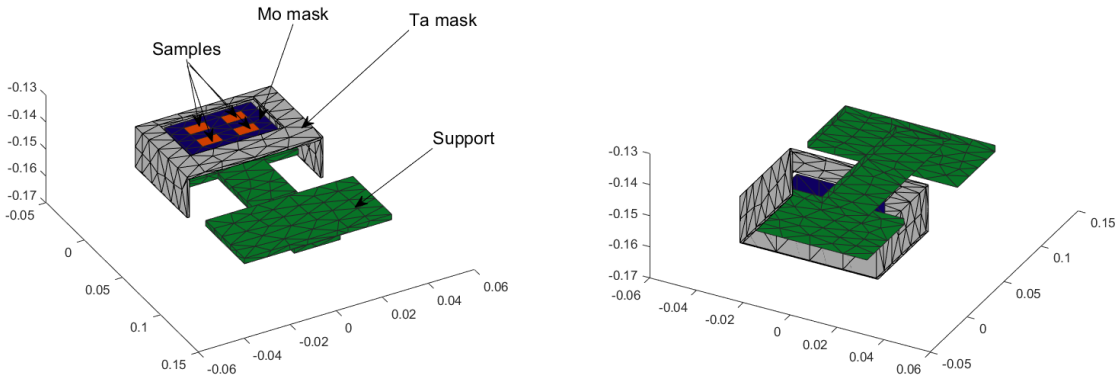

(a) (b)

Figure 4.14: Front (a) and rear (b) view of the four sample-holder components.

A focus on the samples is then presented at the higher biases, where Mo and W sources become active, presented in figure 4.15. Predictably, as soon as Mo starts being eroded it becomes the dominant source of deposition on the samples, as they are embedded in the Mo mask. Also the W component increases its importance at the highest bias, as the gross erosion of the samples increases, and so does the prompt re-deposition effect.

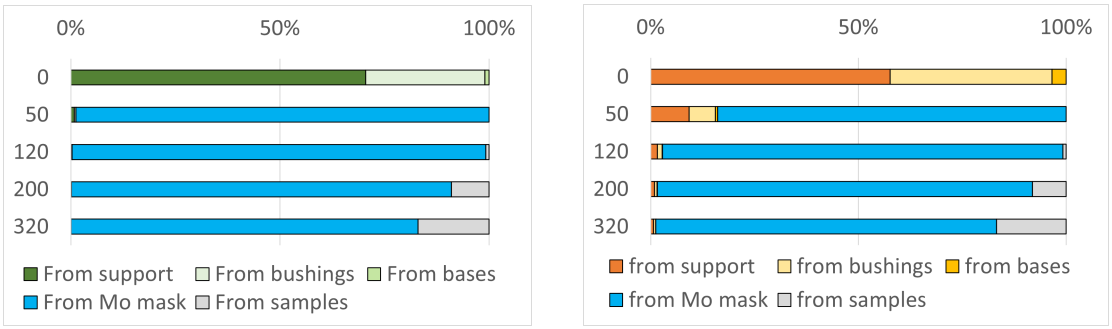

(a) (b)

Figure 4.15: Deposition on samples at varying bias, subdivided by the share of impurities coming from each source.

4.4. Local erosion results on W samples

This section will present the results of simulations conducted at the microscale level, similarly to the ones presented in section 3.2. Differently from global simulations, here the erosion and migration is simulated only in a tiny volume near the surface of the W samples located in the sample-holder. Therefore, they do not treat self-consistently the impurity content in the plasma, taking into account erosion from all the PFCs of the machine. On the other hand, the small scale of the simulation allows to describe the surface morphology of different samples and observe its effect on the erosion process, instead of considering them as generic flat W surfaces like in the global simulations. The morphologies of surfaces employed in the simulations can be reconstructed from measurements on real samples with techniques such as atomic force microscopy (AFM), hence allowing to establish a link between ERO2.0 simulations and actual experimental campaigns of samples exposure to the GyM plasma. This is the main goal of this section, delivering the results of erosion simulations on a set of samples surfaces and comparing them to experimentally measured erosion on said samples, particularly comparing the simulated $Y_{eff,ERO}$, calculated as explained in section 3.2, to the experimental $Y_{eff,\Delta m}$, measured by mass loss of the samples during the exposure.
A total of five W samples will be investigated in the present section, four of them are made by W or W+O coatings deposited on polished Mo substrates and were employed together in an experimental campaign in 2023:

- W_{HiPIMS}: a W film of 1 μm thickness deposited through the High Power Impulse Magnetron Sputtering (HiPIMS).
- $W{+}O_{PLD}$: a W film with 15% of atomic concentration of O, 1 μm thickness, de-

posited by Pulsed Laser Deposition (PLD).

- W_{CMSII}: a W film of 5.1 μm thickness, deposited by Combined Magnetron Sputtering and Ion Implantation (CMSII).
- $W{+}O_{HiPIMS}$: a W film with 3% O concentration, 4 μm, deposited again by HiPIMS.

A fifth one is instead made of full W bulk, originally employed in a previous experimental campaign, and is useful as a reference to compare with the coatings. Figure 4.16 shows the AFM images of the surfaces of the five samples, which are replicated in ERO2.0 to perform the simulations.

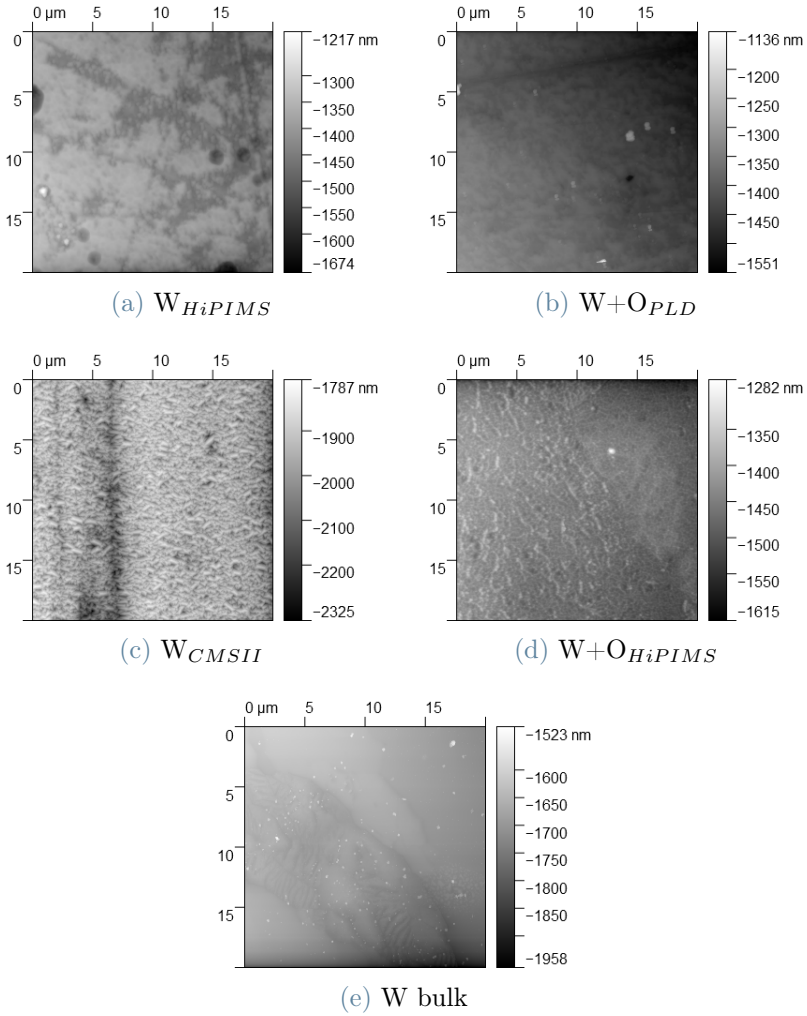

(a) W_{HiPIMS} (b) $W{+}O_{PLD}$

(c) W_{CMSII} (d) $W{+}O_{HiPIMS}$

(e) W bulk

Figure 4.16: AFM images of the surfaces of the five samples employed in the micro scale ERO2.0 simulations

Both the experimental and the simulated Y_{eff} are thus calculated for the samples at vary-

ing bias applied to them, to tune the impact energy of He plasma ions on the surface, and observe its influence on the erosion. Figure 4.17 reports the results of such calculation, plotting Y_{eff} against the impact energy, which is determined by adding the absolute value of the applied bias to the unbiased potential drop in the plasma sheath. It is important to specify that the W+O samples are simulated as pure W surfaces, therefore taking into account only the effects of their surface morphology, but not their elemental composition, which may be included in future developments. The simulated $Y_{eff,ERO}$ can be seen to follow quite closely the nominal sputtering yield curve at normal incidence obtained from SDTrimSP, the only difference being due to the fraction of test particles leaving the simulation domain perpendicularly to the surface: as this fraction approaches 1, $Y_{eff,ERO}$ will result closer to the nominal sputtering yield. For most samples the fraction of particles leaving the boundary is above 90%, except for the 72% value of the W_{CMSII} sample, which also appears as the roughest one, hence being the farthest from the nominal curve. Nonetheless, the biggest difference is observed between the simulated $Y_{eff,ERO}$ and the experimental $Y_{eff,\Delta m}$, with the latters in general being lower by about an order of magnitude, regardless of the specific sample considered. This means that other phenomena are occurring to cause this gap, which is not explainable by the morphology alone, or the elemental composition, since it is observed for all the samples.

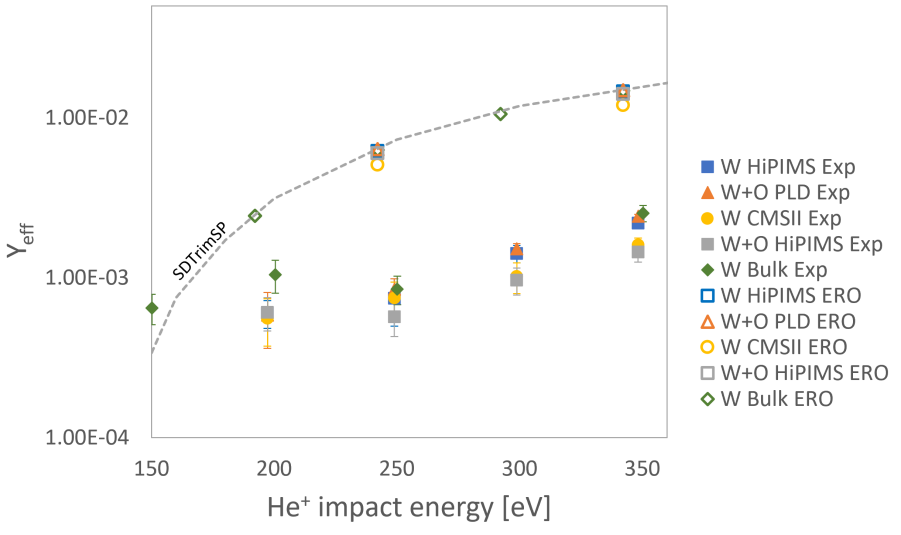

Figure 4.17: Values of the effective sputtering yield (Y_{eff}) calculated from ERO2.0 simulations and measured by mass-loss in experiments, for the five samples considered, as a function of the He impact energy. Overall similar values are observed for different samples, while a significant gap is observed between simulations and experiments. The SDTrimSP sputtering yield curve for He on W at normal incidence is also reported for reference.

One possible explanation is represented by the dynamic retention of He in the W surface. The presence of He may cause the W to be partially shielded from other He ions striking the surface, thus lowering the overall sputtering yield. For this reason, SDTrimSP was used to calculate a new sputtering yield curve for W with a 50% concentration of He. New simulations were performed on the W bulk sample using these new data, obtaining a significantly lower value of $Y_{eff,ERO}$, much closer to the experimental ones, as depicted in figure 4.18.

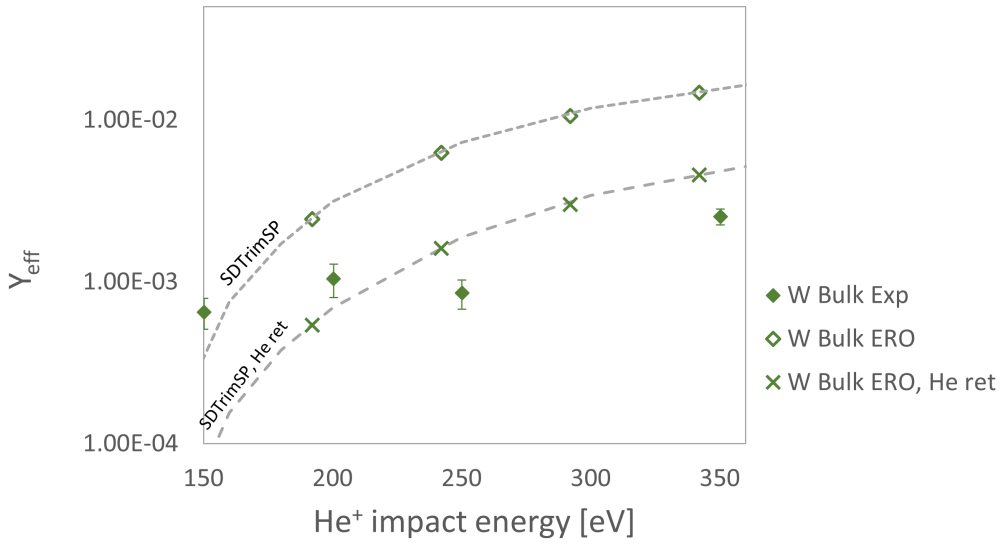

Figure 4.18: Experimental and simulated Y_{eff} for the W bulk sample, including simulations performed using the modified sputtering yield that considers He retention.

5 | He plasma erosion simulations in ASDEX Upgrade

This chapter will present the results of ERO2.0 simulations performed at a global level in the environment of the ASDEX Upgrade tokamak. As introduced in section 3.3, the main open issue was about finding a good agreement between the eroded thickness on the outer divertor experimentally measured during the exposure to the 2019 L-mode discharge, and the one retrieved from the ERO2.0 simulations, performed using a background plasma produced by SOLPS-ITER, aimed at reproducing the plasma conditions observed in that experimental campaign. Initial results presented in section 3.3 proved to be very far from experimental measure, underestimating the eroded thickness by orders of magnitude, hence highlighting the need to find different ways to setup the simulations in order to improve the agreement.
This will be done particularly in section 5.1 and its relative subsections, where a scan of some parameters, namely the electron temperature, the ion temperature and the impurity content, will be performed to observe their effect on the erosion of the outer divertor. Section 5.2 will investigate the behaviour of the obtained erosion profiles at the following time steps, allowing to produce a more accurate description of the steady state erosion regime. Section 5.3 instead will focus on extending the model by including the description of a variable distribution of effective mass and charge for the plasma in the simulated volume, allowing a more accurate description of the two species of He ions.

5.1. Parametric analysis for improvements in experimental agreement

This section will be devoted to investigate some relevant plasma parameters whose variation with respect to the base case could explain, at least partially, the large gap observed between the measured net erosion on the outer divertor during exposure to the # 36687 L-mode discharge (50 nm) and the one resulting from ERO2.0 simulations. Section 5.1.1 will provide a parametric scan of the electron temperature (Te), by applying a variable

coefficient that multiplies the original Te profile provided by SOLPS-ITER. The same will be done in section 5.1.2 for the ion temperature (Ti). Section 5.1.3 instead will consider the possible presence of extrinsic impurities in the plasma that could enhance the erosion, in particular oxygen will be investigated, and a scan will be performed over its concentration to observe the effect on the erosion. Finally, section 5.1.4 will examine some cases in which these parameters are applied simultaneously, to observe their combined effect.

5.1.1. Electron temperature coefficient

The electron temperature is a plasma parameter that is able to influence the erosion process. In fact, recalling equation 1.39, we can observe that the expression for the mean impact energy of ions contains a term linearly dependent on Te, which is the energy gain across the sheath. Thus, by raising Te, the impact energy is also raised, and in turn the sputtering yield usually increases, leading to an enhancement of the erosion process.

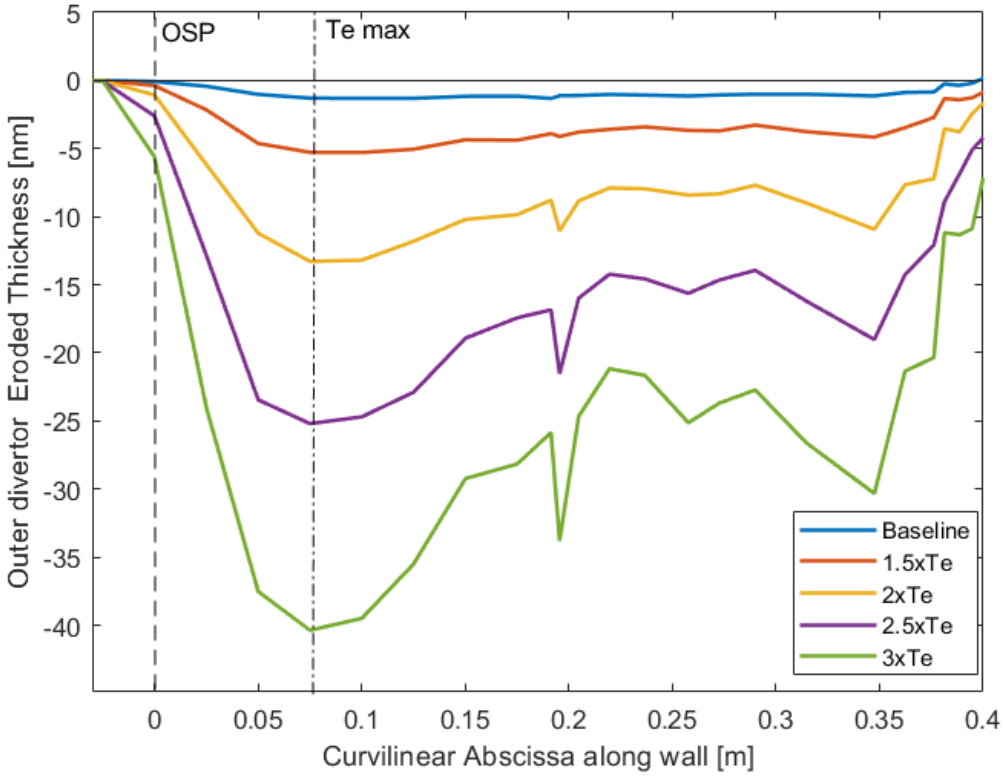

Figure 5.1: 1D net erosion profiles along the outer divertor, considering different Te obtained by multiplying the original SOLPS-ITER Te profile by a coefficient. The location of the maximum value of the Te is marked for reference.

The SOLPS-ITER profile for the Te was obtained by matching the experimental data at the outer strike point, as they were both reported in figure 3.13. It can be seen that, although the SOLPS profile overestimates the median values of the experimental data, there is however a large uncertainty, as many data points reach values that are two or even three times larger than the employed SOLPS profile. For this reason, multiplying the original SOLPS profile by a fixed coefficient constitutes a rough, but simple way to address the possibility of the plasma experiencing higher Te, observing the effect on the erosion simulated eroded thickness on the outer divertor.
Figure 5.1 shows the erosion profiles obtained from simulations where the Te profile was multiplied by coefficients in the 1.5-3 range, compared to the base case. Overall we can note that the erosion is strongly influenced by varying Te, as it increase up to a factor $\sim$30 in the most extreme case with respect to the baseline, reaching values comparable with the reference measured eroded thickness of 50 nm. It can also be seen that the erosion profile modifies its shape at increasing Te coefficient. In particular, it can be seen that at higher coefficients a net erosion peak becomes increasingly evident compared to the flatter profile of the base case, and its location coincides with the one of the maximum Te.

5.1.2. Ion temperature coefficient

Similarly to the Te, the ion temperature is also a plasma parameter able to influence the erosion process. Recalling again equation 1.39, we can see that the mean ion impact energy depends on a term containing Ti, again linearly dependent as in the Te case, which express the mean energy of ions before crossing the sheath. Therefore, raising Ti will again lead to an enhancement of the erosion process.
Unlike Te, the original SOLPS-ITER profile of the Ti was not obtained by benchmarking it with experimental data, but was instead purely an outcome of the SOLPS simulations. This leads to uncertainties, mainly due to the fact that the determination of the Ti profile is not univocal in SOLPS. Therefore, the same procedure done for Te is repeated here for Ti, applying multiplicative coefficients to the original Ti profile to observe the effect of a higher Ti on the erosion. The range of investigated coefficients is again 1.5-3. Figure 5.2 shows the net erosion results of such simulations. Even in this case the overall effect is an increase of the erosion across the whole profile, however it can be immediately noticed that the enhancement is weaker with respect to the Te case, as the highest Ti coefficient yields an erosion three times lower than the analogous highest Te coefficient. Furthermore, Ti coefficients have a different influence on the shape of the erosion profile, and this can be attributed to the different Ti profile with respect to Te. In fact, recalling figure 3.13,

it can be seen that Ti increases farther from the strike point and reaches a maximum around 0.3 m from it in the curvilinear abcissa along the divertor, whereas Te increases more rapidly, peaking around 0.075 m, than decreasing moving away from the OSP. For this reason the erosion profile tends to increase more around the peak of Ti at increasing Ti coefficient.

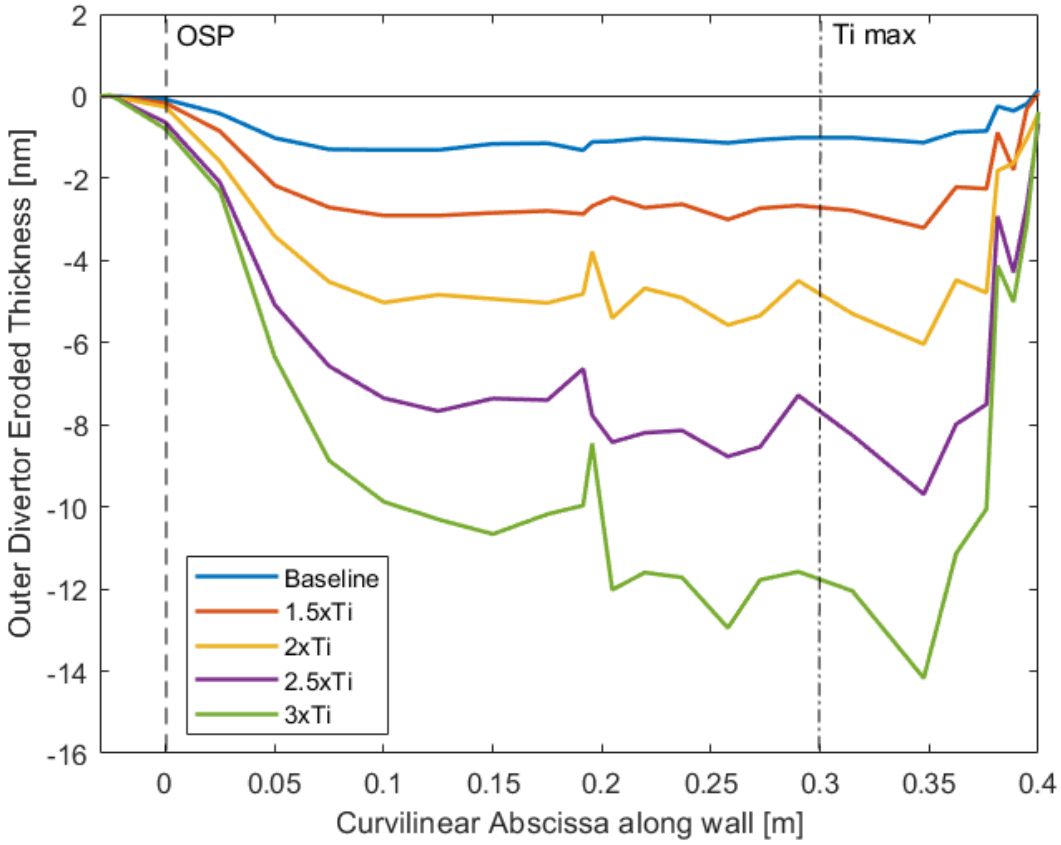

Figure 5.2: 1D net erosion profiles along the outer divertor, considering different Ti obtained by multiplying the original SOLPS-ITER Ti profile by a coefficient. The location of the maximum value of the Ti is marked for reference.

5.1.3. Oxygen impurity concentration

Another possible factor influencing the erosion of the outer divertor may be the presence of foreign impurities in the plasma. On one hand, impurities, which are usually heavier than the plasma He ions, can sputter the W more effectively from the wall, as the energy transfer between the projectile and the target is more efficient if the mass difference between the two is reduced, hence the sputtering yields will be higher. On the other hand, impurities can also reach higher ionization states, which in turn means a higher

energy gain across the plasma sheath. Therefore, the ion impact energy will be higher for the impurities, which means moving higher on the sputtering yield curve if we are on the increasing side of the curve with respect to energy, which is usually the case. Hence, the overall effect of introducing an impurity species may be a great enhancement of the erosion, even if the concentration of said impurity is small.

To study this effect, oxygen (O) was chosen as a proxy for light impurities, as it is a typical element that may be present in the plasma along with boron (B), and it was preferred over the latter as its greater mass and atomic number should lead to a greater enhancement of the erosion. Thus, a parametric scan was performed over a very wide range of oxygen concentrations, between a very small one (0.1%) and an extremely high one (10%). It should be noted that all simulations are performed considering the original He background plasma, thus assuming that the plasma parameters are not influenced by the presence of impurities, which obviously is a more accurate assumption when the impurity content is lower.

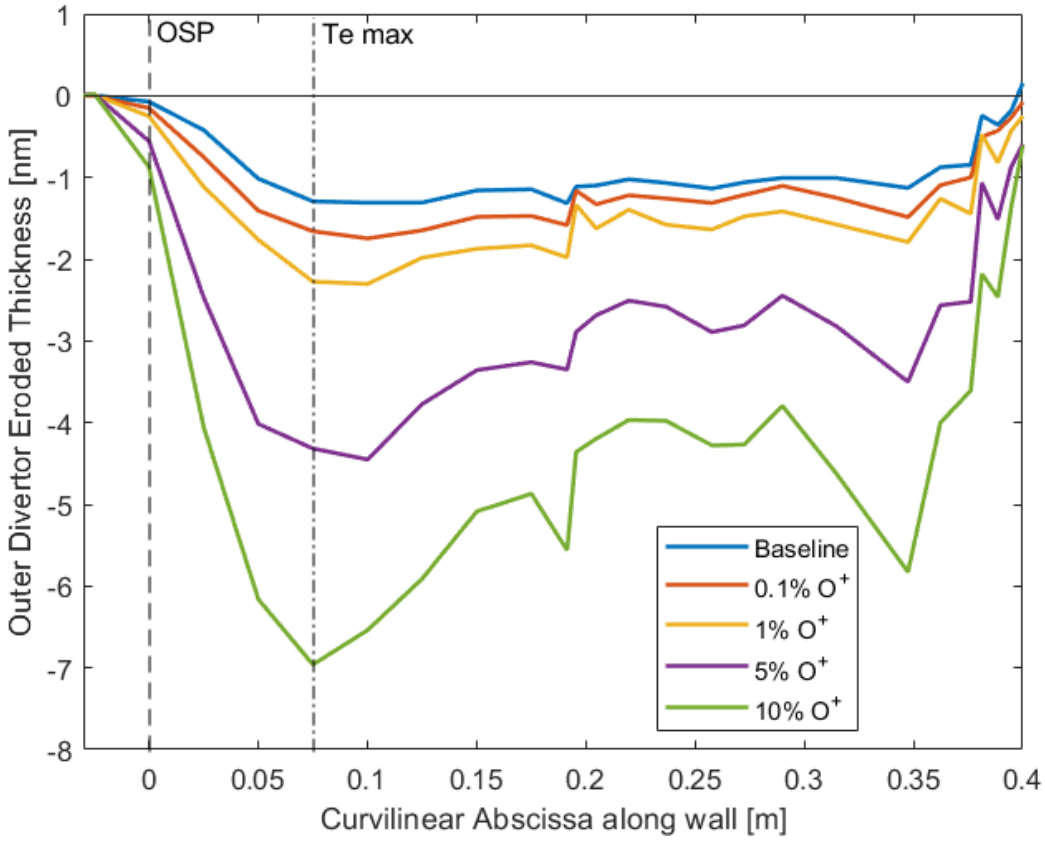

Figure 5.3: 1D net erosion profiles along the outer divertor, considering a variable oxygen impurities content in the low charge state O^+.

O can exist in different charge states, up to O^{8+} when fully ionized, which have different influence on the erosion. To account for this, the parametric scan on the concentration is repeated for two different fixed charge state: a low charge state considering singly ionized O, hence O^{+}, and a high charge state, which has been selected to be O^{6+}, basing on a study conducted at WEST [118], showing that in general O finds itself in higher charge states at the outer divertor, and O^{6+} can be viewed as a reasonable mean value.
Figure 5.3 shows the profiles resulting from the simulations in the low charge state scenario. It can be seen that in this case the erosion enhancement is mild, roughly doubling at 1% O^{+} concentration but still being very far from the target experimental value. At the higher concentrations the erosion increases more significantly, however even in the extreme case of 10% concentration there is a difference of one order of magnitude with respect to the experimental erosion. The erosion increases more or less uniformly, however, especially at the highest concentration, a net erosion peak starts to form in the region of maximum Te, similarly to what happened when applying Te coefficients. This aspect will be more evident in the high charge state scenario.

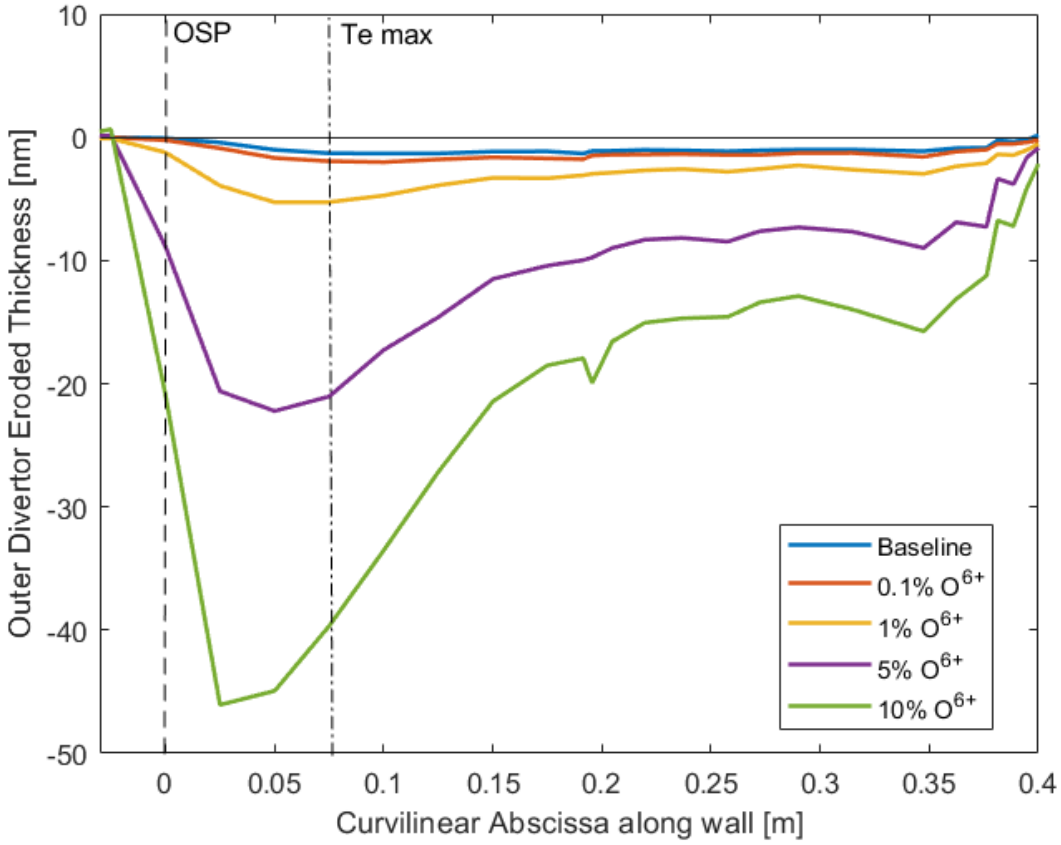

Figure 5.4: 1D net erosion profiles along the outer divertor, considering a variable oxygen impurities content in the high charge state O^{6+}.

Figure 5.4 shows the same scan performed for the high charge state O^{6+}. It is immediately evident that the effect on erosion is much greater than the low charge state case, especially in the region of maximum Te, where a very sharp erosion peak arises, reaching values comparable to the experimental measure. This behaviour may be explained by the fact that, recalling again equation 1.39, the sheath potential drop term in the mean impact energy expression, which is proportional to Te, is also proportional to the charge state of the ions. Therefore, introducing higher charge state impurities, will increase its strength, and will do so particularly in higher Te regions, giving the resulting profile. Figure 5.5 shows the share of gross erosion attributable either to the He or the O ions in the peak Te spot, at the investigated concentrations, in the two charge states for O. The share of O gross erosion obviously increases with the concentration, and does so much faster in the high charge state case, becoming predominant with respect to He already at 1% concentration. It can be noticed that as the O concentration is low and He is still the main gross erosion source, the resulting erosion profiles will be shaped similarly to the pure He base case, although with the erosion enhancement due to the O. Instead, as the erosion contribution of O grows, the shape of the erosion profile is greatly modified, tending to resemble the profile that would be obtained in a pure O plasma.

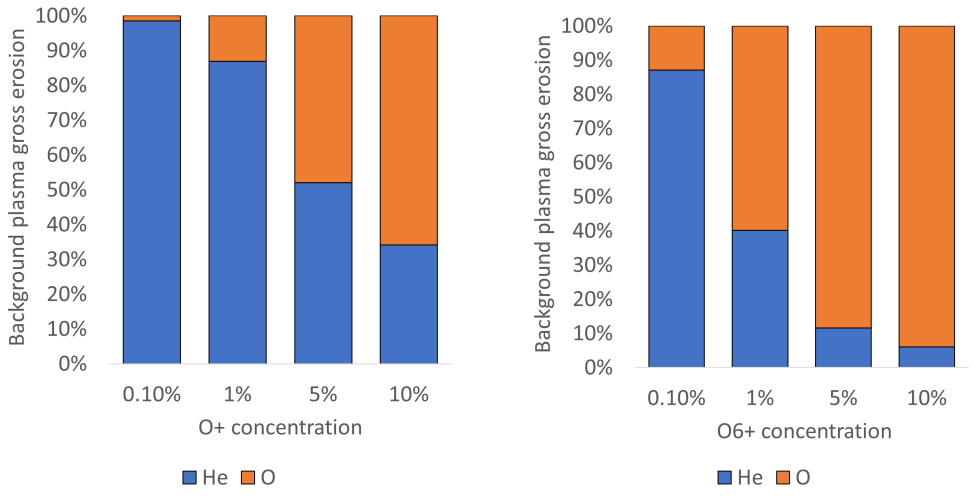

Figure 5.5: Share of gross erosion caused by the background plasma He and O ions at varying O concentration, for the two charge state cases.

5.1.4. Combination of parameters

This subsection will build on the parametric scans performed in the previous three subsections, by considering hybrid conditions in which more than one of the examined parameters is applied simultaneously. This will allow to consider the combination of their erosion enhancement effects, allowing to get net erosion results closer to the experimental reference while considering narrower ranges and less extreme variations of the considered parameters.

The first scenario is set by taking into account the two temperature coefficients simultaneously. It is done by first setting a fixed value for the Ti coefficient equal to 2, as it has been identified as a reasonable variation of the parameter according to the uncertainty on the SOLPS-ITER profile, and then performing the same parametric scan as before for the Te coefficient, in the 1.5-3 range. Figure 5.6 reports the net erosion profiles resulting from these simulations, along with the ones from the previous parametric scan on Te for reference.

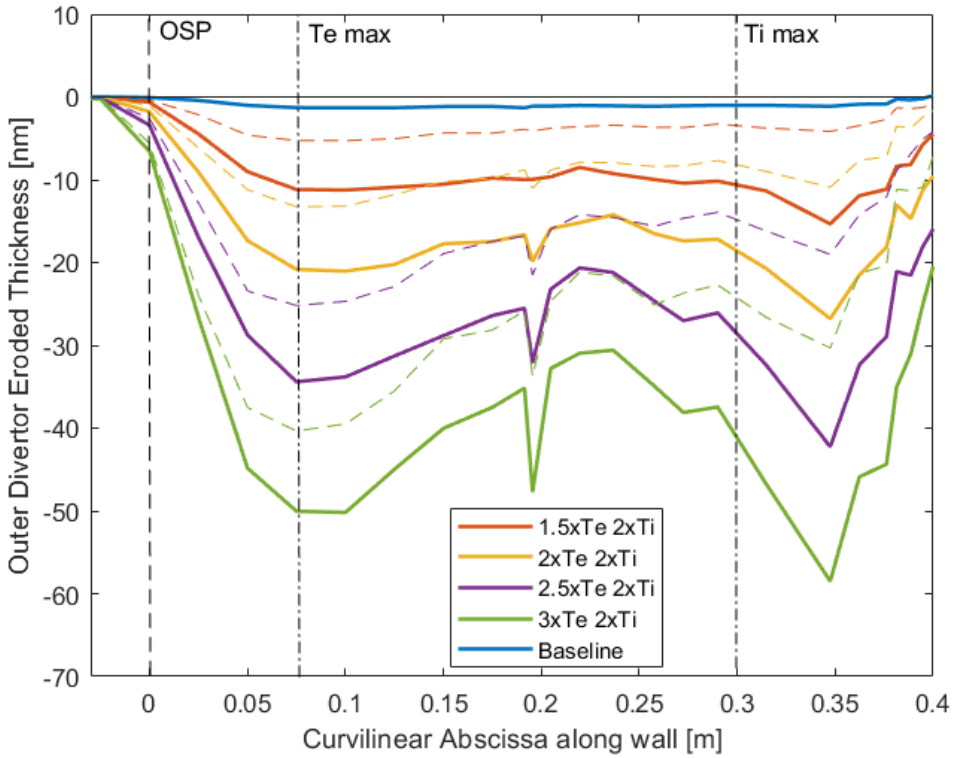

Figure 5.6: 1D net erosion profiles along the outer divertor, resulting from the parametric scan on the Te coefficient while simultaneously applying a Ti coefficient equal to 2. The results of the original Te scan are also reported in dashed lines.

As can be seen, the addition of the Ti coefficient leads to an increase of the erosion relatively to the original Te scan, although mostly concentrated in the maximum Ti region, while only a mild increase is observed in the maximum Te region, where the erosion peak previously arose at increasing Te coefficient. Thus, this leads to the formation of two peaks, roughly of the same intensity, near the Te and Ti maximums. The final step is to consider all three parameters at the same time. Therefore, simulations are performed considering again a fixed Ti coefficient equal to two, and the same is done for the Te coefficient. The parametric scan is then performed on the O impurity concentration, for the high charge state scenario. The investigated range will be different from section 5.1.3, because the simultaneous application of the temperature coefficients allows to reach net erosion values comparable to the experimental one at lower O concentrations, not needing to inquire the extremely high O contents above few %. In fact, the examined range will be 0.1-3%, and results are shown in figure 5.7.

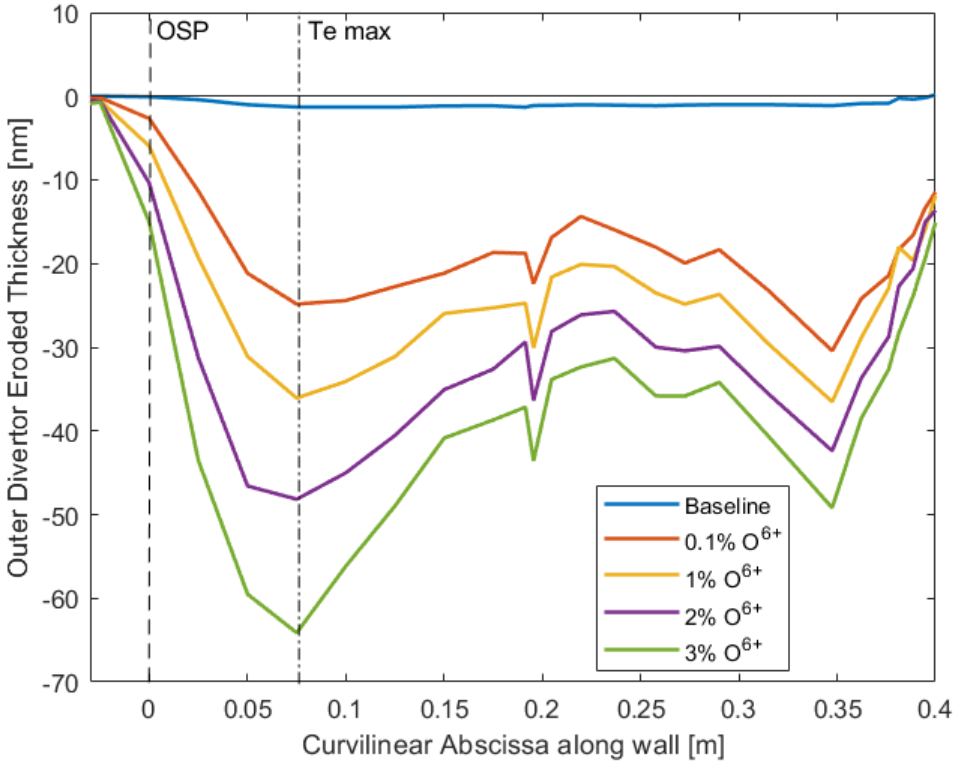

Figure 5.7: 1D net erosion profiles along the outer divertor, resulting from the parametric scan on the high charge state oxygen concentration, while simultaneously applying Te and Ti coefficients both equal to 2.

The resulting erosion profiles share many features with the previous results, showing the

two peaks near Te and Ti maximums like in figure 5.6, but with a higher intensity of the former due to the presence of O impurities, which was shown in section 5.1.3 to enhance erosion near the maximum Te. Overall, it can be concluded that applying all parameters simultaneously enables to match the experimental reference for the erosion with less extreme assumptions than the ones necessary in each individual parametric scan shown previously.

5.2. Evolution of the erosion profile at the following time steps

The work presented up to this point was entirely done in a single time step framework. In this kind of simulations, test particles are launched based on the initial erosion by the background plasma, then particles are followed in their migration until they are re-deposited somewhere, and their contribution to erosion is also computed, but without launching new test particles. This means that the total calculated erosion takes into account the one caused both by the plasma and traced impurities, whereas the deposition is calculated only for the impurities initially eroded by the plasma. Therefore, an unbalance exist between the computed gross erosion and the total deposition, which affects the resulting net erosion profiles. This can be adjusted by performing multiple time steps simulations, in which test particles are launched taking into account also the erosion due to the traced impurities of the previous step, hence allowing to find a steady state net erosion profile after a few steps which is more accurate.
Some results in this perspective will be presented in this section, showing how the net erosion profile evolves at the following time steps. Two cases are selected to observe the evolution, namely the base case, shown in figure 5.8, and the one with Te and Ti coefficients equal to 2, with 2% O^{6+} concentration, shown in figure 5.9, where the profiles at selected time steps are reported. General observations can be made in a similar way for both cases. Coherently with what was explained above, the general trend is a decrease of the net erosion at the following time steps, as the steady state regime is established and the deposition increases, being able to account for the deposition of particles eroded by other impurities at the previous steps. Net deposition zones also arise as steady state is settled, in particular it can be appreciated that in both cases it happens very close to the outer strike point location. This means that particles in that region are more likely to be prompted re-deposited, whereas farther from the separatrix they are more free to migrate for longer distances, leading to a net flux of impurities towards the OSP.

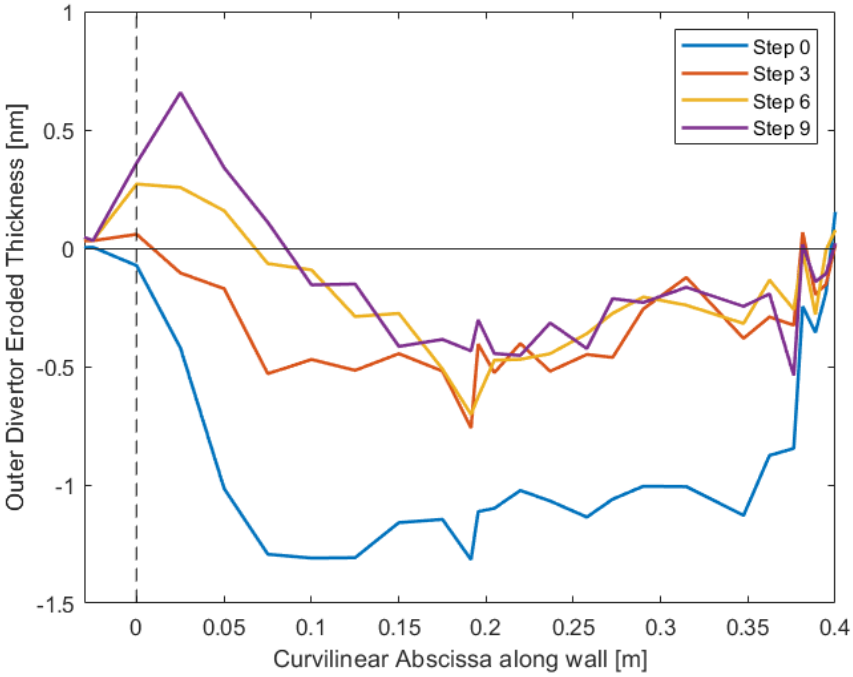

Figure 5.8: Evolution of the 1D net erosion profile for the base case on the outer divertor at the following time steps.

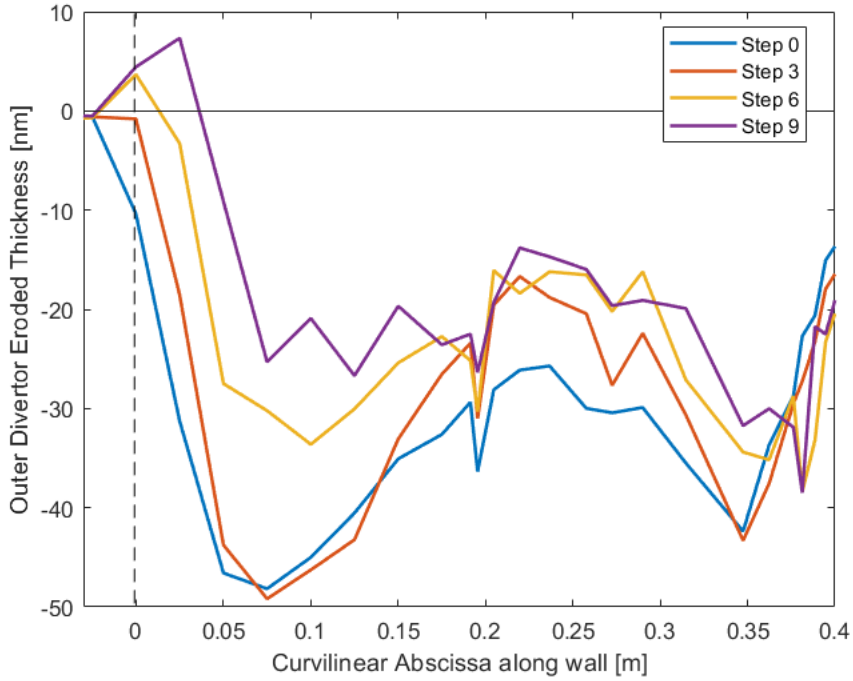

Figure 5.9: Evolution of the 1D net erosion profile for the 2xTe, 2xTi, 2% O^{6+} case on the outer divertor at the following time steps.

5.3. The effect of considering realistic m_{eff} and Z_{eff} distributions

This last section will recall the topic of the role of the two charge states of He in the plasma, introduced in section 3.3. Simulations performed up to this point considered only the He^{2+} component in the plasma as it is by far the dominant component among the two, leading to a good approximation of the real conditions. Moreover, the erosion by both components is correctly accounted for, by adding the fluxes of He^{+} to the outer divertor surface. However, some differences may arise in the description of impurity migration, especially in the OSP region where a higher He^{+} content is expected, and it can be useful to improve the accuracy of the model in this aspect.

A recent development of the code allows to better represent different plasma species, by setting variable distributions of the effective mass (M_{eff}) and charge state (Z_{eff}) over the simulation volume that describe the local concentration of the different species. The main parameter affected by this correction is the electron density (n_e), which was underestimated, as it considered only the fraction attributable to the He^{2+} component. Figure 5.10 shows a comparison between the old n_e and the new one, where the significant difference around the OSP can be appreciated.

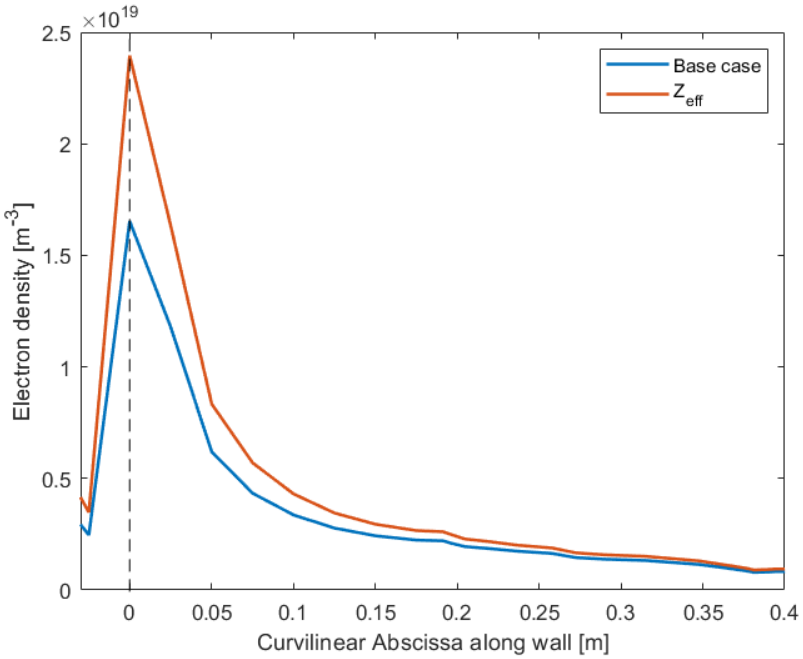

Figure 5.10: Comparison of the electron density profile in the simulation volume between the base case and the Z_{eff} case.

A simulation in this new condition was performed in order to make a comparison with the old one, particularly focusing on the different behaviour in impurity migration. To evaluate this aspect, the time averaged W impurity density across the simulation volume can be a good indicator of different migration patterns, thus figure 5.11 shows a comparison between the two cases.

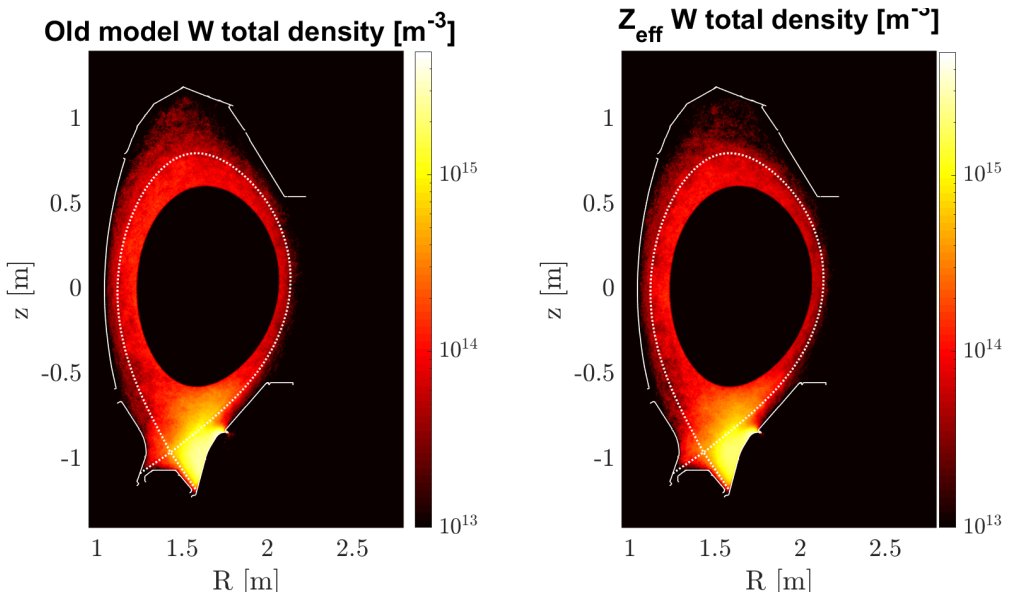

Figure 5.11: Comparison of the time averaged density of W impurities in the simulation volume between the old model (left) and the Z_{eff} case (right).

The distributions appear very similar, however a slightly lower intensity can be appreciated in the Z_{eff} scenario, especially in the divertor region. This means that impurities are less likely to migrate far from their erosion location and their prompt re-deposition is favored, leading to a smaller average impurity density in the plasma. To gain further insight, the net erosion profiles can also be compared. The erosion caused by the background plasma does not change, as the old scenario correctly accounted for the erosion caused by both species, however, differences in migration may lead to a different erosion by the impurities, hence to different net erosion profiles, which can be appreciated in figure 5.12. The net erosion in Z_{eff} case is seen to decrease, the reason may be found looking at the data collected in table 5.1. The first three rows report the average tracing time, impact energy and charge state of test particles depositing on the outer divertor. All these quantities are lower in the Z_{eff} scenario, meaning that particles migrate over shorter distances, having less time to be ionized, leading in turn to a lower energy gain across the plasma sheath, hence to a lower erosion.

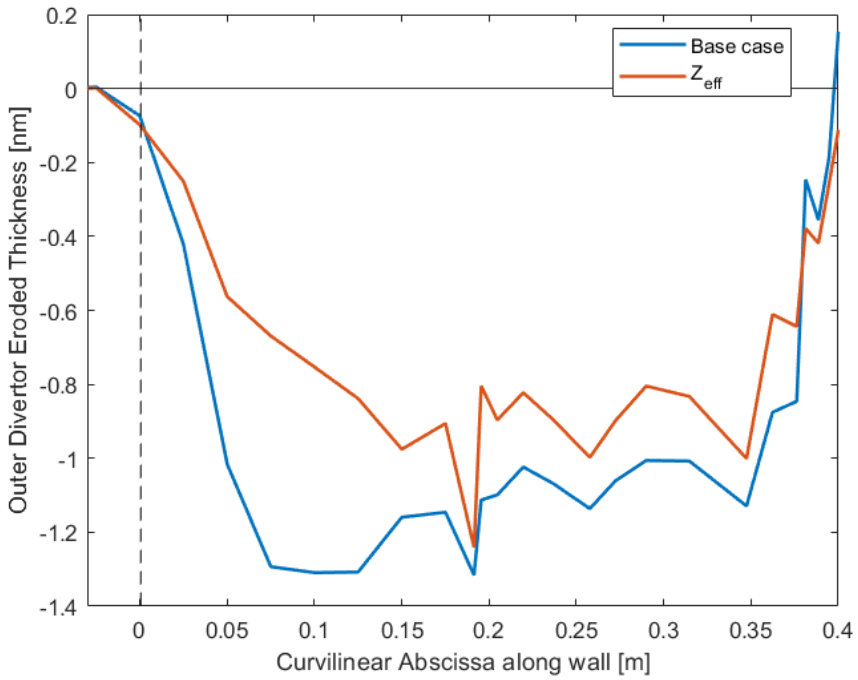

Figure 5.12: Comparison of the 1D net erosion profile on the outer divertor between the base case and the Z_{eff} case.

	Base case	**Z_{eff}**
Tracing time	2.06e-04 s	1.62e-04 s
Impact energy	155.8 eV	116.2 eV
Charge state	1.935	1.732
Tracing time (near OSP)	1.70e-04 s	1.14e-04 s
Impact energy (near OSP)	144.4 eV	84.5 eV
Charge state (near OSP)	1.728	1.483

Table 5.1: Average tracing time, impact energy and charge state of test particles depositing on the whole outer divertor (first three rows) and on a limited region of the outer divertor near the OSP (last three rows), where the peak n_e is located.

The last three rows report the same quantities, but related only to a small outer divertor region around the OSP, where the peak electron density is located. All quantities decrease significantly with respect to the average over the whole divertor, and do so more in the Z_{eff} case. This means that the higher electron density may be favoring quicker deposition, thus being responsible of the erosion reduction in the Z_{eff} case. This may also help to

explain the evolution of the net erosion profile shown in the previous section, where net deposition emerged in the proximity of OSP. In fact, the higher density in that spot favors prompt re-deposition, whereas particles eroded farther from the OSP are able to travel longer distances, leading to a net flux of impurities towards the OSP.

6 | Conclusions and future perspectives

The present thesis work has been produced in the context of PWI studies in magnetic confinement devices for nuclear fusion. Chapter 1 introduced the general topic of magnetic nuclear fusion, while then narrowing its focus on the issue of the interaction between the plasma state of matter, needed to produce the conditions necessary for nuclear fusion to occurr, and the solid walls of the machines. Chapter 2 treated more in-depth the specific subject of the wall erosion mechanism arising from the PWI and the subsequent transport of eroded impurities in the plasma, highlighting their ability to hinder the successful achievement of a self-sustaining thermonuclear plasma, hence evidencing the need to study and control the phenomenon.
In the same chapter the role of linear plasma devices in providing a simpler way to study PWI, while also reproducing ITER relevant plasma conditions, not always obtainable in todays tokamaks, was presented. The same was done for numerical codes able to simulate these processes, referring particularly to the ERO2.0 code, as their coupling with experimental activities provides a great boost to the knowledge acquisition and reinforces the predictive capability of future experiments.
Helium was presented as a plasma species of interest, since its presence in D-T plasma as a reaction product makes it necessary to assess its behaviour in PWI processes, which is characterized by a higher sputtering capability, thanks to its higher mass and Z, and by the possibility to induce modifications on the surface of fusion relevant materials, such as W, altering their properties.
Few studies in literature have tackled the topic of modelling the PWI relatively to a He plasma, especially in a global perspective, simulating the whole plasma volume of the machines thanks to the higher computational capabilities of ERO2.0 with respect to the former version. Thus, the motivations behind this thesis work emerged, as its scope was to apply ERO2.0 to a He plasma both in a tokamak, which occurred to be ASDEX Upgrade, and in a linear device, exploiting the GyM linear device, to study the behaviour of He in a variety of machine geometry, plasma conditions and wall materials.

The work on GyM was developed on two levels: on a global scale and on a local one. Global simulations involve the modelling of the entire plasma volume and all plasma facing components simultaneously. They were used to test erosion and deposition patterns at varying bias applied to selected PFCs, hence varying impact energy, and for different wall materials, where the stainless steel of the vacuum chamber was simulated through full Fe, full Cu, as a proxy for alloying elements, and realistic multi-element steel compositions. The presence of an additional PFC, namely the sample-holder, which was not accounted for in a previous articles, was also tested in these simulations, enabling to make comparison between the two cases.

The gross erosion rate of the lateral wall of the vacuum chamber was studied, due to its peculiarity as the largest PFC in the machine and the main deposition spot of most eroded impurities, while not being directly sputtered by the plasma. Thus, its gross erosion relation with the strength of impurity sources was highlighted by the results, as it increased at increasing bias applied to the other PFCs. The full Cu wall assumption proved to be far from reality, as it highly overestimated the erosion, whereas full Fe gave results comparable to the realistic steel. Still, even the full Fe slightly overestimated the steel case, as the Cr component in the steel tends to decrease the erosion, thanks to its lower sputtering yields when struck by a He ion. It was also seen that adding the erosion caused by particles sputtered from the lateral wall itself, evaluated through multiple time steps simulations, caused only a small correction, within 10%, to the erosion calculated at the first step.

Another PFC of interest were the W samples carried in the sample-holder, as they are the subject of PWI studies in experimental activities. Unlike the lateral wall, their erosion rate proved to be mostly independent of the material of surrounding walls, especially when bias applied to them is enough to overcome the He on W sputtering threshold and being directly sputtered by the plasma.

The W samples were also the object of simulations at the local microscale level, where only a small volume in the proximity of the surface is simulated, allowing an accurate description of the surface morphology. The surfaces of real samples were thus reproduced through AFM measurements, and a comparison was made possible between simulations results and experimental measures on the effective erosion of the samples, affected by the specific surface morphology of each sample. The general observation was a substantial overestimate by the simulations, regardless of the specific considered sample. However, the agreement was greatly improved by considering modified sputtering yields, which account for He retention in the W surface, causing a shielding effect on the W atoms and reducing the erosion.

In AUG, simulations were conducted with the global approach, and most of the work

was directed at reproducing the PWI processes experienced during the 2019 L-mode He plasma discharge, with particular focus on the net eroded thickness on the outer divertor. A reference experimental value of 50 nm was provided, with the goal of matching it in simulations. Preliminary simulations showed a heavy underestimation of the net erosion, by a couple of orders of magnitude. Thus, a parametric analysis was conducted over selected quantities to investigate the source of such discrepancy. The scanned parameters were fixed coefficients multipliying electron and ion temperatures and oxygen impurity concentration, assessing a high and a low charge state case. The 1D net erosion profile was obtained at different values of these parameters, observing the erosion enhancement, as well as the profile shape modification. The application of the parameters was also combined together, observing their simultaneous effects, obtaining finally net erosion values comparable with the experimental reference.

The net erosion profile was also evaluated in its evolution at following time steps, where a more accurate description is given when a steady state regime of erosion and deposition is established. The overall trend was a decrease of net erosion, particularly in the OSP region, where a net deposition zone emerges.

Finally the role of the two He charge states was investigated by using a variable distribution of the effective charge state in the volume, a more accurate description of the previous model, which considered only the He^{2+} component. The observed effect was a reduction of the W impurity content in the volume, mainly attributable to the higher electron density of the new model, which favors a quicker deposition of W impurities, in turn leading to a reduction of net erosion.

Overall, this thesis work contributed to expand the knowledge on the behaviour of He plasmas by the point of view of PWI modelling through the ERO2.0 code, in a wide range of geometries and plasma conditions. Global descriptions of the AUG tokamak and the GyM linear device were given, allowing a complete description of the production of impurities and their long range migration in the plasma volume.

In light of the work presented, a few future developments are possible. For instance, in GyM, the possibility to include the sample-holder in the modelling of the plasma in SOLPS-ITER may be evaluated. A comparison of the global erosion and deposition results with experimental measurements may be foreseen in the future, to validate the modelling of the machine in the global approach. Moreover, a link between global and local simulations can be established, by comparing for instance the erosion of the samples in the two approaches. About local simulations, an improvement may be given by the correct description of oxygen in the W+O samples.

In AUG, the most straightforward approach for the next steps is to model other discharges through SOLPS-ITER, and in turn use the new background plasmas to perform simula-

tions in ERO2.0, comparing results with the work reported here. In particular, the 2022 L-mode discharge, which should share many features with the 2019 one, can be modelled, while its outer divertor erosion can be compared with the results presented in this thesis and with the experimental reference value of the net eroded thickness. In the future the same may be done even for H-mode discharges, thus allowing to shed light on the different behaviour of the two modes relatively to the outer divertor erosion.

Bibliography

[1] Max Roser. The world's energy problem. *Our World in Data*, 2020. https://ourworldindata.org/worlds-energy-problem.

[2] Hoesung Lee, Katherine Calvin, Dipak Dasgupta, Gerhard Krinner, Aditi Mukherji, Peter Thorne, Christopher Trisos, José Romero, Paulina Aldunce, Ko Barret, et al. Ipcc, 2023: Climate change 2023: Synthesis report, summary for policymakers. contribution of working groups i, ii and iii to the sixth assessment report of the intergovernmental panel on climate change [core writing team, h. lee and j. romero (eds.)]. ipcc, geneva, switzerland. 2023.

[3] Hannah Ritchie and Pablo Rosado. Energy mix. *Our World in Data*, 2020. https://ourworldindata.org/energy-mix.

[4] Kenneth S Krane. *Introductory nuclear physics*. Wiley, New York, NY, 1988.

[5] J.P. Freidberg. *Plasma Physics and Fusion Energy*. Cambridge University Press, 2008.

[6] Lorenzo Giuffrida, Fabio Belloni, Daniele Margarone, Giada Petringa, Giuliana Milluzzo, Valentina Scuderi, Andriy Velyhan, Marcin Rosinski, Antonino Picciotto, Milan Kucharik, et al. High-current stream of energetic α particles from laser-driven proton-boron fusion. *Physical Review E*, 101(1):013204, 2020.

[7] D Mazzucconi, D Vavassori, D Dellasega, FM Airaghi, S Agosteo, M Passoni, A Pola, and D Bortot. Proton boron fusion reaction: A novel experimental strategy for cross section investigation. *Radiation Physics and Chemistry*, 204:110727, 2023.

[8] F. F. Chen. *Introduction to plasma physics*. New York: Plenum Press, 1974.

[9] Roger D. Blandford and Kip S. Thorne. Applications of classical physics. 2013.

[10] John D Lawson. Some criteria for a power producing thermonuclear reactor. *Proceedings of the physical society. Section B*, 70(1):6, 1957.

[11] S Leray. Nuclear energy basics. In *EPJ Web of Conferences*, volume 268, page 00008. EDP Sciences, 2022.

[12] John Nuckolls, Lowell Wood, Albert Thiessen, and George Zimmerman. Laser compression of matter to super-high densities: Thermonuclear (ctr) applications. *Nature*, 239(5368):139–142, 1972.

[13] R Betti and OA Hurricane. Inertial-confinement fusion with lasers. *Nature Physics*, 12(5):435–448, 2016.

[14] H Abu-Shawareb, R Acree, P Adams, J Adams, B Addis, R Aden, P Adrian, BB Afeyan, M Aggleton, L Aghaian, et al. Lawson criterion for ignition exceeded in an inertial fusion experiment. *Physical review letters*, 129(7):075001, 2022.

[15] Jeff Tollefson and Elizabeth Gibney. Nuclear-fusion lab achieves 'ignition': What does it mean? *Nature*, 612(7941):597–598, 2022.

[16] Samuel E Wurzel and Scott C Hsu. Progress toward fusion energy breakeven and gain as measured against the lawson criterion. *Physics of Plasmas*, 29(6), 2022.

[17] KM McGuire, H Adler, P Alling, C Ancher, H Anderson, JL Anderson, John W Anderson, V Arunasalam, G Ascione, D Ashcroft, et al. Review of deuterium–tritium results from the tokamak fusion test reactor. *Physics of Plasmas*, 2(6):2176–2188, 1995.

[18] M Keilhacker, A Gibson, C Gormezano, PJ Lomas, PR Thomas, ML Watkins, P Andrew, B Balet, D Borba, CD Challis, et al. High fusion performance from deuterium-tritium plasmas in jet. *Nuclear Fusion*, 39(2):209, 1999.

[19] A. J. Creely, M. J. Greenwald, S. B. Ballinger, D. Brunner, J. Canik, J. Doody, T. Fülöp, D. T. Garnier, R. Granetz, T. K. Gray, and et al. Overview of the sparc tokamak. *Journal of Plasma Physics*, 86(5), 2020.

[20] R Aymar, P Barabaschi, and Y Shimomura. The iter design. *Plasma physics and controlled fusion*, 44(5):519, 2002.

[21] Sergio Ciattaglia, Gianfranco Federici, Luciana Barucca, Alessandro Lampasi, Simone Minucci, and Ivo Moscato. The european demo fusion reactor: Design status and challenges from balance of plant point of view. In *2017 IEEE International Conference on Environment and Electrical Engineering and 2017 IEEE Industrial and Commercial Power Systems Europe (EEEIC/I&CPS Europe)*, pages 1–6. IEEE, 2017.

[22] Hugh D Young. *University Physics (For Pune University), 11/E*. Pearson Education India, 2008.

[23] P.C. Stangeby. *The Plasma Boundary of Magnetic Fusion Devices*. Series in Plasma Physics and Fluid Dynamics. Taylor & Francis, 2000.

[24] J. Wesson and D.J. Campbell. *Tokamaks*. International series of monographs on physics. Clarendon Press, 2004.

[25] Max planck institute for plasma physics web page. `https://www.ipp.mpg.de/14953/weltweit`. Accessed: 2024-01-27.

[26] Masahiro Wakatani. *Stellarator and heliotron devices*, volume 95. Oxford University Press, USA, 1998.

[27] Per Helander, CD Beidler, TM Bird, M Drevlak, Y Feng, R Hatzky, F Jenko, R Kleiber, JHE Proll, Yu Turkin, et al. Stellarator and tokamak plasmas: a comparison. *Plasma Physics and Controlled Fusion*, 54(12):124009, 2012.

[28] J Ongena, R Koch, R Wolf, and H Zohm. Magnetic-confinement fusion. *Nature Physics*, 12(5):398–410, 2016.

[29] Raoul N Franklin. Plasma phenomena in gas discharges. *Oxford and New York*, 1976.

[30] PC Stangeby and GM McCracken. Plasma boundary phenomena in tokamaks. *Nuclear Fusion*, 30(7):005, 1990.

[31] Peter C Stangeby. The plasma sheath. In *Physics of Plasma-Wall Interactions in Controlled Fusion*, pages 41–97. Springer, 1986.

[32] Lewi Tonks and Irving Langmuir. A general theory of the plasma of an arc. *Physical review*, 34(6):876, 1929.

[33] Robert J Goldston. *Introduction to plasma physics*. CRC Press, 2020.

[34] Roland Chodura. Plasma–wall transition in an oblique magnetic field. *The Physics of Fluids*, 25(9):1628–1633, 1982.

[35] Douglass Edmund Post and Rainer Behrisch. *Physics of plasma-wall interactions in controlled fusion*. Springer Science & Business Media, 2013.

[36] W Eckstein and H Verbeek. Reflection of light ions from solids. In *Data compendium for plasma-surface interactions*, pages 12–12. Nucl. Fusion special issue, 1984.

[37] R Behrisch and W Eckstein. Ion backscattering from solid surfaces. In *Physics of Plasma-Wall Interactions in Controlled Fusion*, pages 413–438. Springer, 1986.

[38] W Eckstein. Reflection. In *Atomic and plasma-material interaction data for fusion. Vol. 1*. 1991.

[39] WR Wampler, DK Brice, and CW Magee. Saturation of deuterium retention in carbon a new calibration for plasma edge probes. *Journal of Nuclear Materials*, 102(3):304–312, 1981.

[40] Wolfhard Möller. Hydrogen trapping and transport in carbon. *Journal of Nuclear Materials*, 162:138–150, 1989.

[41] Rion A Causey. The interaction of tritium with graphite and its impact on tokamak operations. *Journal of Nuclear Materials*, 162:151–161, 1989.

[42] KL Wilson, R Bastasz, RA Causey, DK Brice, BL Doyle, WR Wampler, W Moller, BMU Scherzer, and T Tanabe. Trapping, detrapping and release of implanted hydrogen isotopes. *Nucl. Fusion*, 1:31, 1991.

[43] BD Wirth, K Nordlund, DG Whyte, and D Xu. Fusion materials modeling: Challenges and opportunities. *MRS bulletin*, 36:216–222, 2011.

[44] P Andrew, D Brennan, JP Coad, J Ehrenberg, M Gadeberg, A Gibson, M Groth, J How, ON Jarvis, H Jensen, et al. Tritium recycling and retention in jet. *Journal of nuclear materials*, 266:153–159, 1999.

[45] Wilfred Effingham Dasent. *Inorganic energetics: an introduction*. CUP Archive, 1982.

[46] Ghadeer H Al-Malkawi, Al-Montaser Bellah A Al-Ajlony, and Khaled F AL-Shboul. Computer simulation of the sputtering energy thresholds for some plasma-facing component materials irradiated with helium, deuterium, and tritium ions. *Nuclear Materials and Energy*, 35:101442, 2023.

[47] J Bohdansky. A universal relation for the sputtering yield of monatomic solids at normal ion incidence. *Nuclear Instruments and Methods in Physics Research Section B: Beam Interactions with Materials and Atoms*, 2(1-3):587–591, 1984.

[48] W Eckstein, J Bohdansky, and J Roth. Physical sputtering. *Nucl. Fusion*, 1:51, 1991.

[49] Wolfgang Eckstein, C Garcia-Rosales, J Roth, and W Ottenberger. Sputtering data. 1993.

[50] W Eckstein and R Preuss. New fit formulae for the sputtering yield. *Journal of Nuclear Materials*, 320(3):209–213, 2003.

[51] Yasumichi Yamamura, Yukikazu Itikawa, and Noriaki Itoh. Angular dependence of sputtering yields of monatomic solids. *Unknown*, 1983.

[52] Andreas Mutzke, Ralf Schneider, Wolfgang Eckstein, Renate Dohmen, K Schmid, U von Toussaint, and G Badelow. Sdtrimsp version 6.00. 2019.

[53] H Hofsäss, K Zhang, and A Mutzke. Simulation of ion beam sputtering with sdtrimsp, tridyn and srim. *Applied Surface Science*, 310:134–141, 2014.

[54] GF Matthews. Material migration in divertor tokamaks. *Journal of nuclear materials*, 337:1–9, 2005.

[55] SI Krasheninnikov, Y Tomita, RD Smirnov, and RK Janev. On dust dynamics in tokamak edge plasmas. *Physics of Plasmas*, 11(6):3141–3150, 2004.

[56] JD Strachan, W Fundamenski, M Charlet, G Corrigan, K Erents, J Gafert, C Giroud, C Gowers, M von Hellermann, LD Horton, et al. Jet carbon screening experiments using methane gas puffing and its relation to intrinsic carbon impurities. *Nuclear Fusion*, 43(9):922, 2003.

[57] SK Rathgeber, R Fischer, S Fietz, J Hobirk, A Kallenbach, H Meister, T Pütterich, F Ryter, G Tardini, E Wolfrum, et al. Estimation of profiles of the effective ion charge at asdex upgrade with integrated data analysis. *Plasma Physics and Controlled Fusion*, 52(9):095008, 2010.

[58] RA Pitts, JP Coad, DP Coster, G Federici, W Fundamenski, J Horacek, K Krieger, A Kukushkin, Jari Likonen, GF Matthews, et al. Material erosion and migration in tokamaks. *Plasma physics and controlled fusion*, 47(12B):B303, 2005.

[59] J Von Seggern, P Wienhold, T Hirai, V Philipps, and HG Esser. Long term behaviour of material erosion and deposition on the vessel wall and remote areas of textor. *Journal of nuclear materials*, 313:439–443, 2003.

[60] Jari Likonen, Elizaveta Vainonen-Ahlgren, JP Coad, Riitta Zilliacus, Tommi Renvall, DE Hole, M Rubel, Kai Arstila, GF Matthews, M Stamp, et al. Beryllium accumulation at the inner divertor of jet. *Journal of nuclear materials*, 337:60–64, 2005.

[61] V Rohde, R Dux, M Mayer, R Neu, T Pütterich, and W Schneider. Material transport in asdex upgrade. *Physica Scripta*, 2004(T111):49, 2004.

[62] GF Matthews, M Stamp, P Coad, J Likonen, V Philipps, M Rubel, JD Strachan, and JET EFDA Contributors. Material migration in jet. In *Proc. 30th EPS Conf. on Controlled Fusion and Plasma Physics (St. Petersburg)*, volume 27, 2003.

[63] Ch Linsmeier, B Unterberg, JW Coenen, RP Doerner, H Greuner, A Kreter, J Linke, and H Maier. Material testing facilities and programs for plasma-facing component testing. *Nuclear Fusion*, 57(9):092012, 2017.

[64] Arkadi Kreter, C Brandt, A Huber, S Kraus, Sören Möller, M Reinhart, B Schweer, G Sergienko, and B Unterberg. Linear plasma device psi-2 for plasma-material interaction studies. *Fusion science and technology*, 68(1):8–14, 2015.

[65] D Naujoks, R Behrisch, JP Coad, and LCJM De Kock. Material transport by erosion and redeposition on surface probes in the scrape-off layer of jet. *Nuclear fusion*, 33(4):581, 1993.

[66] A Kirschner, V Philipps, J Winter, and U Kögler. Simulation of the plasma-wall interaction in a tokamak with the monte carlo code ero-textor. *Nuclear Fusion*, 40(5):989, 2000.

[67] Juri Romazanov. *3D simulation of impurity transport in a fusion edge plasma using a massively parallel Monte-Carlo code*. Number FZJ-2019-01018. Plasmaphysik, 2018.

[68] C Bourdelle, JF Artaud, Vbulandi Basiuk, M Bécoulet, S Brémond, J Bucalossi, H Bufferand, G Ciraolo, L Colas, Y Corre, et al. West physics basis. *Nuclear Fusion*, 55(6):063017, 2015.

[69] Hendrik Meyer, C Angioni, CG Albert, Nils Arden, R Arredondo Parra, O Asunta, M De Baar, M Balden, V Bandaru, K Behler, et al. Overview of physics studies on asdex upgrade. *Nuclear Fusion*, 59(11):112014, 2019.

[70] Sebastijan Brezinsek, JET-EFDA contributors, et al. Plasma-surface interaction in the be/w environment: conclusions drawn from the jet-ilw for iter. *Journal of nuclear materials*, 463:11–21, 2015.

[71] Sebastijan Brezinsek, Andreas Kirschner, Matej Mayer, A Baron-Wiechec, Irina Borodkina, Dmitriy Borodin, I Coffey, J Coenen, Niek den Harder, Alina Eksaeva, et al. Erosion, screening, and migration of tungsten in the jet divertor. *Nuclear fusion*, 59(9):096035, 2019.

[72] Antti Hakola, Jari Likonen, Aki Lahtinen, Tomi Vuoriheimo, Mathias Groth, H Kumpulainen, Martin Balden, Karl Krieger, Matej Mayer, Thomas Schwarz-

Selinger, et al. Gross and net erosion balance of plasma-facing materials in full-w tokamaks. *Nuclear Fusion*, 61(11):116006, 2021.

[73] S Brezinsek, Antti Hakola, H Greuner, M Balden, A Kallenbach, M Oberkofler, G De Temmerman, D Douai, Aki Lahtinen, B Böswirth, et al. Surface modification of he pre-exposed tungsten samples by he plasma impact in the divertor manipulator of asdex upgrade. *Nuclear materials and energy*, 12:575–581, 2017.

[74] Antti Hakola, Seppo Koivuranta, Jari Likonen, A Herrmann, H Maier, M Mayer, R Neu, V Rohde, ASDEX Upgrade Team, et al. Erosion of tungsten and steel in the main chamber of asdex upgrade. *Journal of Nuclear Materials*, 463:162–165, 2015.

[75] R Dux, V Bobkov, A Herrmann, A Janzer, A Kallenbach, R Neu, M Mayer, HW Müller, R Pugno, T Pütterich, et al. Plasma-wall interaction and plasma behaviour in the non-boronised all tungsten asdex upgrade. *Journal of Nuclear Materials*, 390:858–863, 2009.

[76] Martin Balden, M Mayer, B Bliewert, E Bernard, M Diez, M Firdaouss, M Missirlian, B Pégourié, M Richou, H Roche, et al. Erosion and redeposition patterns on entire erosion marker tiles after exposure in the first operation phase of west. *Physica Scripta*, 96(12):124020, 2021.

[77] DM Goebel, G Campbell, and RW Conn. Plasma surface interaction experimental facility (pisces) for materials and edge physics studies. *Journal of Nuclear Materials*, 121:277–282, 1984.

[78] Y Hirooka, RW Conn, T Sketchley, WK Leung, G Chevalier, R Doerner, J Elverum, DM Goebel, G Gunner, M Khandagle, et al. A new plasma-surface interactions research facility: Pisces-b and first materials erosion experiments on bulk-boronized graphite. *Journal of Vacuum Science & Technology A: Vacuum, Surfaces, and Films*, 8(3):1790–1797, 1990.

[79] N Ohno, D Nishijima, S Takamura, Y Uesugi, M Motoyama, N Hattori, H Arakawa, N Ezumi, S Krasheninnikov, A Pigarov, et al. Static and dynamic behaviour of plasma detachment in the divertor simulator experiment nagdis-ii. *Nuclear Fusion*, 41(8):1055, 2001.

[80] GJ Van Rooij, VP Veremiyenko, WJ Goedheer, B De Groot, AW Kleyn, PHM Smeets, TW Versloot, DG Whyte, R Engeln, DC Schram, et al. Extreme hydrogen plasma densities achieved in a linear plasma generator. *Applied physics letters*, 90(12), 2007.

[81] HJN Van Eck, T Abrams, MA Van Den Berg, S Brons, GG Van Eden, MA Jaworski, R Kaita, HJ Van Der Meiden, TW Morgan, Marc J van de Pol, et al. Operational characteristics of the high flux plasma generator magnum-psi. *Fusion Engineering and Design*, 89(9-10):2150–2154, 2014.

[82] Andrea Uccello, William Bin, Alessandro Bruschi, Federica Causa, Anna Cremona, Marco De Angeli, Daniela Farina, Giuseppe Gatto, Gabriele Gervasini, Francesco Ghezzi, et al. Linear plasma device gym for plasma-material interaction studies. *Frontiers in Physics*, 11:1108175, 2023.

[83] Dai Nishijima, MY Ye, N Ohno, and S Takamura. Formation mechanism of bubbles and holes on tungsten surface with low-energy and high-flux helium plasma irradiation in nagdis-ii. *Journal of nuclear materials*, 329:1029–1033, 2004.

[84] MJ Baldwin and RP Doerner. Helium induced nanoscopic morphology on tungsten under fusion relevant plasma conditions. *Nuclear Fusion*, 48(3):035001, 2008.

[85] Shin Kajita, Wataru Sakaguchi, Noriyasu Ohno, Naoaki Yoshida, and Tsubasa Saeki. Formation process of tungsten nanostructure by the exposure to helium plasma under fusion relevant plasma conditions. *Nuclear Fusion*, 49(9):095005, 2009.

[86] Alina Eksaeva, D Borodin, J Romazanov, A Kreter, A Pospieszczyk, S Dickheuer, S Möller, B Göths, M Rasinski, U Knoche, et al. Ero2. 0 modelling of the effects of surface roughness on molybdenum erosion and redeposition in the psi-2 linear plasma device. *Physica Scripta*, 2020(T171):014057, 2020.

[87] M Miyamoto, D Nishijima, Y Ueda, RP Doerner, H Kurishita, MJ Baldwin, S Morito, K Ono, and J Hanna. Observations of suppressed retention and blistering for tungsten exposed to deuterium–helium mixture plasmas. *Nuclear Fusion*, 49(6):065035, 2009.

[88] V Kh Alimov, WM Shu, J Roth, K Sugiyama, S Lindig, M Balden, K Isobe, and T Yamanishi. Surface morphology and deuterium retention in tungsten exposed to low-energy, high flux pure and helium-seeded deuterium plasmas. *Physica Scripta*, 2009(T138):014048, 2009.

[89] Sven Wiesen, Detlev Reiter, Vladislav Kotov, Martine Baelmans, Wouter Dekeyser, AS Kukushkin, SW Lisgo, RA Pitts, Vladimir Rozhansky, Gabriella Saibene, et al. The new solps-iter code package. *Journal of nuclear materials*, 463:480–484, 2015.

[90] J Romazanov, D Borodin, A Kirschner, S Brezinsek, S Silburn, A Huber, V Huber,

H Bufferand, M Firdaouss, D Brömmel, et al. First ero2. 0 modeling of be erosion and non-local transport in jet iter-like wall. *Physica scripta*, 2017(T170):014018, 2017.

[91] D Borodin, S Brezinsek, J Miettunen, M Stamp, A Kirschner, C Björkas, M Groth, S Marsen, C Silva, SW Lisgo, et al. Determination of be sputtering yields from spectroscopic observations at the jet iter-like wall based on three-dimensional ero modelling. *Physica Scripta*, 2014(T159):014057, 2014.

[92] J Romazanov, S Brezinsek, D Borodin, M Groth, S Wiesen, A Kirschner, A Huber, A Widdowson, Markus Airila, A Eksaeva, et al. Beryllium global erosion and deposition at jet-ilw simulated with ero2. 0. *Nuclear materials and energy*, 18:331–338, 2019.

[93] S Di Genova, A Gallo, N Fedorczak, H Yang, G Ciraolo, J Romazanov, Y Marandet, H Bufferand, C Guillemaut, JP Gunn, et al. Modelling of tungsten contamination and screening in west plasma discharges. *Nuclear Fusion*, 61(10):106019, 2021.

[94] AV Chankin, DP Coster, and R Dux. Monte carlo simulations of tungsten redeposition at the divertor target. *Plasma Physics and Controlled Fusion*, 56(2):025003, 2014.

[95] A Gallo, A Sepetys, J Romazanov, Y Marandet, S Brezinsek, H Bufferand, G Ciraolo, Y Corre, S Ertmer, N Fedorczak, et al. First efforts in numerical modeling of tungsten migration in west with soledge2d-eirene and ero2. 0. *Physica scripta*, 2020(T171):014013, 2020.

[96] Juri Romazanov, Sebastijan Brezinsek, Andreas Kirschner, Dmitriy Borodin, Alina Eksaeva, Richard A Pitts, Steven W Lisgo, Himank Anand, Evgeny Veshchev, Vlad S Neverov, et al. First monte-carlo modelling of global beryllium migration in iter using ero2. 0. *Contributions to plasma physics*, 60(5-6):e201900149, 2020.

[97] D Borodin, A Kirschner, S Carpentier-Chouchana, RA Pitts, S Lisgo, C Björkas, PC Stangeby, JD Elder, A Galonska, Dmitry Matveev, et al. Ero code benchmarking of iter first wall beryllium erosion/re-deposition against lim predictions. *Physica scripta*, 2011(T145):014008, 2011.

[98] D Borodin, J Romazanov, RA Pitts, SW Lisgo, S Brezinsek, I Borodkina, A Eksaeva, E Safi, K Nordlund, A Kirschner, et al. Improved ero modelling of beryllium erosion at iter upper first wall panel using jet-ilw and pisces-b experience. *Nuclear materials and energy*, 19:510–515, 2019.

[99] A Eksaeva, D Borodin, J Romazanov, A Kirschner, A Kreter, M Eichler, M Rasinski, A Pospieszczyk, B Unterberg, S Brezinsek, et al. Surface roughness effect on mo physical sputtering and re-deposition in the linear plasma device psi-2 predicted by ero2. 0. *Nuclear materials and energy*, 19:13–18, 2019.

[100] Alina Eksaeva, D Borodin, J Romazanov, A Kirschner, A Kreter, B Göths, M Rasinski, B Unterberg, S Brezinsek, Ch Linsmeier, et al. The impact of surface morphology on the erosion of metallic surfaces–modelling with the 3d monte-carlo code ero2. 0. *Nuclear Materials and Energy*, 27:100987, 2021.

[101] Gabriele Alberti, M Sala, J Romazanov, A Uccello, D Dellasega, and M Passoni. Ero2. 0 modelling of nanoscale surface morphology evolution. *Nuclear Fusion*, 61(6):066039, 2021.

[102] Gabriele Alberti, Elena Tonello, Paolo Carminati, Andrea Uccello, Xavier Bonnin, Juri Romazanov, Sebastijan Brezinsek, and Matteo Passoni. Global solps-iter and ero2. 0 coupling in a linear device for the study of plasma–wall interaction in helium plasma. *Nuclear Fusion*, 63(2):026020, 2023.

[103] R Simonini, G Corrigan, G Radford, J Spence, and A Taroni. Models and numerics in the multi-fluid 2-d edge plasma code edge2d/u. *Contributions to Plasma Physics*, 34(2-3):368–373, 1994.

[104] Hugo Bufferand, B Bensiali, J Bucalossi, G Ciraolo, P Genesio, Ph Ghendrih, Yannick Marandet, A Paredes, F Schwander, E Serre, et al. Near wall plasma simulation using penalization technique with the transport code soledge2d-eirene. *Journal of Nuclear Materials*, 438:S445–S448, 2013.

[105] Y Feng, F Sardei, J Kisslinger, P Grigull, K McCormick, and D Reiter. 3d edge modeling and island divertor physics. *Contributions to Plasma Physics*, 44(1-3):57–69, 2004.

[106] HP Summers. The adas user manual, version 2.6. *http://www. adas. ac. uk/*, 2004.

[107] Hong Qin, Shuangxi Zhang, Jianyuan Xiao, Jian Liu, Yajuan Sun, and William M Tang. Why is boris algorithm so good? *Physics of Plasmas*, 20(8), 2013.

[108] I Borodkina, D Borodin, S Brezinsek, A Kirschner, IV Tsvetkov, VA Kurnaev, V Bobkov, CC Klepper, A Lasa, C Guillemaut, et al. An analytical expression for ion velocities at the wall including the sheath electric field and surface biasing for erosion modeling at jet ilw. *Nuclear Materials and Energy*, 12:341–345, 2017.

[109] The mpi forum webpage. `http://mpi-forum.org`. Accessed: 2024-02-12.

[110] The openmp api specification. ,http://www.openmp.org. Accessed: 2024-02-12.

[111] G Federici, JN Brooks, DP Coster, G Janeschitz, A Kukuskhin, A Loarte, HD Pacher, J Stober, and CH Wu. Assessment of erosion and tritium codeposition in iter-feat. *Journal of nuclear materials*, 290:260–265, 2001.

[112] Joachim Roth, Kazuyoshi Sugiyama, Vladimir Alimov, Till Höschen, Matt Baldwin, and Russ Doerner. Eurofer as wall material: Reduced sputtering yields due to w surface enrichment. *Journal of Nuclear Materials*, 454(1-3):1–6, 2014.

[113] Alberti G.; Tonello E.; Uccello A.; Passoni M. Solps iter and ero2.0 modelling to estimate the influence of eroded impurities from wall and samples on experimental results in gym. 19th International Conference on Plasma-Facing Materials and Components for Fusion Applications - PFMC 19, , Bonn, Germany, May 2023.

[114] Uccello A.; Alberti G.; Cremona A.; Ghezzi F.; Pedroni M.; Vassallo E.; Tonello E.; Vavassori D.; Dellasega D.; Passoni M. Study the role of roughness in the sputtering process of tungsten by gym helium plasma: experiments and ero2.0 modelling. 19th International Conference on Plasma-Facing Materials and Components for Fusion Applications - PFMC 19, , Bonn, Germany, May 2023.

[115] Max planck institute for plasma physics web page. https://www.ipp.mpg.de/5035491/01_21. Accessed: 2024-02-16.

[116] Alberti G.; of E. Tonello; F. Mombelli; J. Romazanov ; M. Passoni. Further progress about w-he interaction modelling in asdex upgrade. 33rd Meeting of the ITPA Scrape Off Layer and Divertor Topical Group, ORNL, Oak Ridge,, June 2023.

[117] G.Alberti; E. Tonello; F. Mombelli; A. Uccello; C. Carati and M. Passoni. Modelling plasma wall interaction in a tokamak: the helium plasma case in asdex upgrade. CMD30 FisMat 2023 Joint Conference, Milan, Italy, September 2023.

[118] C Christopher Klepper, Ezekial A Unterberg, Y Marandet, D Curreli, A Grosjean, Jeffrey H Harris, Curtis A Johnson, A Gallo, M Goniche, Ch Guillemaut, et al. Characterizing w sources in the all-w wall, all-rf west tokamak environment. *Plasma Physics and Controlled Fusion*, 64(10):104008, 2022.

List of Figures

1.1 Global energy consumption by energy source [3]. The increasing trend can be easily noted. . . . 2
1.2 Nuclei binding energy per nucleon . . . 3
1.3 Cross section dependence on center of mass energy for each fusion reaction 5
1.4 Lawson criterion threshold curve for different fusion reactions. Similarly to the cross section curves, D-T is the most favorable reaction having the lowest threshold and the minimum of the curve at a lower temperature. Taken from [11] . . . 9
1.5 Q and Q_{eng} as functions of the triple product relative to the ignition threshold value [5] . . . 9
1.6 Scheme of implosion of the fuel pellet in inertial confinement fusion [13] . . 10
1.7 Estimated Lawson parameter for ICF and MCF experiments. The colored lines mark the thresholds for the specified value of the gain factor Q for MCF, while ICF data are compared against the hot-spot ignition threshold represented by the black line [16] . . . 11
1.8 Gyromotion on the transverse plane [5] . . . 13
1.9 The mirror effect (a) Particle motion from low to high field region. (b) Reflection of the particle at the critical value of B for which parallel velocity goes to 0. (c) The longitudinal force experienced, opposite to the field gradient. . . . 16
1.10 The configuration of a simple magnetic mirror machine [22] . . . 16
1.11 (a) Toroidal and poloidal magnetic fields . . . 17
1.12 (a) Scheme of coils and magnetic surfaces in a stellarator. (b) Photograph of the W7-X during construction. From [28] . . . 18
1.13 (a) Scheme of the coils system and the field lines in a tokamak. (b) Magnetic surfaces in a tokamak. (c) Photograph of the now dismantled Tokamak Experiment for Technology Orientated Research (TEXTOR) in Julich, Germany. From [28] . . . 19

1.14 (a) Unconfined plasma in a cylinder. (b) Longitudinal magnetic field is applied. Radial motion is greatly reduced and only limited to diffusion processes. (c) Annular limiters are inserted, the stronger longitudinal motion brings the particles to collide with the limiters' sides. [23] 20
1.15 Toroidal limiter in a tokamak. [23] 21
1.16 (a) A diverted poloidal magnetic field, with an added solid surface and the formation of the relative SOL. (b) A zoomed view of the separatrix x-point. [23] 23
1.17 The pressure, potential, velocity and density profiles along a 1D profile following the field lines in the SOL between the two walls. 25
1.18 (a) The potential profile with a biased wall. The potential drop in the sheath varies accordingly to the bias, while the rest of the plasma and the right, unbiased wall remain unaffected. (b) The magnetic pre-sheath formed by oblique field-surface incidence 26
1.19 Neutralization process at the wall for a H ion, by prompt reflection (left), or by adsorption and thermal desorption in molecular form. [23] 27
1.20 Scheme of main processes involved in plasma-surface interaction. [43] . . . 28

2.1 Two-collision model for physical sputtering energy threshold. From [46] . . 33
2.2 Energy dependence of normal incidence sputtering yields for a D projectile on common wall materials 35
2.3 The local erosion-deposition process for impurities eroded by a C divertor target. From [54] 36
2.4 Examples of global impurity flows observed in different tokamaks. From [58] 38
2.5 (a) A picture of the PSI-2 device located at Forschungzentrum Julich. (b) A pictorial scheme of PSI-2 [64] 40
2.6 Pictures comparing all-carbon JET (JET-C) on the left, and JET equipped with ITER-like walls (JET-ILW), so with Be first wall and W divertor, on the right [70] 42

3.1 ERO 2.0 general workflow, with the example of D plasma irradiating a Be wall. [67] 50
3.2 JET-ILW polygon mesh used for ERO2.0 simulations in [90] 50
3.3 Comparison of the simulation volumes of ERO (red line) and ERO2.0 (green line) in JET. The dashed black lineline is the separatrix [90]. 52
3.4 Schematic representation of the execution of MPI and OpenMP processes [67]. 53

3.5 Different hybdridation of MPI and OpenMP. p is the number of MPI processes, t is the number of OpenMP threads per MPI process. The two extreme cases are (a) where each CPU in a node starts an MPI process and no OpenMP forking is used and (b) where just one MPI process is used in the whole node, leaving all CPUs available for OpenMP forking [67]. 53
3.6 GyM linear plasma device layout and characteristics [82] 54
3.7 Photographs inside of the GyM vacuum chamber (a) and of the sample-holder inserted in GyM (b) [82] 55
3.8 Global erosion rate (a) and deposition distribution (b) in GyM with varying bias for different wall materials [102] 56
3.9 Erosion rates for the samples (a) and the lateral wall (b), deposition distribution of impurities (c) in presence of the sample-holder [113] 58
3.10 comparison of experimental and simulated Y_{eff} as a function of roughness (a) and as a function of the mean surface inclination angle, in this case normalized to the Y_{eff} of the flat samples [114] 59
3.11 Photograph inside Asdex main chamber [115] 60
3.12 Experimental electron temperature and saturation current at the outer strike point in the 2019 #36687 discharge. 62
3.13 SOLPS-ITER profiles for the electron and ion temperatures, along the poloidal profile of the outer divertor, where the origin is in the strike point. The experimental data of the electron temperature at the outer divertor is also reported for reference. 63
3.14 Outer divertor 2D gross erosion profile for the three cases: full He^{+} plasma, full He^{2+} plasma and a mix of the two as described by SOLPS-ITER[116] . 63
3.15 Outer divertor gross erosion at different fixed incidence angles [116]. 64
3.16 1D net erosion profile along the outer divertor for different incidence energy and angle models. 65

4.1 Lateral wall gross erosion for Fe/Cu wall configuration as a function of the biasing voltage, applied either to the sample-holder, the bases or the bushings. 68
4.2 Contribution to the lateral wall erosion of each impurity species at the different biases in the SH configuration. Fe wall in figure (a), Cu wall in figure (b). 69
4.3 Erosion distribution on the lateral wall at 0 V (a) and 320 V (b). 70
4.4 Lateral wall erosion as a function of the bias applied to the SH for a realistic steel wall, compared to the simplified Fe/Cu wall models. 71

4.5 Sputtering yields of the plasma and impurity ions on the steel wall atomic species. 73
4.6 Composition of the eroded flux from the steel lateral wall at each bias, compared to the elemental composition of the steel 73
4.7 Contribution to the cumulative lateral wall erosion of the first step compared to the following ones, at each bias for Fe (a) and Cu (b) walls 75
4.8 Lateral wall erosion at each time step for each traced impurity, for Fe (a) and Cu (b) wall at 320 V 75
4.9 Erosion distribution on the lateral wall at different time steps 76
4.10 Gross erosion on samples at different biases and wall materials 77
4.11 Contribution to the samples erosion by each ion species, in Fe wall (a) and Cu wall (b) 78
4.12 Deposition location of Fe (a) and Cu (b) particles launched from each of the three Fe/Cu sources 79
4.13 Deposition on each SH component subdivided by the share of particles coming from each Fe (a) and Cu (b) source. 80
4.14 Front (a) and rear (b) view of the four sample-holder components. 81
4.15 Deposition on samples at varying bias, subdivided by the share of impurities coming from each source. 82
4.16 AFM images of the surfaces of the five samples employed in the micro scale ERO2.0 simulations 83
4.17 Values of the effective sputtering yield (Y_{eff}) calculated from ERO2.0 simulations and measured by mass-loss in experiments, for the five samples considered, as a function of the He impact energy. Overall similar values are observed for different samples, while a significant gap is observed between simulations and experiments. The SDTrimSP sputtering yield curve for He on W at normal incidence is also reported for reference. 84
4.18 Experimental and simulated Y_{eff} for the W bulk sample, including simulations performed using the modified sputtering yield that considers He retention. 85

5.1 1D net erosion profiles along the outer divertor, considering different Te obtained by multiplying the original SOLPS-ITER Te profile by a coefficient. The location of the maximum value of the Te is marked for reference. . . . 88
5.2 1D net erosion profiles along the outer divertor, considering different Ti obtained by multiplying the original SOLPS-ITER Ti profile by a coefficient. The location of the maximum value of the Ti is marked for reference. . . . 90

5.3 1D net erosion profiles along the outer divertor, considering a variable oxygen impurities content in the low charge state O^+. 91
5.4 1D net erosion profiles along the outer divertor, considering a variable oxygen impurities content in the high charge state O^{6+}. 92
5.5 Share of gross erosion caused by the background plasma He and O ions at varying O concentration, for the two charge state cases. 93
5.6 1D net erosion profiles along the outer divertor, resulting from the parametric scan on the Te coefficient while simultaneously applying a Ti coefficient equal to 2. The results of the original Te scan are also reported in dashed lines. 94
5.7 1D net erosion profiles along the outer divertor, resulting from the parametric scan on the high charge state oxygen concentration, while simultaneously applying Te and Ti coefficients both equal to 2. 95
5.8 Evolution of the 1D net erosion profile for the base case on the outer divertor at the following time steps. 97
5.9 Evolution of the 1D net erosion profile for the 2xTe, 2xTi, 2% O^{6+} case on the outer divertor at the following time steps. 97
5.10 Comparison of the electron density profile in the simulation volume between the base case and the Z_{eff} case. 98
5.11 Comparison of the time averaged density of W impurities in the simulation volume between the old model (left) and the Z_{eff} case (right). 99
5.12 Comparison of the 1D net erosion profile on the outer divertor between the base case and the Z_{eff} case. 100

List of Tables

3.1 Main parameters of the #36687 and #41480 ASDEX Upgrade L-mode discharges. 61

5.1 Average tracing time, impact energy and charge state of test particles depositing on the whole outer divertor (first three rows) and on a limited region of the outer divertor near the OSP (last three rows), where the peak n_e is located. 100